



UNIVERSIDAD DE CHILE
FACULTAD DE CIENCIAS FÍSICAS Y MATEMÁTICAS
DEPARTAMENTO DE GEOLOGÍA

NEOTECTONICS AT PUNTA DE TRALCA (33°25' S), CENTRAL COASTAL CHILE

MEMORIA PARA OPTAR AL TÍTULO DE GEÓLOGA

BÁRBARA ANDREA BUONO-CORE ZÚÑIGA

PROFESOR GUÍA:

GREGORY PAUL DE PASCALE

MIEMBROS DE LA COMISIÓN:

MARÍA PÍA RODRÍGUEZ MONTECINOS

CHRISTIAN ERWIN CREIXELL TORRES

SANTIAGO DE CHILE
2019

**SUMMARY OF THESIS SUBMITTED IN
FULFILLMENT OF THE REQUIREMENTS
FOR THE DEGREE: Geologist**

BY: Bárbara Andrea Buono-Core Zúñiga

DATE: 05/08/2019

SUPERVISOR: Gregory Paul De Pascale

**NEOTECTONICS AT PUNTA DE TRALCA (33°25' S),
CENTRAL COASTAL CHILE**

The present work is developed at Punta de Tralca Peninsula, located in the central coast at the Valparaíso Region of Chile. This location and its surroundings account for the complex tectonic and geomorphological history that has been recorded in the present land relief. Morphologies resembling wave-cut platforms disposed at different elevations are part of the main traits comprising the peninsula.

In this thesis, detailed mapping and description of the entire study area is presented in order to establish a first approach towards understanding the main processes that have played a role in the modelling of the current topography. To fulfill this purpose, drones have been used for the obtainment of high-resolution imagery and elevation models through the *Structure from Motion* method (SfM).

Additionally, analysis and measurement of geomorphological features such as tafoni are considered in this work. Tafoni develop worldwide and can constitute a complementary tool for the determination of a temporal evolution in a specific area. With data gathered during fieldwork, calculations of exposure ages are attempted for some of the platforms present at the peninsula.

Finally, it is expected to correlate the history told by these superficial features with the recent seismic record, as well as long-term tectonics that have affected this part of the Chilean central coast.

RESUMEN DE LA MEMORIA PARA OPTAR AL

TÍTULO DE: Geóloga

POR: Bárbara Andrea Buono-Core Zúñiga

FECHA: 05/08/2019

PROFESOR GUÍA: Gregory Paul De Pascale

NEOTECTONICS AT PUNTA DE TRALCA (33°25' S), CENTRAL COASTAL CHILE

El presente trabajo se desarrolla en la Península de Punta de Tralca, ubicada en la costa central en la Región de Valparaíso, Chile. Este lugar y sus alrededores dan cuenta de la compleja historia tectónica y geomorfológica que ha sido registrada en el relieve superficial actual. Morfologías que se asemejan a plataformas de abrasión marina dispuestas a distintas elevaciones, son parte de los principales rasgos que comprende la península.

En esta tesis se presenta un detallado mapa y descripción de la zona de estudio, para así poder establecer un primer acercamiento hacia el entendimiento de los principales procesos que han jugado en rol en el modelamiento de la topografía actual. Para llevar a cabo este propósito, se han utilizado drones para la obtención de imágenes y modelos de elevación de alta resolución a través del método *Structure from Motion* (SfM).

Adicionalmente, el análisis y medición de rasgos geomorfológicos como tafoni han sido considerados en este trabajo. Los tafoni se desarrollan en todo el mundo y pueden constituir una herramienta complementaria para la determinación de la evolución temporal de un área específica. Con datos recopilados en terreno, se han calculado posibles edades de exposición para algunas de las plataformas de la península.

Finalmente, se espera correlacionar la historia de estos rasgos superficiales tanto con el registro sísmico reciente, como con la tectónica de largo plazo que ha afectado a esta parte de la costa central chilena.

ACKNOWLEDGMENTS

Agradezco a la Tierra y a las circunstancias que me han llevado a conocerla y estudiarla.

Agradezco a los académicos que me guiaron en este trabajo. A Greg, por confiar en mí, brindarme oportunidades de aprendizaje fuera de la sala de clases y motivarme a seguir investigando. A Pía, por su paciencia, comprensión y sus sólidos aportes a este trabajo. A Chris, por su confianza, dedicación, amistad y por apoyarme constantemente haciéndome parte de sus proyectos.

Agradezco a mi hermano, Nico. Por apoyarme con el modelo del dron y sus conocimientos. Por apoyarme en la vida.

Agradezco a mis geoamigos (Gus et al. 2015-2019), quienes hicieron de mi paso por Geología los años más entretenidos, aprendidos y crecidos de mi vida. A la Frani, por enseñarme a ser mejor persona desde que yo era su jefa en scout y hasta el día de hoy; a la Roxy, por ser una especie de amiga-hermana sin la que ya no podría sobrevivir; a la Carli, por su genuina y permanente bondad, cariño, fuerza y amistad; a la Vale, por ser la más divertida, motivada y aplicada a la vez, por traer energías diferentes y positivas al clan; al Pelao, por su incondicional amistad, paciencia, empatía y cariño; al Gus, por siempre compartir conmigo su sabiduría sobre la más amplia gama de temas posible, por jamás juzgar y siempre apañar; al Hevia, por demostrarme durante su amistad que la disciplina, la locura, la sabiduría y la impulsividad sí son compatibles; al Manana, por ser como una caja de sorpresas, talentos, actitudes y magia, por haber compartido juntos memorables 21 días de terreno en la Laguna del Maule con el Claudio, Chiris y Caro; al Borja, por ser ese amigo en el cual convergen la inteligencia, la montaña, la razón y la distensión; y al Benja, por la amistad, por el rock y por todas esas geoconversaciones que me llevaron a entender mejor nuestra zona de estudio y a hacer de éste un trabajo mejor.

Agradezco a las y los funcionarios de geología y de la U por su cariño, apoyo y por las risas compartidas. A la Jacqui, a la Rosita, a la Mari, a la Vero, a Don Carlos, al Lucho. Agradezco en especial, a la Blanca, por absolutamente todo. Por las incontables salvadas y risas. Por su inagotable paciencia y empatía.

Agradezco a mis amigas y amigos del colegio, Las Ratoncitas y Los Ratones, por estos eternos e inolvidables años de amistad, en donde hemos ido cambiando, reconociéndonos y aprendiendo, además de ver a la familia crecer con puras grandes personas a sus lados. Panchi, Cata, Nacha, Franbe, Fraxie, Jesu, Nacha, Jow, Suen, Coke, Terry, Iván, Kin. Desde 1996.

Agradezco a mis amigas y amigos que conocí durante el colegio y la universidad, a los que veo siempre y a los que ya no, cada uno fue parte de mis circunstancias. A la Paski, mi favorita aquí. A toda la gente de Geología, a mi curso en Campo I, II y Económica, a la Sala de Memoristas. A la Cami Maldavsky, Caro Ganga, Jairo, Joaco, Karen, Sami, Andrea, Dani, Cata Pino, Ada, DZ, Cristián B, Vale Lepe, Nati P, Caro Geo, Coni M, Isa, a mis equipos de Volley 2010-2017, Caro Lohidoy y las cabras del Basket, a la Casa del Basket, Julio F, Cata & Fabián, Naty C, Angy, Soffi, GeoCabros 2011-2015. A los de la temporada UAI, Javi A, Javi L, Pitu, Andrea K, Sigal, Carla, Ryan, Gus, Chris, Paipo. A la Tía Paty, Tía María Eliana, Don Manuel, Tío Coke, Dolly, Maca Origen, Pablo G. A la gente de la EdV, Fran A, Lis, Dani, Marce, Gabriel Vargas, Kitty, al Pepe por acompañarme a terreno y por ayudarme a encauzar notablemente el enfoque de esta tesis. A la gente del Sernageomin por el compañerismo, amistad y terrenos, Javier, Coloma, Gus, Chris, Cata R, Chala, Pauli, Carola, Surma, Vacca, ...

Agradezco al Feminismo, por enseñarme a ser mejor mujer, mejor compañera, mejor persona. Por enseñarme a ser tanto libre como mía.



CONTENTS

1	CHAPTER ONE: INTRODUCTION	1
1.1	STUDY FORMULATION	1
1.1.1	<i>Research Problem</i>	1
1.2	OBJECTIVES.....	3
1.2.1	<i>General Objective</i>	3
1.2.2	<i>Specific Objectives</i>	3
1.3	WORK HYPOTHESIS.....	3
1.4	STUDY AREA.....	4
1.4.1	<i>Geological setting along central coast</i>	6
1.4.2	<i>Geological setting at Punta de Tralca</i>	16
1.5	NEOGENE TECTONICS.....	21
1.6	SEISMICITY	26
1.6.1	<i>Seismicity in central Chile</i>	26
1.6.2	<i>Seismicity in the central coast</i>	30
1.7	SEISMOTECTONICS	34
1.8	TAFONI	38
1.8.1	<i>What are tafoni?</i>	38
1.8.2	<i>Tafoni as indicators of time</i>	42
2	CHAPTER TWO: METHODS AND INFORMATION SOURCES.....	50
2.1	GEOLOGICAL MAPS.....	50
2.2	SATELLITE IMAGES	51
2.3	DRONE IMAGERY	51
2.4	TOPOGRAPHIC DATA.....	56
3	CHAPTER THREE: RESULTS.....	61
3.1	PLATFORMS	61
3.2	FRACTURES AND FAULTS	75
3.3	DIKES AND ENCLAVES	82
3.4	TAFONI CLASSIFICATION AND DISTRIBUTION.....	85
4	CHAPTER FOUR: DISCUSSION AND CONCLUSIONS.....	96
4.1	DISCUSSION.....	96
4.1.1	<i>About Platforms</i>	96

4.1.2	<i>About Fractures and Faults</i>	99
4.1.3	<i>Tafoni and relative dating</i>	100
4.1.4	<i>Uplift of the peninsula and seismic activity</i>	110
4.2	CONCLUSIONS	122
4.2.1	<i>Concluding remarks</i>	122
4.2.2	<i>Suggestions for future work</i>	124
5	BIBLIOGRAPHY	126
6	ANNEXES	154

TABLE INDEX

Table 1. Table shows main characteristics of both NW and NE dike swarms present in Punta de Tralca Peninsula. Data obtained from Creixell et al. (2011).	18
Table 2. Summarize of tectonic deformational events that affected the Coastal Cordillera during the Cenozoic. Data obtained from Giambiagi et al. (2015) and references mentioned in their work are also shown in the table. CC: Coastal Cordillera, WCC: western Coastal Cordillera, ECC: eastern Coastal Cordillera, PC: Principal Cordillera.	23
Table 3. Table shows record of largest earthquakes from 1570 to date between 31°-35° S and 70°-74° W. The earthquakes that occurred closest to or have been reported to affect the area near Punta de Tralca have been highlighted. Those highlighted in purple are the ones with highest magnitudes. Data obtained from the Chilean National Seismologic Center (CSN) and from (a) Cisternas et al. (2012); (b) Carvajal et al. (2017b); (c) Lomnitz (2004); (d) Benjamín Vicuña Mackenna (1877); (e) Carvajal et al. (2017a).	30
Table 4. Summary table of some earthquakes that have affected the study area (location in bold letter), in addition to other events where coseismic uplift has been measured. Some events affecting the area have been poorly documented and, therefore, no specific uplift information is available. They are mentioned in Table 3, but have been omitted in this table. Magnitudes M_S and M_W are surface-wave and moment, respectively. Note how, tentatively, areas closer to the trench seem to entail higher coseismic uplift.	36
Table 5. Time-averaged rates of coastal tafoni development. Sources: (1) Grisez (1960); (2) Takashi (1975, fig. 18); (3) Gill et al. (1981); (4) Mustoe (1982); (5) Matsukura & Matsuoka (1991); (6) Viles & Goudie (1992); (7) Mottershead (1994); (8) Takahashi et al. (1994). ^a Based on pls. 10 and 11. ^b Calculated from tafoni depth in this study. ^c The year 1981 from G. E. Mustoe (1991, pers. commun.). Table obtained from Sunamura (1996).	44

Table 6. Elevation range and mean elevation per platform (in meters above sea-level), area covered and main features for each platform are summarized here. Elevation was obtained from DEMs..... 64

Table 7. Tafoni development scale proposed in this work and applicable to the study area. Images correspond to tafoni found at Punta de Tralca Peninsula, specifically. Field photos by author..... 89

Table 8. Tafoni measurements obtained from fieldwork by author. Colors in each cell represent the surface and/or scarp in which tafone measurement was taken (Platforms: P1-red, P2-pink, P3-orange, and P4-yellow). Lower levels have been omitted since enclave tafoni is poorly developed, joint tafoni are unilaterally well-developed in every platform, and regular tafoni are not present (only in loose boulders that probably fell from upper platforms to lower ones)..... 93

Table 9. Maximum depths measured per type of tafone obtained from data presented on Table 8. Colors in each cell represent the surface and/or scarp in which tafone measurement was taken (Platforms: P1-red, P2-pink, P3-orange, and P4-yellow). 94

Table 10. Tafoni initiation ages for each type of tafoni considering different values for t^* and z_c . Values are indicated in the upper-left corner of each table. 109

Table 11. Elevation range and maximum elevation for each platform mapped at Punta de Tralca Peninsula. 111

Table 12. Sea level highstands and their correspondent MIS stage or substage, MIS age and reference. 111

Table 13. Estimated percentage of permanent vertical deformation for each platform according to previously associated MIS stage ages and considering different subsidence rates based on literature referenced in the text. (*) Arbitrary values were chosen for the Holocene platform P6 in order to study the behavior of the parameter S..... 113

Table 14. Table shows measured values for coseismic uplift (see Table 4, References) highlighted in grey, and estimated minimum values from the lineal tendency set in Figure 61. Magnitudes M_S and M_W are surface-wave and moment, respectively. Bars at the side show the number of events -given their uplifting potential- that would have contributed to the rising of platforms P5 and P6. For this analysis maximum height values for each platform are used (Table 11). Estimated accumulated coseismic uplift for all documented earthquakes in the area is also shown..... 118

Table 15. Estimated emergence time (T_E) in years before present (BP) for each platform considering different coseismic uplift values (U_C) calculated using Equation (5). The number of events or earthquakes (N_E) expected to have affected each platform has also been calculated using Equation (6)..... 120

Table 16. Summary table showing the calculated exposure ages (in calendar or common era age (C.E.)) for platforms P4, P5 and P6 from Table 14 and the associated registered earthquakes for those values, considering different coseismic uplift long-term mean values (U_C) defined by the user. N.R. stands for “not recorded” seismic events..... 121

FIGURE INDEX

Figure 1. Overall view of the study area. (a) White polygon corresponds to area shown in (b). (b) Part of Valparaíso Region. Red star shows Punta de Tralca Peninsula location. (c) Punta de Tralca Peninsula. Satellite images obtained from Google Earth.	5
Figure 2. NW view of the staircase-like block-tower of Punta de Tralca Peninsula. DJI Mavic Air drone on the rock was used for data obtainment and processing during this work. Field photo by the author.....	6
Figure 3. a) Simplified map of the Andean orogen between 33° and 34° S. Obtained from Giambiagi et al. (2015). Red lines indicate faults with Quaternary activity. Red star in (a) shows location of Punta de Tralca Peninsula.....	8
Figure 4. Perspective view of shaded-relief bathymetry off central Chile. Image shows high variability in morphology of the continental slope. The uplifted Punta Salinas Ridge is spatially coincident with the landward projection of the Juan Fernández Ridge. VFB stands for Valparaíso Forearc Basin. Yellow star indicates Punta de Tralca peninsula's location. Image obtained from Contreras-Reyes et al. (2015) and modified by author.....	10
Figure 5. Simplified regional geologic map. Base map from Sernageomin (2003) modified by Leyton et al (2010).	13
Figure 6. Regional map of the main structures around the study area. Purple solid lines indicate fault traces. Dashed lines depict inferred or covered traces. Purple circles indicate normal movement for the fault segment. The location of Punta de Tralca Peninsula is shown with a red star. Orange, green and yellow stars show the location of Río Maipo, Puangue and Melipilla Faults, respectively. Note how Melipilla Fault divides into north and south branches to the west. Fault traces were mapped based on Rodríguez (2008).....	15
Figure 7. NW-striking dikes from ETDS at Punta de Tralca Peninsula showing sinistral displacement. Hammer for scale. Field photo by the author. Specific location and orientation for the shot is shown in Annex 2.	20

Figure 8. NE- and NW-striking dikes from ETDS. Left: Field photo by the author with hammer for scale (at 33.426°S/71.706°W). Right: Orthophoto from DJI Phantom 4 drone flight by Gregory De Pascale (at 33.430°S/71.702°W)..... 21

Figure 9. Schematic profile showing earthquake locations in dots, registered between 1973 and 2007 from the NEIC catalogue and for a latitude of 33,5° S. Nazca Plate is represented by the blue color, whereas South American Plate is green. The dashed lines show the seismogenic sources: (a) thrust interplate, (b) intermediate-depth intraplate, (c) crustal, and (d) outer-rise. Figure obtained from Leyton et al. (2010)..... 27

Figure 10. Seismotectonic segments, rupture zones of historical subduction earthquakes, and main tectonic features of the south-central Andean convergent margin. Earthquakes were compiled by Melnick et al. (2006) from Lomnitz (1970, 2004), Kelleher (1972), Comte et al. (1986), Cifuentes (1989), Beck et al. (1998), and Campos et al. (2002). Nazca plate and trench are from Bangs & Cande (1997) and Tebbens & Cande (1997). Maximum extension of glaciers is from Rabassa and Clapperton (1990). F.Z.—fracture zone. Figure obtained from Melnick et al. (2006). Red star showing the location of Punta de Tralca has been added by the author. 29

Figure 11. Left: tafoni in sandstone at Zion National Park, Utah. Photo by the author. Right: honeycomb tafoni and some nest tafoni at Koh Kut, Thailand; photo by Jennifer Bright obtained from <https://fineartamerica.com/featured/rock-erosion-3-koh-kut-jennifer-bright.html?product=beach-towel>. 39

Figure 12. Left: intricate tafoni pattern at El Corte de Madera Creek; photo by Dawn Endico obtained from <https://www.flickr.com/photos/candiedwomanire/84148980..> Right: Honeycomb tafoni in sandstone at Drachenfels, Wabenverwitterung, Germany. Photo from <https://mapio.net/pic/p-14183158/>. 40

Figure 13. Left: Tafoni and case-hardening in Almo Granite, Idaho; photo by Mark Wilson obtained from <http://woostergeologists.scotblogs.wooster.edu/2017/07/26/>. Right: Tafoni and case-hardening in sandstone at South Jeolla in South Korea; photo obtained from <https://creativecommons.org/licenses/by-sa/3.0>. 41

Figure 14. Schematic diagram showing equation (2) that describes the reduction in rock strength with time t and depth z ; t^* is the time when the rock surface ($z = 0$) attains the critical strength S^* for the onset of mechanical breakdown. Figure obtained from Sunamura (1996)..... 46

Figure 15. Temporal change in tafoni depth and respective equation, where z is the depth of the tafoni, z_c is the depth of the weathering front, t is time and t^* is the time when the rock's strength or resistance to weathering is critical and the tafoni starts to grow. Obtained from Sunamura (1996). 46

Figure 16. Conceptual tafone evolution model based on Sunamura (1996), from an unweathered rock at $t = 0$ to an inactive well-developed tafone at $t \gg t^*$, where t is time, t^* is the time where the rock is sufficiently weathered for removal of disaggregated material to start, z is the depth of the tafone (surface of the cavernous form in relation to the original unweathered surface at a certain time t), and z_c is the advance-depth of the weathering front in relation to the original unweathered surface. Note that z_c must be greater than z in order for the tafone to be active. If $z = z_c$, the tafone becomes inactive..... 49

Figure 17. Satellite image of the study area obtained from Google Earth. 51

Figure 18. Screenshot of the grid generated from the flight route of the drone, where the blue dots are locations of the orthophotos taken by the drone. 52

Figure 19. Screenshot of the generated disperse point cloud, with some control-points (PC1, PC2 and PC3) taken in the field with a Garmin GPS, so as to refine the model coordinates. 53

Figure 20. Screenshot of the generated dense point cloud, showing control-points PC1, PC2 and PC3. 53

Figure 21. Orthophoto of Punta de Tralca peninsula obtained from the first drone flight during fieldwork. Image resolution is 26.7 cm/pix. Drone used was a DJI Phantom 4. Field photo by Gregory De Pascale. 55

Figure 22. Orthophoto of Punta de Tralca peninsula obtained from the second drone flight during fieldwork. Image resolution is 4.7 cm/pix. Drone used was a DJI Mavic Air. Field photo by Nicolás Buono-Core. 56

Figure 23. DEM of the whole study area obtained from first drone flight using a DJI Phantom 4 drone. Flight by Gregory De Pascale. Legend has been modified for achieving better visualization of elevation data. 57

Figure 24. DEM of the seaward end of the peninsula, obtained from second drone flight using a DJI Mavic Air drone. Flight by Nicolás Buono-Core. Hill shade effect has been applied for achieving a more realistic view of the topography..... 58

Figure 25. DEM of the seaward end of the peninsula obtained from second drone flight using a DJI Mavic Air drone. Flight by Nicolás Buono-Core. Legend has been modified for better visualization of elevation..... 59

Figure 26. Slope map of the seaward end of Punta de Tralca Peninsula obtained from second drone-flight DEM model. Drone used was a DJI Mavic Air drone. Flight by Nicolás Buono-Core. 60

Figure 27. Punta de Tralca Peninsula platform map 1:5000. Basemap obtained with high resolution drone imagery from first flight. Drone used was a DJI Phantom 4. Flight by Gregory De Pascale..... 62

Figure 28. Platform map of Punta de Tralca Peninsula seaward end, 1:1000. Platforms from P1 to P7 correspond to the highest and lowest levels, respectively. Unedited orthophoto obtained with DJI Mavic Air drone; flight by Nicolás Buono-Core. 63

Figure 29. Images shows platform P7 covered by waves in a low tide. Dark seaweed can be observed attached to the surface of the platform. Field photo by the author. Photo-shot location and orientation shown in Annex 2..... 65

Figure 30. Topographic profile A-A' obtained from Google Earth software. Up: profile trace A-A'. Down: simplified interpretation of the topography with relatively low

resolution. Platforms P2, P3, P5, P6 and P7, cannot be distinguished at this scale and resolution..... 66

Figure 31. Topographic profile B-B' obtained from DEM developed with drone DJI Phantom 4. Up: profile trace B-B'. Down: interpretation of the topographic profile where P1, P2, P4, P5, P6 and P7, stand for the mapped and described platforms with their respective color index. 67

Figure 32. Up: unedited field photo by the author. Down: interpreted image of the seaward end of the peninsula showing platforms 1, 2, 3 and 4 with a WNW view. White dashed line indicates the exposed surface of a notorious quartz-plagioclase-biotite vein emplaced along a fracture. Purple dashed lines show fault planes (the one with a question mark is a fracture in which no apparent setoff could be seen). Photo-shot location and orientation shown in Annex 2..... 68

Figure 33. Photo taken from P6 showing a SSE view of the blocky pattern mentioned in the text. Field photo by author. Photo-shot location and orientation shown in Annex 2. 69

Figure 34. SE view of the 3D drone model corresponding to the seaward end of the peninsula. Up: unedited image. Down: interpreted image. Distinct vein shows no setoff. White arrows show apparent setoff within platform P5. Photoshoot location shown in Annex 2. 70

Figure 35. SW view of the peninsula. Up: unedited field photo taken with DJI Mavic Air drone; flight by Nicolás Buono-Core. Down: edited image showing platform levels in different colors. P1 is the highest recognized platform level, whereas P6 is the lowest emerged. P7 is underwater and seen between waves. White polygons in NW and NE-strike correspond to El Tabo Mafic Dike Swarm (ETDS). White arrows indicate apparent setoff (see 72

Figure 36. SE view of the peninsula showing platforms from P1 to P7. Up: unedited field photo by author. Down: interpreted image with mapped platforms, scale and orientation. Purple dashed line shows recognized subvertical fault trace. White

arrows show apparent setoff (see text for discussed interpretation). Photo-shot location and orientation shown in Annex 2. 74

Figure 37. SW view of the peninsula showing apparent displacement of P5 (white arrow) along the NE dike strike of ETDS. Field photo by author. Photo location and orientation shown in Annex 2. 74

Figure 38. SW view of the seaward end of the peninsula. Up: unedited field photo taken with DJI Mavic Air drone; flight by Nicolás Buono-Core. Down: interpreted image showing the El Tabo Dike Swarm (ETDS), both NW and NE-striking components. Photo-shot location and orientation shown in Annex 2. 76

Figure 39. Panoramic southward view of P4 scarp (with inherent panoramic-effect distortion). Up: unedited panoramic field photo by author. Down: interpreted image showing an example of a NE-dipping fracture and vein (white dashed line). NW and NE ETDS are also shown. NE ETDS visible outcrop is indicated with a solid turquoise line, while the dashed line indicates its covered by in situ-formed sand. Photo-shot location and orientation shown in Annex 2. 77

Figure 40. Images showing fallen boulders at platform P6 removed from their original location due to a blocky-pattern erosion triggered by the existing joint sets. Field photos by author. Photo-shot location and orientation shown in Annex 2. ... 78

Figure 41. Map showing NW and NE dike swarms, and NW and NE minor fractures. Photo obtained with DJI Mavic Air drone; flight by Nicolás Buono-Core. 79

Figure 42. Quartz-plagioclase-biotite vein. Left: SE view of vein at P2's surface. Right: vein mineralogy close-up. Field photo by author. Photo-shot location and orientation shown in Annex 2. 80

Figure 43. Sigma-type-resembling structures observed in NE ETDS, specifically where NW and NE ETDS crosscut at platform P6. Origin and classification are unclear. View of the NE dike is oriented towards the SW. Along these structures and parallel to them, fractures with weathered fine-grain non-cohesive material are seen. Field photos by author. 81

Figure 44. Left: NW dike swarm showing sinistral displacement at P6. Right: NE dike outcrop at P5. Field photos by author..... 83

Figure 45. NW and NE-striking dikes from El Tabo Mafic Dike Swarms (ETDS). Left: original image obtained in the field. Right: sketch showing crosscutting relation. Field photo by author. 83

Figure 46. Mafic elongated oriented enclaves of variable sizes. Left: 70-cm enclave with ellipsoidal basal section. Right: NW-oriented enclaves that have been differentially eroded. Elongation axis in both images goes towards the southeast. Field photos by author..... 84

Figure 47. Images showing presence of salt crystals from sea spray in enclaves (Left), favoring weathering processes. Right: hopper crystals close-up. Field photos by author. 85

Figure 48. Enclave tafoni (Type III) of about 20 cm in long axis. Tafone at the right, shows additional erosion spots within. Field photos by author. 86

Figure 49. Left: Type II Joint tafoni at P2 scarp. Right: Type III Joint tafoni at wall located close to intersection of ETDS (see Figure 38). Some joint-defined blocks have already been removed by erosion. 33 cm geological hammer for scale. Field photos by author..... 86

Figure 50. Image shows some joint tafoni (Type II) and enclave tafoni at the surface of P2 and scarp of P1 platforms. Field photo by author. Photo-shot location and orientation shown in Annex 2. 87

Figure 51. Regular tafoni found at platform P4. Photos A-E show Type I tafoni. Photos E and F show disaggregated tonalite minerals (mixed with sand from P4 deposit) inside the tafone indicating that it is still active. Field photos by the author. 88

Figure 52. Lichen-covered surfaces at SE face of the main platform sequence outcrop. At the background of the image, the main regional platform of this coastal

area can be distinguished. Field photo by author. Photo-shot location and orientation shown in Annex 2. 90

Figure 53. Image shows highly eroded tonalite outcrop at P4: joint tafoni development through different-striking sets shaped the outcrop, triggering considerable material loss (Type I). Field photo by author. 91

Figure 54. Image of P1 scarp showing detachment of a block triggered by joint tafoni erosive action. White arrows indicate original position of tilted block outlined in blue. Field photo by author..... 92

Figure 55. Map of the seaward end of Punta de Tralca peninsula, showing profile traces C-C', D-D' and E-E' interpreted below. 94

Figure 56. Topographic profiles C-C', D-D' and E-E' from traces shown in Figure 55. Platform location is shown with the respective platform label and color index shown at the beginning of this chapter. NW and NE ETDS correspond to northwest- and northeast- striking El Tabo Mafic Dike Swarms mapped in section 3.3. Major fractures are shown in dashed purple lines. Tafoni development scale indexes are shown in each profile in grey boxes, where I corresponds to well-developed tafoni and III to poorly-developed tafoni, as proposed in Table 7. 95

Figure 57. Grooves found at platform P5 interpreted as former inner edges dipping towards the ocean. Hammers for scale. Field photo by the author. Photo-shot location and orientation shown in Annex 2. 97

Figure 58. Platform P1 at the top of the staircase-like platform sequence, displaying enclave tafoni. Location of drone photo-shot shown in Annex 2..... 98

Figure 59. Well developed (Type I) regular tafone found in a loose block at platform P5 scarp. Field photo by author..... 101

Figure 60. Schematic simplified potential correlation of the platform sequence at Punta de Tralca Peninsula to the late Quaternary global sea level curve based on Lambeck et al. (2002), Creveling et al. (2017), and Pico et al. (2017). Approximate ages used are based on Broecker et al. (1968), Mesolella et al. (1969), Lambeck et

al. (2002), Hearty et al. (2007), Pedoja et al. (2011, 2014), Pico et al. (2016), and Creveling et al. (2017)..... 112

Figure 61. Measured coseismic uplift values for different earthquake magnitudes. Red dotted line shows lineal tendency of the data. Data derived from Table 4 (see references in it) and specific values for the construction of this graph are shown in Annex 1. 115

Figure 62. (A) Space-time diagram of central Chile earthquakes. Solid horizontal lines represent estimated rupture lengths. The arrows indicate that the rupture lengths extended farther in that direction. Dashed lines show uncertain rupture lengths. Dashed line with question marks for the 1575 earthquake reflects inadequate reports, which make the estimated rupture length very uncertain. Earthquakes of past centuries that were large but not great ($7.5 > M > 7$) and whose rupture lengths could not be estimated are shown by (O). Locations of this century's main shocks are shown by stars. M_s , M_w , and M_t are surface-wave , moment, and tsunami magnitudes (Abe (1981)), respectively. (B) Central Chile region and aftershock areas of the 1985 and 1971 earthquakes. Obtained from Comte et al. (1986)..... 117

1 CHAPTER ONE: INTRODUCTION

1.1 STUDY FORMULATION

1.1.1 Research Problem

The morphological features present in the Earth's current crustal portion, correspond to millions of years of geologic evolution. Along its history, the planet has experienced different stress regimes in which distinct tectonic, magmatic and volcanic processes have controlled the dynamics in the crust leading to an always-changing topography.

Chile, in particular, has a very complex tectonic record. Compressive and extensive regimes, variable rates and directions for the subduction of Nazca plate under the South American plate along its border, currently at a convergence rate of 68 mm/a (Ruegg et al. (2009)), eventually triggered uplift and subsidence episodes together with the appearance of several structures in the crust (Paskoff (2005)). Segmentation along the country takes place to accommodate the heterogeneous-moving blocks. Consequently, the landscape of this convergent margin is the result of the complex interplay between internal tectonic processes, surface deformation and erosive processes driven by the interaction of tectonic and climate (Montgomery et al. (2001); Lamb & Davis (2003); Farías (2007); Strecker et al. (2007); Farías et al. (2008); Aguilar et al. (2013); Armijo et al. (2015); Sepúlveda et al. (2015)).

Understanding this record and quantifying its activity allows to determine how the coastal morphological configuration has developed throughout recent periods, which is one of the goals of this thesis. Several studies have been developed in relation to this topic, so as to determine coseismic, postseismic and interseismic deformation rates from morphological observations (Lajoie (1986); Leonard & Wehmler (1991); Nelson & Manley (1992);

Ortlieb et al. (1996a,1996b); Marquardt et al. (2004); Melnick et al. (2006); Saillard et al. (2009); Farías et al. (2010); Regard et al. (2010); Rodríguez et al. (2013); Yildirim et al. (2013); Jara-Muñoz & Melnick (2015); Jara-Muñoz et al. (2015); Martinod et al. (2016); González et al. (2018)). Consequently, these studies show how long-term and coseismic deformation have influenced the current morphology. Features such as emerged marine terraces, cliffs and platforms, are evidence of the mentioned dynamics and therefore contain useful information for the characterization of the associated tectonic activity.

The coastal area from the V Region of Valparaíso in Chile accounts for these morpho-tectonic dynamics. Punta de Tralca Peninsula, which is located at the southern area of the V Region, comprises a very specific example of these configurations due to the presence of surfaces located at different heights that resemble wave-cut platforms, which are one of the focus of this thesis.

Other peninsulas along the Chilean margin have been studied before in order to unravel Neogene and Quaternary tectonic activity. Peninsulas potentially tend to preserve geomorphological features (such as marine landforms) influenced by local tectonic forces that account for seismogenic and long-term deformation, as well as showing a greater deformational response to interplate seismic activity, likely due to their relative closeness to the trench (Ortlieb et al. (1996b); Delouis et al. (1998); Melnick et al. (2006); Saillard (2008); Saillard et al. (2009); Vigny et al. (2009); Regard et al. (2010); Farías et al. (2010); Vargas et al. (2011b); Melnick et al. (2012a); Lin et al. (2013); Jara-Muñoz & Melnick (2015); Jara-Muñoz et al. (2015); González-Alfaro et al. (2018)).

Also, a distinct feature to be analyzed in this work, is the presence of tafoni at the study area. These geomorphological elements develop worldwide under steady erosive conditions, and have been used as temporal-analysis tools through the modeling of growth rates in different lithologies and regions (Grisez (1960); Takashi (1975); Gill et al. (1981); Mustoe (1982); Matsukura & Matsuoka (1991); Viles & Goudie (1992); Mottershead (1994); Takashi et al. (1994); Sunamura (1996); Norwick & Dexter (2002);

Brandmeier et al. (2010)). This work aims to establish a first approach towards the usage of these geomorphological features as a temporal-analysis tool to determine the emergence of the observed platforms at Punta de Tralca.

1.2 OBJECTIVES

1.2.1 General Objective

This thesis aims to provide a first approach towards the correlation of different platforms and tafoni development at Punta de Tralca with long-term tectonic activity as well as recent seismic events recorded throughout central Chile's written history, through detailed characterization and mapping of the study area.

1.2.2 Specific Objectives

Specific goals of this thesis include:

- a. Reconnaissance and determination of morphological markers at Punta de Tralca Peninsula including platform elevation and extension, lithological distribution (enclaves and dikes), fractures, and characterization of geomorphological features (such as tafoni), through field and remote sensing techniques supported by drone usage.
- b. Establishing a coherent tectonic chronology for the area, considering coseismic and long-term deformation records along with geomorphological data.

1.3 WORK HYPOTHESIS

The present work is developed under the hypothesis that the morphological features observed at Punta de Tralca Peninsula, such as platforms and erosional forms, register

long-term and seismic deformation that have affected the area throughout the recent periods of time.

From that basis, a detailed map of the study area and elevation profiles of the platforms developed with drone imagery, tafoni study and measurements, uplift records and seismological data, will constitute the main tools in order to support the analysis of this work hypothesis.

1.4 STUDY AREA

Punta de Tralca Peninsula ($33^{\circ}25'$ S) is located at the coastal southern part of the V Region of Valparaíso in Chile, at about the same latitude of Santiago, located ~90 km to the west (Figure 1). The peninsula covers an area of approximately 0.11 km^2 .

Four different climates can be distinguished at this region: estepa climate with great atmospheric drought and three temperate climates with different cloudiness and dry-period lengths. Current annual average rainfall is 372.5 mm, which concentrate between May and August. It is in this same time of the year where lowest temperatures are registered, ranging from 3°C in July and 31°C in March. Prevailing wind direction is SE (~ 150°) between October and May, changing northwards (0°) between June and September. Wind velocities vary very little throughout the year, between 11 and 17 km/hr.



Figure 1. Overall view of the study area. (a) White polygon corresponds to area shown in (b). (b) Part of Valparaíso Region. Red star shows Punta de Tralca Peninsula location. (c) Punta de Tralca Peninsula. Satellite images obtained from Google Earth.

Punta de Tralca Peninsula is distinguished by a staircase-like feature carved in the Paleozoic intrusive rocks that comprise the seaward far end of the peninsula (Figure 2). This specific area contains several erosive evidences affecting the rock, such as joint sets, tafoni, blocky-pattern erosion and mineral disaggregation. The latter can be found in the whole area. Furthermore, the rest of the peninsula constitutes a relatively smooth surface (with only few topographic heights and more pronounced slopes towards the ocean) mainly covered by fine to coarse-grained sand as a product of *in situ* chemical and mechanical weathering of the country rock, as well as areas with dark soil development and vegetation (mainly “docas”). The highest points are at about 30 m a.s.l., whereas the predominant sand-covered level reaches ~ 20 m a.s.l.

This peninsula is located ~ 50 km above the interplate seismogenic zone and ~ 90 km landward of the trench. The subduction angle between the Nazca and South American Plates in this area is c. 30°, in contrast to the Pampean or Chilean flat-slab segment (27-33° S) located immediately north of the peninsula, within which the subduction angle is c. 10° (Cahill & Isacks (1992)).



Figure 2. NW view of the staircase-like block-tower of Punta de Tralca Peninsula. DJI Mavic Air drone on the rock was used for data obtainment and processing during this work. Field photo by the author.

1.4.1 Geological setting along central coast

The present-day architecture of the world's largest non-collisional orogen, the Andes Mountains, along with the Coastal Cordillera, are largely the result of convergence and consequent subduction of the Nazca plate under the South American continent, at a convergence rate of 68 mm/a (Ruegg et al. (2009)). Evidence of contractional, extensional and strike-slip deformation periods, is vastly found along these distinctive features, although mechanisms by which crustal shortening is achieved -and consequent thickening and surface uplift (Isacks (1988); Sheffels (1990); Allmendinger et al. (1997))- remain

controversial (e.g. Garzzone et al. (2008); DeCelles et al. (2009); Ehlers & Poulsen (2009); Armijo et al. (2010); Farías et al. (2010); Comte et al. (2019)).

At this latitude, Chile can be divided into four different morphostructural units displayed in NS-striking fringes, as a result of its tectonic configuration and Andean orogeny (

Figure 3). These are, from west to east: (1) the Coastal Platform (CP), characterized by the presence of uplifted marine and continental sediments and surfaces; (2) the Coastal Cordillera (CC), constituted by a Paleozoic accretionary complex and magmatic arc constituting the crystalline continental basement (Coastal Batholith), as well as Mesozoic volcanic sequences; (3) Central Depression (CD), a low-lying basin filled by Pliocene-Quaternary conglomerates and volcanic rocks; and (4) Main Cordillera (MC), characterized by high topography and an active volcanic arc (e.g., Mpodozis and Ramos (1989)).

The Pennsylvanian Coastal Batholith comprising part of the CC in south-central Chile, is shown to have been emplaced in a very short period (20 Ma) and to be relatively homogeneous in crystallization age of both Hf and O isotopic compositions along an 800 km length, regardless of rock types which vary from quartz diorite to granite (Deckart et al. (2014)). Furthermore, the CC unit can be divided into Western Coastal Cordillera (WCC) and Eastern Coastal Cordillera (ECC) (Farías et al. (2008); Rodríguez (2008)).

WCC comprises metamorphic and intrusive Late Paleozoic rocks to the west, and intrusive Mesozoic rocks to the east. It is also characterized by a smooth homogeneous relief, interpreted as marine terraces (Fuenzalida et al. (1965)). Most of these marine terraces are displaced by NW-striking normal faults (Aron et al. (2015)).

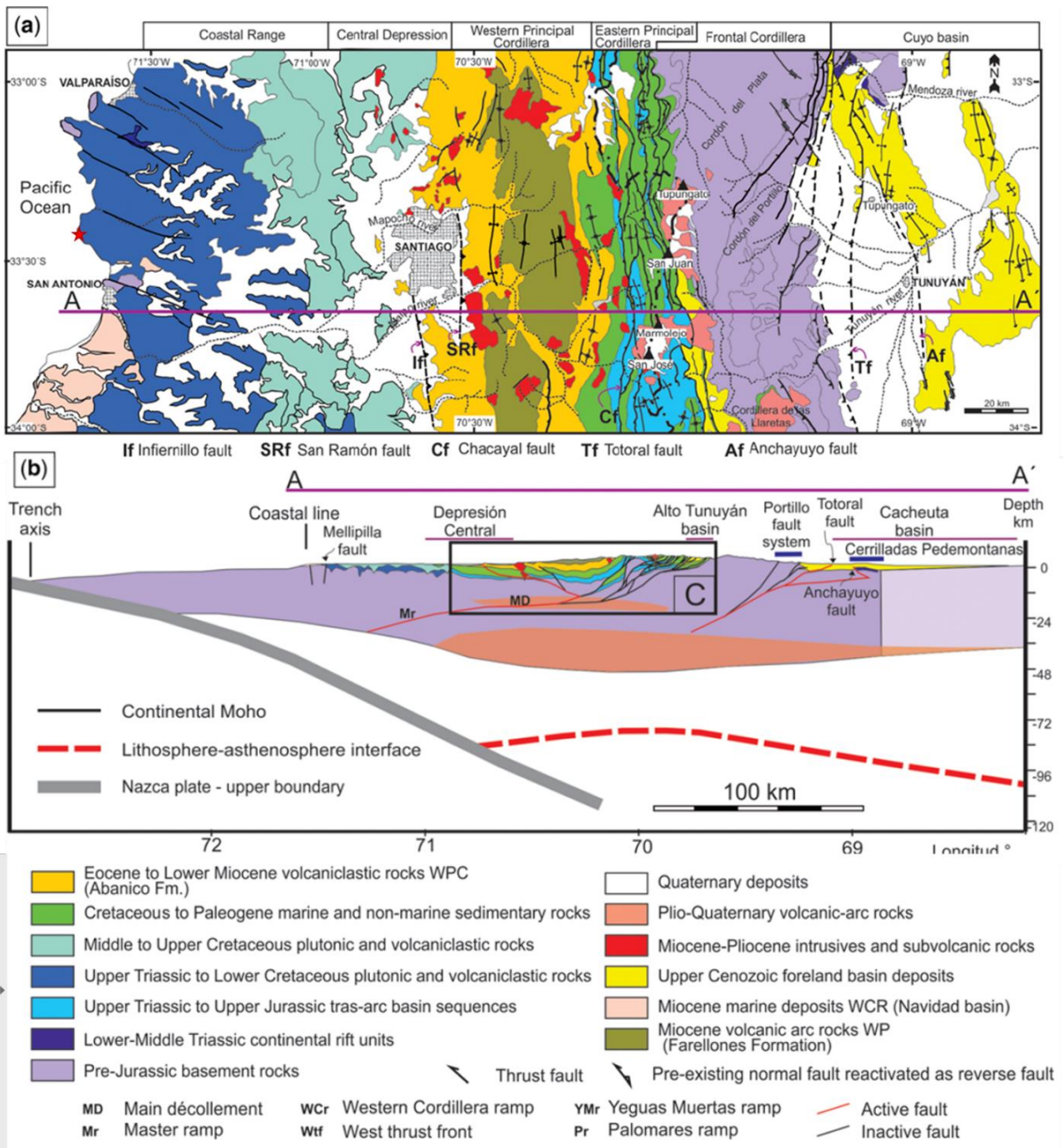


Figure 3. a) Simplified map of the Andean orogen between 33° and 34° S. Obtained from Giambiagi et al. (2015). Red lines indicate faults with Quaternary activity. Red star in (a) shows location of Punta de Tralca Peninsula.

ECC corresponds to concordantly stratified volcanic and sedimentary rocks (homoclinal) towards the west and to Late Mesozoic intrusive rocks to the east. It forms a mount chain

with summits that reach more than 2000 m a.s.l. close to Santiago, diminishing its height to the south. Some of these summits and smooth areas on CC scarps have been interpreted before as relicts of continental-erosion surfaces (Borde (1966); Farías et al. (2007); Rodríguez et al. (2014)).

According to Rodríguez et al. (2014), a pediplain dominated the landscape of the present-day CC (between 28-32° S), prior to Lower Miocene. This pediplain was offset during the Early (Middle?) Miocene, leading to uplift of the actual ECC and to the formation of a secondary topographic front. During the Late Miocene, the entire CC was uplifted.

Another large-scale feature observed at this latitude is the presence of the Maipo Orocline (Farías et al. (2008)), which coincides with the collision of the Juan Fernández Ridge with the South American Plate. The latter constitutes a major bathymetric anomaly and tectonic discontinuity of the Nazca plate. Collision of the Juan Fernández Ridge at about 10 Ma BP (Yáñez et al. (2002)) is an approximately coeval event that might have caused some disturbance along the subduction zone, that is, flattening of the subduction plane between 27 and 33° S at eastward longitudes (Yáñez et al. (2001)). It probably influenced later evolution of the Andean range along this region (Ramos et al. (2002)) and resulted in a lack of Plio-Pleistocene volcanic activity, as well as no development of the Central Depression.

Additionally, the seamounts that comprise the Juan Fernández Ridge at the subducted plate, constitute positively correlated bathymetric and magnetic anomalies which can account for the observed subaerial topographic features and tectonics of the upper plate. Ridges intersecting continental margins are areas of major uplift and local tectonic erosion in the collision zone (Yáñez et al. (2001)).

Another interesting feature about the study area, is the presence of the San Antonio submarine canyon immediately south to Punta de Tralca Peninsula. This canyon extends

for about 170 km to the NW excavating the forearc slope, where it enters the trench axis via San Antonio Reentrant near 33° S (Figure 4) supplying coarse-sediment backscatter material transported down the canyon as turbidity currents (Hagen (1996); Laursen & Normak (2002)). Multibeam survey over the canyon revealed an overall sinuosity of 1.25 (channel length/valley length), a broad roughly U-shaped cross section, an almost constant channel slope above the forearc structural high, reminiscent of stream braiding and point bars inside channel beds (Hagen (1996)). The development of the San Antonio Canyon was controlled or strongly influenced by the subduction of the San Antonio Seamount beneath the head of the reentrant about 165 ka ago (Laursen & Normak (2002); Laursen et al. (2002)).

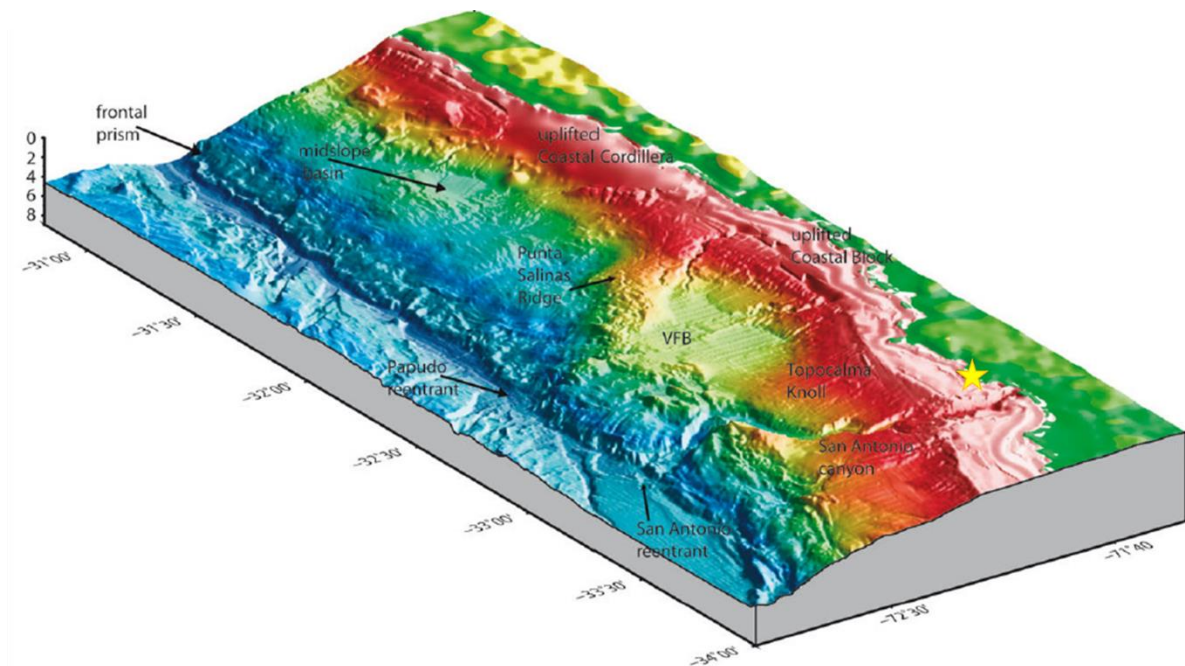


Figure 4. Perspective view of shaded-relief bathymetry off central Chile. Image shows high variability in morphology of the continental slope. The uplifted Punta Salinas Ridge is spatially coincident with the landward projection of the Juan Fernández Ridge. VFB stands for Valparaíso Forearc Basin. Yellow star indicates Punta de Tralca peninsula's location. Image obtained from Contreras-Reyes et al. (2015) and modified by author.

In this thesis, the focus will be a very specific part of the WCC, where Punta de Tralca Peninsula is located. The main lithology and structural geology are shown in

Figure 3 and listed in detail in the sections below.

1.4.1.1 Lithology

The study area is mainly dominated by a Paleozoic Coastal Batholith and a Mesozoic central batholith, along with Paleozoic metamorphic basement outcrops and sedimentary and volcanic Neogene formations.

The Coastal Batholith of central Chile between 31° and 34° S represents a locus of long-lived (c. 200 Ma) plutonic activity. It is composed by plutonic rocks which occur as north-trending discontinuous belts that decrease in age eastward and that range in composition from tonalite to granite (Siña (1987); Arce (2002)). Gana et al. (1994) describe and classify these rocks as two major units described below (Unidad Sauce, Js; Unidad Mirasol, Pzmg) with several marine cut terraces (QTt); the latter, with a NS disposition matching the coastline. Their description is presented below, whereas a simplified map of the regional geology is shown in Figure 5.

Also, several mafic dike swarms have been recognized along the coastline between 33° and 33°45' S, mainly intruding the Late Paleozoic basement. Creixell et al. (2011) describes them in detail: Concón Mafic Dike Swarm (CMDS), Cartagena Mafic Dike Swarm (CrMDS) and El Tabo Dike Swarm (ETDS).

Quaternary

Current littoral and eolic deposits (Qe)

Non-consolidated beach sediments composed by sand and well-rounded boulder gravels. Mainly horizontal stratification and some low angle cross stratification including sandy

lamination and active yellow-sand well selected transverse dunes with cross stratification and superficial ripples (Gana et al. (1994)).

Aluvial deposits (Qa)

Non-consolidated sediments including interdigitated fluvial and gravitational deposits composed by gravels, sand and silt. These deposits host gold placers (Gana et. al, 1994).

Tertiary

Navidad Formation (Tn)

Miocene-Lower Pliocene sedimentary sequences of fine-grain sandstone, intercalated conglomerate and siltstones with abundant fossiliferous content. These marine facies gradate to a more continental one to the top, with presence of sandstones and conglomerates. Variable tilting of the formation is associated to structures that favor block tectonics (Tavera (1979); Gana et al. (1994)).

Paleozoic

Intrusive rocks

Mirasol Unit (Pzmg) (Gana et al. (1994))

Tonalites, granodiorites, syenite-granites, microcline-granites and amphibole-biotite monzogranites. Coarse to medium grain size rocks, greenish gray in color, with dioritic to quartz-rich dioritic enclaves. Enclaves disposition is parallel to the magmatic foliation of the host rock and might form up to 50% of it (Isla Negra). This unit also has magmatic foliation affected by tectonic foliation, which is evidenced by mylonitic zones (Mirasol and Punta Tralca). The composite pluton is 36 km long with a NW distribution. The contact between lithologies is mainly gradational. Intruded by foliated basic dikes and Jurassic plutons forming magmatic enclave zones. Crystallization date varies from 405 Ma U-Pb in zircon (Godoy & Loske (1988); Corvalán & Munizaga (1972)) to 292 ± 2 Ma isochrone Rb-Sr in total rock (Hervé et al. (1988)). The latter, being the commonly accepted age.

Metamorphic rocks

Valparaíso Metamorphic Complex (Pzmv) (Gana et al. (1996))

Foliated metamorphic rocks with a mainly plutonic parental rock. They are exposed as inclusions within intrusive complexes (less than 2 km long) and are intruded by Paleozoic granitoids with a gradual contact (Quintay and Las Cruces). Granitic and tonalitic orthogneisses and intercalations of amphibole, sericitic and chloritic schists, along with para-gneissic aluminum-silicate-rich lenses. Foliation strikes NNW and dips S; metric wavelength folding with minor ductile shear overlaps the main foliation. Metamorphism of Caleta Las Cruces orthogneisses dated by K-Ar in biotite is 278 ± 6 Ma (Cordani et al. (1976)). Gneisses in Cartagena gave dates between 167-145 Ma with K-Ar method in biotite, amphibole and plagioclase (Cordani et al. (1976); Hervé et al. (1988); Gana et al. (1996)).

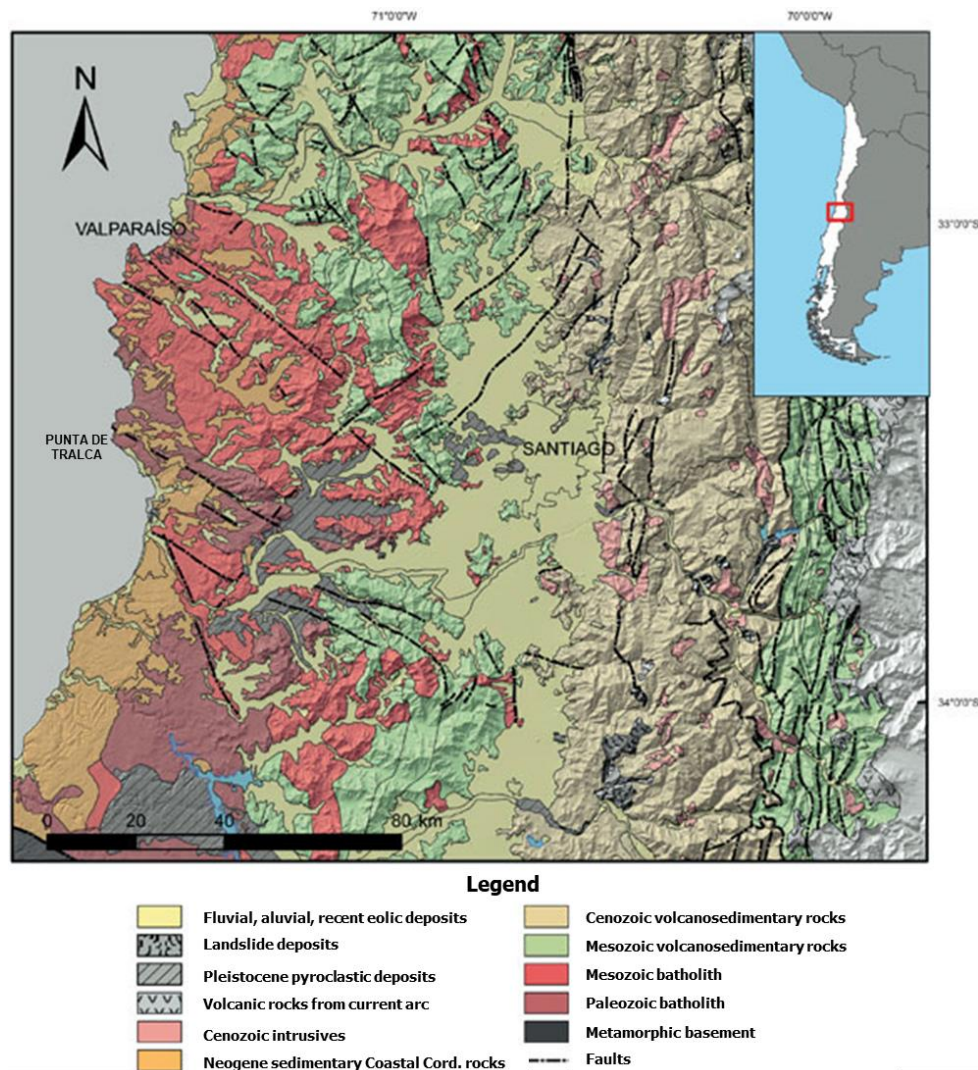


Figure 5. Simplified regional geologic map. Base map from Sernageomin (2003) modified by Leyton et al (2010).

1.4.1.2 Structural geology

Tectonics on a large scale are characterized by the existence of two structural domains: occidental and oriental. The occidental domain is characterized by several levels of Miocene-Pliocene wave-cut terraces which height varies from 100 to 230 m a.s.l. It is formed by Paleozoic-Middle Jurassic plutonic to metamorphic bedrock, along with scarce remnants of Late Cretaceous-Paleogene sedimentary rocks (strata from Quebrada Municipalidad and from Algarrobo formations) with NNE strike and 15° W dip. The bedrock is subhorizontally covered by Neogene marine and continental sedimentary units, and some Pleistocene ones (Navidad Formation and Potrero Alto strata).

A block structure system predominates and is limited by NW and NE faults with a vertical displacement (post-Pliocene) over imposed on a strike-slip movement, which allows block rotation affecting Cretaceous rocks along the Coastal Cordillera (Gana et al. (1994)).

The oriental structural domain is characterized by abrupt and highland setoff. Part of the Coastal Cordillera can reach heights of 2000 m. The Cretaceous and partly Jurassic intrusive rocks and the Jurassic to Lower Cretaceous volcano-clastic sequences, form a monoclinical block with NNE to NNW strike and dip 40° E in average. Some folds can be found related to faults or intrusive rims (Gana et al. (1996)).

The main great structures in the Coastal Cordillera at this latitude are the: Melipilla, Río Maipo and Puangue Faults (Figure 6). The Melipilla Fault is a WNW-striking subvertical structure interpreted as a dextral strike-slip transpressional fault (Gana et al. (1996)), located closest to Punta de Tralca Peninsula. It extends throughout the Maipo River valley and it branches into two NW segments: one of these affecting Paleozoic intrusive rocks near el Quisco north of the peninsula, and the other deviating towards Cartagena Bay (Rodríguez (2008)). This structure coincides with the magnetic and gravimetric Melipilla Anomaly located at intermediate depths within the upper crust (Gana et al. (2004); Yáñez

et al. (1998)) and it is suggested to comprise the symmetry axis of the Maipo River Orocline (Yáñez et al. (2002)).

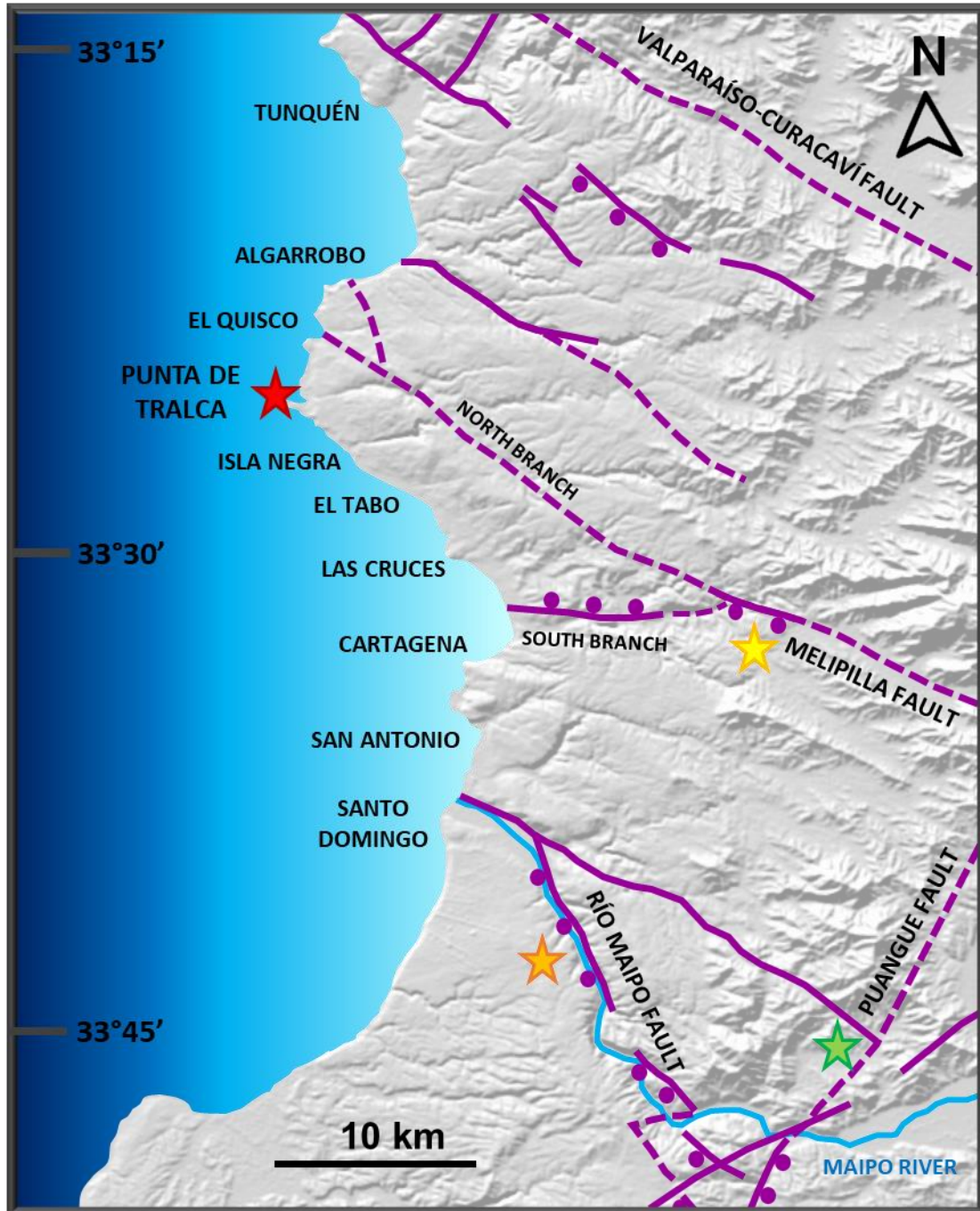


Figure 6. Regional map of the main structures around the study area. Purple solid lines indicate fault traces. Dashed lines depict inferred or covered traces. Purple circles indicate normal movement for the fault segment. The location of Punta de Tralca Peninsula is shown with a red star. Orange, green and yellow stars show the location of

Río Maipo, Puangue and Melipilla Faults, respectively. Note how Melipilla Fault divides into north and south branches to the west. Fault traces were mapped based on Rodríguez (2008).

Further south, the NNW-striking Río Maipo Fault shows post-Pliocene normal displacement (Gana et al. (1996)) and extends from the mouth of the Maipo River to the mid-course of Cachapoal River (at ~ 34°30' S), determining an adjacent SW hanging wall formed by rocks from Navidad Formation and a NE foot-wall formed by Triassic-Jurassic intrusive rocks (Rodríguez (2008)).

Finally, the NNE-striking Puangue Fault, shows a post-Pliocene normal displacement that determines hanging and foot- walls formed by Paleozoic and Triassic intrusive rocks (Gana et al. (1996)).

1.4.2 Geological setting at Punta de Tralca

1.4.2.1 Lithology and geomorphology

The study area is mainly dominated by a Paleozoic Coastal Batholith, as mentioned in the previous sections. Specifically, Parada et al. (1999) describe four plutonic complexes for the Coastal Batholith emplaced during four major episodes of arc magmatism: Santo Domingo, Limarí, Papudo-Quintero and Illapel Complexes.

Punta de Tralca Peninsula displays several platforms that have been carved into rocks that belong to the Santo Domingo Complex or to the Paleozoic Marisol Unit (Pzmg), according to the classification proposed by Gana et al. (1994).

In particular, the Santo Domingo Complex (Carboniferous, c. 290 Ma) comprises hornblende-biotite bearing tonalites and granodiorites with abundant mafic enclaves, and

enclave-free granites. The association of enclave-bearing granitoids and enclave-free granites resulted from different degrees of mixing of crustal -and mantle- derived magmas (Parada et al. (1999)).

The lithology observed at Punta de Tralca Peninsula corresponds to the mentioned tonalite, which presents mafic enclave alignment along the whole peninsula's outcrops and lose eroded blocks. No significant variations regarding composition are observed in this specific study area.

In relation to the mafic dike swarms mentioned in section 1.4.1.1, El Tabo Dike Swarm (ETDS) can be seen at some of the platforms carved in Punta de Tralca tonalite (Figure 7).

ETDS is a mafic dike swarm that comprises two systems of dikes (Table 1) with different orientation cross-cutting each other: a mainly NW dike swarm formed by multiple parallel intrusions, and a NE dike swarm (Figure 41). They can be found in outcrops along the coast between Algarrobo and El Tabo intruding Late Paleozoic foliated granitoids.

	NW dike swarm	NE dike swarm
Texture	Porphyritic to aphanitic	Porphyritic
Lithology groundmass	Brown hornblende prisms, accessory titanite, magnetite and locally chromite.	Clinopyroxene (Wo ₄₀₋₄₂ En ₂₉₋₃₁ Fs ₂₆₋₂₉), plagioclase (An ₅₂₋₅₃), accessory ilmenite, apatite and minor biotite.

Lithology phenocrysts	Subparallel plagioclase (An ₅₃₋₇₄) and amphibole prisms, and clinopyroxene (Wo ₂₈ En ₄₈₋₅₀ Fs ₂₀₋₂₃).	Plagioclase
Mean dike thickness	0.6 m	2.6 m (0.5 – 4 m)
Mean orientation	137°/89° W	65°/79° N

Table 1. Table shows main characteristics of both NW and NE dike swarms present in Punta de Tralca Peninsula. Data obtained from Creixell et al. (2011).

Felsic veins with high quartz, plagioclase and biotite content are distinguished among the tonalite (Figure 42). Narrow chlorite-epidote veins are also distinguished in some areas cut by NW dikes, indicating dike opening is normal to the walls.

Adjacent to this peninsula, marine-cut terraces are observed to the east of Punta de Tralca. These morphologies appear all along the coastal area in the region and in the coast of Chile, and have several levels that can be correlated from north to south (e.g., d’Orbigny (1842); Darwin (1846); Domeyko (1848); Herm (1969); Paskoff (1970, 1977); Leonard & Wehmiller (1991, 1992); Ota et al. (1995); Ortlieb et al. (1996a); Marquardt et al. (2004); Encinas et al. (2006); Melnick et al. (2006); Rodríguez (2008); Saillard (2008); Saillard et al. (2009); Regard et al. (2010); Saillard et al. (2012); Rodríguez et al. (2013); Jara-Muñoz et al. (2015); Martinod et al. (2016); González-Alfaro et al. (2018); Guerrero (in prep.)).

In relation to Quaternary deposits, patches of eolian deposit (fine grain sand) and a medium to coarse grain deposit formed by *in situ* erosion of the tonalite, are also observed

at Punta de Tralca Peninsula. No specific dating or provenance analysis studies have been reported for the area. Fragments of shells are found along the peninsula, in a centimetric-deep layer overlying soil development, insufficiently thick so as to address further analysis. The source of this layer has been interpreted partly as anthropogenic and biogenic (since the peninsula is recurrently visited by humans leaving trash and seafood leftovers behind, as it is the natural environment for several bird species), without discarding its likely and expected geological origin.

1.4.2.2 Structures and dike swarms

The biggest and closest structure to Punta de Tralca Peninsula is the Melipilla Fault described in section 1.4.1.2, with its two NW-striking branches located to the north (near El Quisco) and south (near Cartagena Bay) of the peninsula (Figure 6).

Despite the absence of large-scale faults even closer to Punta de Tralca, some foliation data has been provided by previous works. Less than 1 km SE from the peninsula, foliation with a NW direction and SW dip has been reported. Furthermore, a NW foliation with a NE dip appears close to Isla Negra, at about 3 km SE from the peninsula (Gana, Wall & Gutiérrez (1994); Webber et al. (2015)).

The Middle-Late Jurassic mafic dike swarms of central Chile between 33° and 33°45' S register the tectonic activity of the contemporaneous arc represented by the Coastal Batholith. They evidence alternate episodes of transtension and transpression across NW-striking structures, which controlled the construction of the magmatic arc. These mafic dike swarms have been dated in Concón and Cartagena, with emplacement ages of 163 and 157 Ma along NW-SE to WNW-ESE-striking host fractures, registering a first stage of magma emplacement under sinistral transtension (Creixell et al. (2006); Creixell et al. (2011)).

Regarding the Cretaceous mafic dike swarm outcropping around Punta de Tralca peninsula -El Tabo mafic dike swarm (ETDS)-, there is no evidence of ductile deformation. Also, the orientation of both NW (Figure 7, Figure 8, Figure 41, Figure 44, Figure 45) and NE dike (Figure 8, Figure 41, Figure 44, Figure 45) systems is not similar to the foliation orientation in country rocks in El Tabo, Punta de Tralca and Las Cruces, meaning that dike emplacement happened under a different stress regime than the one ongoing during host rock emplacement (Creixell et al. (2011)). Near the dikes parallel joints can be seen in the country rock, with a decreasing density when moving away from them.

At Punta de Tralca, these dike swarms are more abundant than in the north and south of the peninsula (20% abundancy versus < 2%) and are also more closely spaced (0-0.3 m versus 2-10 m). The NW dikes cut the chlorite-epidote veins in the area, as explained in the previous section.

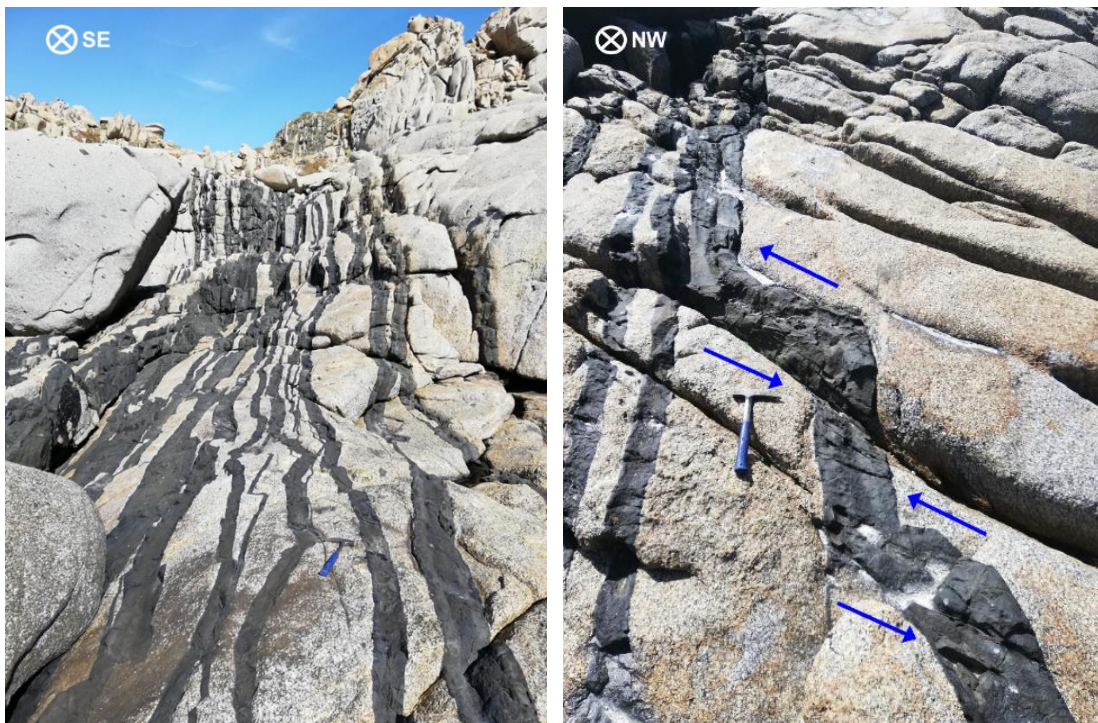


Figure 7. NW-striking dikes from ETDS at Punta de Tralca Peninsula showing sinistral displacement. Hammer for scale. Field photo by the author. Specific location and orientation for the shot is shown in Annex 2.

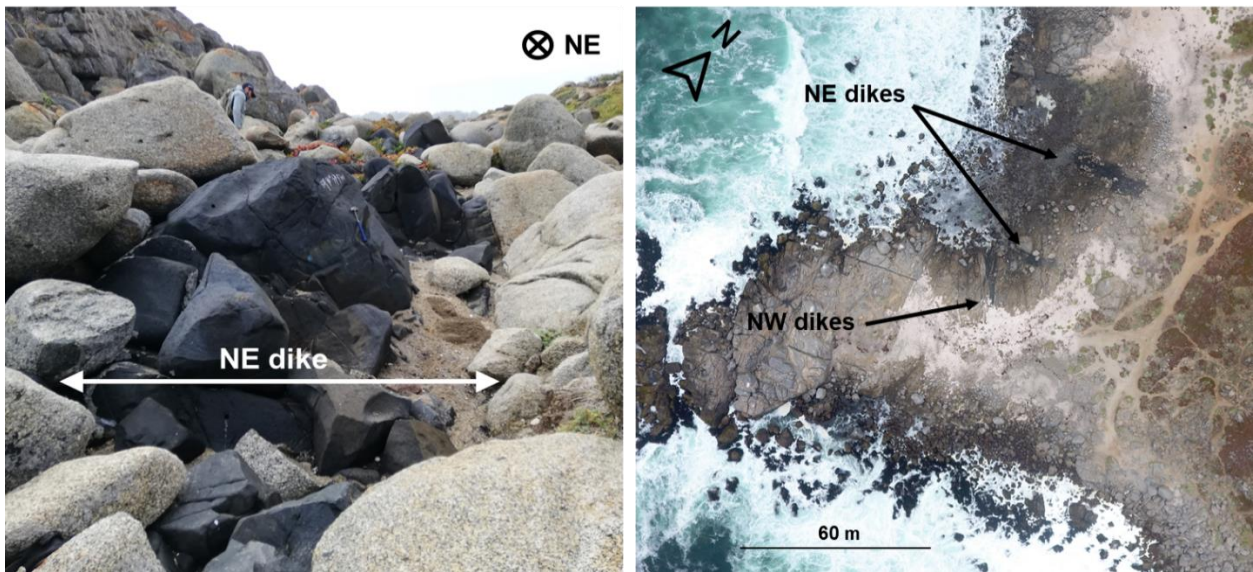


Figure 8. NE- and NW-striking dikes from ETDS. Left: Field photo by the author with hammer for scale (at 33.426°S/71.706°W). Right: Orthophoto from DJI Phantom 4 drone flight by Gregory De Pascale (at 33.430°S/71.702°W).

1.5 NEOGENE TECTONICS

The landscape of convergent margins is the result of the complex interplay between internal tectonic processes, surface deformation and erosive processes driven by the interactions of tectonics and climate. Subduction zones concentrate crustal deformation as seen all along the Chilean margin.

Major crustal discontinuities inherited from pre-Andean geologic processes, such as Paleozoic ductile shear zones or lithological contacts, are used by the current tectonic stresses to accommodate permanent, brittle deformation in the Coastal Cordillera (Thiele & Morel (1981); e.g., Hervé et al. (2007) and references therein; Aron et al. (2015)). Reverse faults are contemporaneous with the normal faults but generally scarce. Some of the structures show long-term inversions of fault kinematics (Lavenu & Cembrano (1999); Lavenu & Encinas (2005); Melnick et al. (2006, 2009); Aron et al. (2015)).

Giambiagi et al. (2015), describe and explain deformational periods for the Coastal Cordillera from an integrated kinematic model with mechanical constrains of the Maipo-Tunuyán transect (33°40' S) across the Andes, immediately south of the study area of this thesis (

Figure 3). The following table (Table 2) summarizes the main tectonic events that affected the Coastal Cordillera (CC) around the study area during the Cenozoic era according to Giambiagi et al. (2015) and other authors referenced in the table.

Period/Epoch	Numerical age (Ma)	Events	References
Late Cretaceous - Paleocene	~ 100 - 56	Contractional event in CC and crustal thickening.	Tapia et al. (2012)
Eocene - Early Miocene	~ 56 - 18	Elevation of CC due to isostatic compensation and locally, by isostatic rebound close to the Abanico east-dipping master fault. Exhumation of ECC (36 - 42 Ma, Late Eocene).	Giambiagi et al. (2015) Fariás et al. (2008)
Early Miocene	21 - 18	Uplift of ECC. Shortening of 1 km at CC.	Rodríguez et al. (2012), Gutiérrez et al. (2013), Fock (2005) Giambiagi et al. (2015)
Late Early Miocene	17 - 15	Uplift of ECC (coeval to PC).	Giambiagi et al. (2015)
Late Miocene	~ 10 - 4	WCC subjected to local extensional stress field. WCC subsides due to flexural elasticity of the rigid cold forearc. ECC is uplifted instead.	Lavenu & Encinas (2005) Giambiagi et al. (2015), Encinas et al. (2006) Giambiagi et al. (2015), Encinas et al. (2006)
Early Miocene - Early Pliocene	~ 23 - 3	WCC is submerged (evidenced by marine deposits of Navidad Formation and younger units).	Encinas et al. (2008), Gutiérrez et al. (2013)
Pliocene	5 - 2.5	CC uplifted by isostatic rebound due to widening of the crustal root.	Encinas et al. (2006), Fariás et al. (2008)
Quaternary	2.5 - present	Development of marine and continental landforms during tectonic stability or slow uplift. Renewed/accelerated coastal uplift post 400 ± 100 ka.	Rodríguez et al. (2013), Regard et al. (2010), Saillard et al. (2009), Martinod et al. (2016)

Table 2. Summarize of tectonic deformational events that affected the Coastal Cordillera during the Cenozoic. Data obtained from Giambiagi et al. (2015) and references mentioned in their work are also shown in the table. CC: Coastal Cordillera, WCC: western Coastal Cordillera, ECC: eastern Coastal Cordillera, PC: Principal Cordillera.

Furthermore, in this subduction context, deformation is concentrated in the magmatic arc zone where crustal thermal weakening occurs. Therefore, tectonics and magmatic activity

are strongly linked. In particular, the study of emplacement mechanisms of dike swarms has been proved as an effective tectonic tool to understand the evolution of ancient magmatic arcs (e.g., Glazner et al. (1999)). In addition, Creixell et al. (2011) discusses the emplacement mechanisms of dike swarms (described in previous sections of this report) and the consequent recognition of the regional deformation history during the construction of the Jurassic to Cretaceous Coastal Batholith of central Chile.

At a regional scale between 33° and 34° S the axis of the Middle-Late Jurassic coastal batholith changes from an almost NS direction to a NW-SE one, that can also be correlatable with the main NW structures in the area (as shown in Figure 5, Figure 6) that are suggested to have controlled the emplacement of dike swarms described by Creixell et al. (2006, 2009, 2011) and Middle-Late Jurassic plutons in the coastal area, at least during the first stages of growth of the batholith (163 - 157 Ma), and will be reactivated later during the Cenozoic (Wall et al. (1996); Rivera & Cembrano (2000)).

At instrumental time scales, both crustal seismicity and GPS surface displacements show that the subduction seismic cycle produces pulses of episodic rapid coseismic extension and slow, interseismic, convergence-parallel shortening of the upper plate (Aron et al. (2015)). Particularly, strong vertical deformation driven by coseismic rebound is considered among the primary effects that contribute to coastal relief construction (Baker et al. (2013); Wesson et al. (2015); Melnick (2016)).

Regarding temporal analysis of the Coastal Cordillera evolution, several authors have related and determined long-term vertical deformation rates, coseismic deformation and seismicity throughout the Neogene and Quaternary (Darwin et al. (1846); Kaizuka et al. (1973); Ortlieb et al. (1996a, 1996b); Marquardt et al. (2004); Melnick et al. (2006); Saillard et al. (2009); Farías et al. (2010); Regard et al. (2010); Farías et al. (2011); Vigny et al. (2011); Moreno et al. (2009); Moreno et al. (2012); Melnick et al. (2012); Baker et al. (2013); Rodríguez et al. (2013); Yildirim et al. (2013); Jara-Muñoz & Melnick (2015); Jara-

Muñoz et al. (2015); Wesson et al. (2015)); Melnick (2016); Saillard et al. (2017); Melnick et al. (2017); González-Alfaro et al. (2018)).

Regarding temporal analysis of this part of the Coastal Cordillera evolution, regional geomorphic correlation between coastal and continental surfaces form a wide marker that has been uplifted ~ 150 m since formation. Given the similarity in the exposure ages of different landforms studied by Rodríguez et al. (2013), they suggest those surfaces probably formed coevally along the coast and throughout the valleys between ~ (1200?) 800-500 ka ago and could have been finally uplifted ca. 500 ka. They also suggest that after a period of slow uplift or tectonic stability long enough to develop such a broad geomorphic marker, ~ 150 m of uplift occurred during the Pleistocene (post 500 ka). The results obtained by Regard et al. (2010), also suggest renewed or accelerated coastal uplift for the region post 400 ± 100 ka that extends continuously between 15° and 32°30' S. This area is immediately north of Punta de Tralca Peninsula, at 33°25' S.

In particular, marine terraces are geomorphic markers that may provide relevant information about coastal paleo-dynamics and vertical tectonic movements (e.g. Dupré (1984); Trenhaile (2002); Marquardt et al. (2004); Saillard et al. (2009); Limber and Murray (2011)). Marine terraces are formed by the interaction between eustatic sea-level fluctuations and tectonic uplift (Bradley (1957); Lajoie (1986); Muhs et al. (1990); Anderson et al. (1999)); during episodes of sea-level rise and during highstand periods a wave-cut platform is carved into the landscape whenever wave erosion forces cliff retreat (Anderson et al. (1999)). The wave-cut platform may be abandoned during the next low-stand period, leaving behind a terrace deposit or veneer of marine and continental sediments (Bradley (1957)). If the uplift rate is fast enough the platform can be preserved during the next highstand period at higher elevations and remain unaffected by rising sea level. An emerged marine terrace is thus preserved, while a new platform will be sculpted at lower elevation (e.g. Rosenbloom and Anderson (1994)). Considering that presently sea-level is at the highest position since the Marine Isotope Stage (MIS) 5e (Shackleton et al. (2003); Hearty et al. (2007)), marine terraces formed during or after the MIS 5 that are still recognizable in the landscape are generally preserved as a result of rapid tectonic

uplift (Lajoie (1986); Pedoja et al. (2011); Jara-Muñoz et al. (2015); González-Alfaro et al. (2018)).

1.6 SEISMICITY

1.6.1 Seismicity in central Chile

Chile is one of the most seismic countries in the world and has been affected by some of the largest earthquakes worldwide, produced along its subduction margin (Cifuentes & Silver (1989); Cifuentes (1989); Vigny et al. (2011); Carvajal et al. (2017a, 2017b)). In particular, the Andes of central Chile and Argentina is one of the most hazardous seismic zones of South America (Holtkamp et al. (2011)). Structural damage in buildings, tsunamis, landslides, liquefaction and ground rupture, are part of the potential hazards that can affect the region during high-magnitude earthquakes. Earthquake sources and mechanisms of the subduction zone boundary are rather well established and include large megathrust ruptures, as well as intraplate ruptures either within the Nazca or South American plates (Barrientos (2007)).

Furthermore, different seismogenic sources with a variety of movements with expected peak ground accelerations (PGA) according to the type and location of the motion, have been described in Chile.

The four seismogenic sources or types of earthquakes are: (a) thrust interplate or megathrust, (b) intermediate-depth intraplate or deep-moderate, (c) crustal, and (d) outer-rise (Figure 9), where most of the seismicity corresponds to interplate events. These are characterized by Gutenberg-Richter and attenuation laws that have been re-evaluated lately in order to represent their distinctive characteristics independently (Saragoni et al (2004); Astroza et al (2002, 2005); Ruiz & Saragoni (2005a); Leyton et al (2010)).

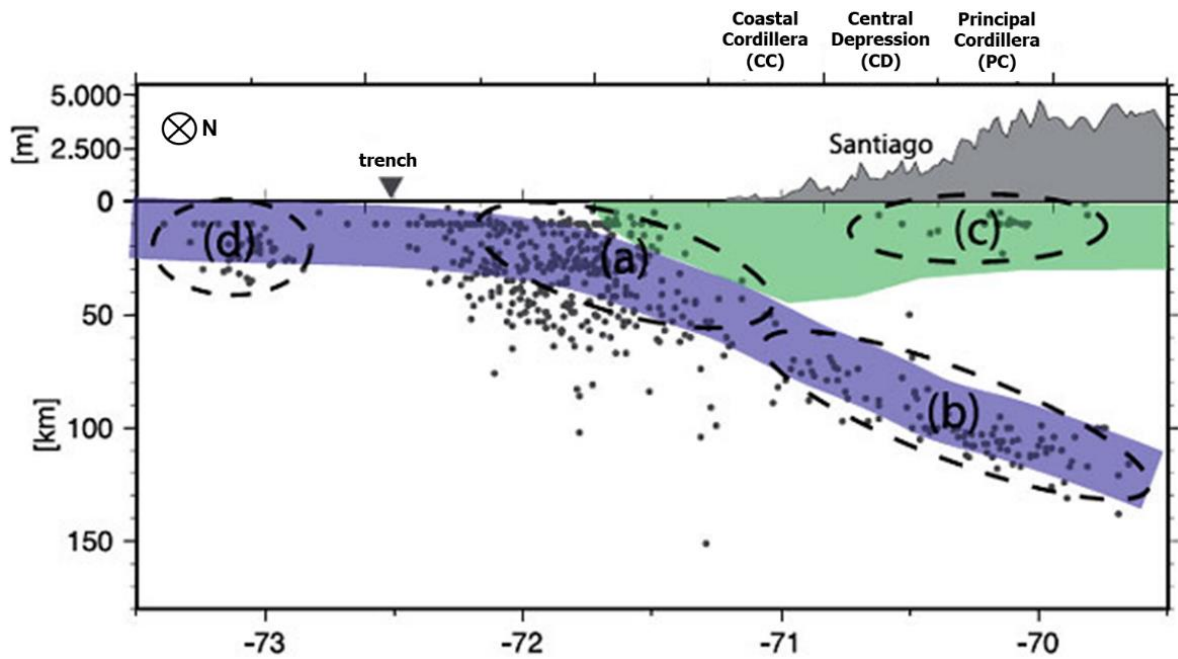


Figure 9. Schematic profile showing earthquake locations in dots, registered between 1973 and 2007 from the NEIC catalogue and for a latitude of $33,5^{\circ}$ S. Nazca Plate is represented by the blue color, whereas South American Plate is green. The dashed lines show the seismogenic sources: (a) thrust interplate, (b) intermediate-depth intraplate, (c) crustal, and (d) outer-rise. Figure obtained from Leyton et al. (2010).

As shown in Figure 9, the coastal area is effectively and potentially affected by most of the seismic activity. Since a vast majority of the earthquakes originate near the trench, the study area has experienced most of this motion -along with occasional tsunamis-, relatively speaking. Therefore, the importance of an overall comprehension on these matters and the need of updated seismic hazard studies.

The seismic cycle of great subduction earthquakes has been described as a repetitive sequence of crustal deformation phenomena constituting three main steps: strain accumulation during the interseismic period, release of strain by an earthquake during the coseismic stage, and the postseismic period, characterized by complex transient processes in the years to decades following the earthquake (e.g. Wang, 2007).

Another important concept regarding seismic activity, has to do with segmentation along major fault systems in subduction zones, which controls earthquake magnitude and location (Figure 10). The existence of discrete seismotectonic blocks and barriers to rupture propagation along the south-central Chile margin is similar to observations from other subduction zones. Earthquake barriers have been commonly associated with lower or upper-plate anomalies (e.g., Shennan et al. (2009); Audin et al. (2008)); Collot et al. (2004); Jara-Muñoz et al. (2015)).

Bathymetric anomalies have also been related to sustained earthquake-rupture barriers in central Perú, Sumatra and Costa Rica by Perfettini et al. (2010), Subarya et al. (2006) and Bilek et al. (2003), respectively. However, segmentation patterns in subduction zones do not seem to follow a unique pattern, because in some cases earthquakes are not constrained by structural features and rupture across segment boundaries. This has been observed in the Solomon Islands (Taylor et al. (2008)), Japan (Nanayama et al. (2003)), and in Chile during the 1730 (M_w 9.1-9.3) earthquake (Udías et al. (2012); Carvajal et al. (2017a, 2017b)). The latter, ruptured across where the Juan Fernández Ridge intersects the continental margin, illustrating the ambiguous role of inferred lower-plate earthquake barriers (Figure 10). More examples of these observations are described in the section below.

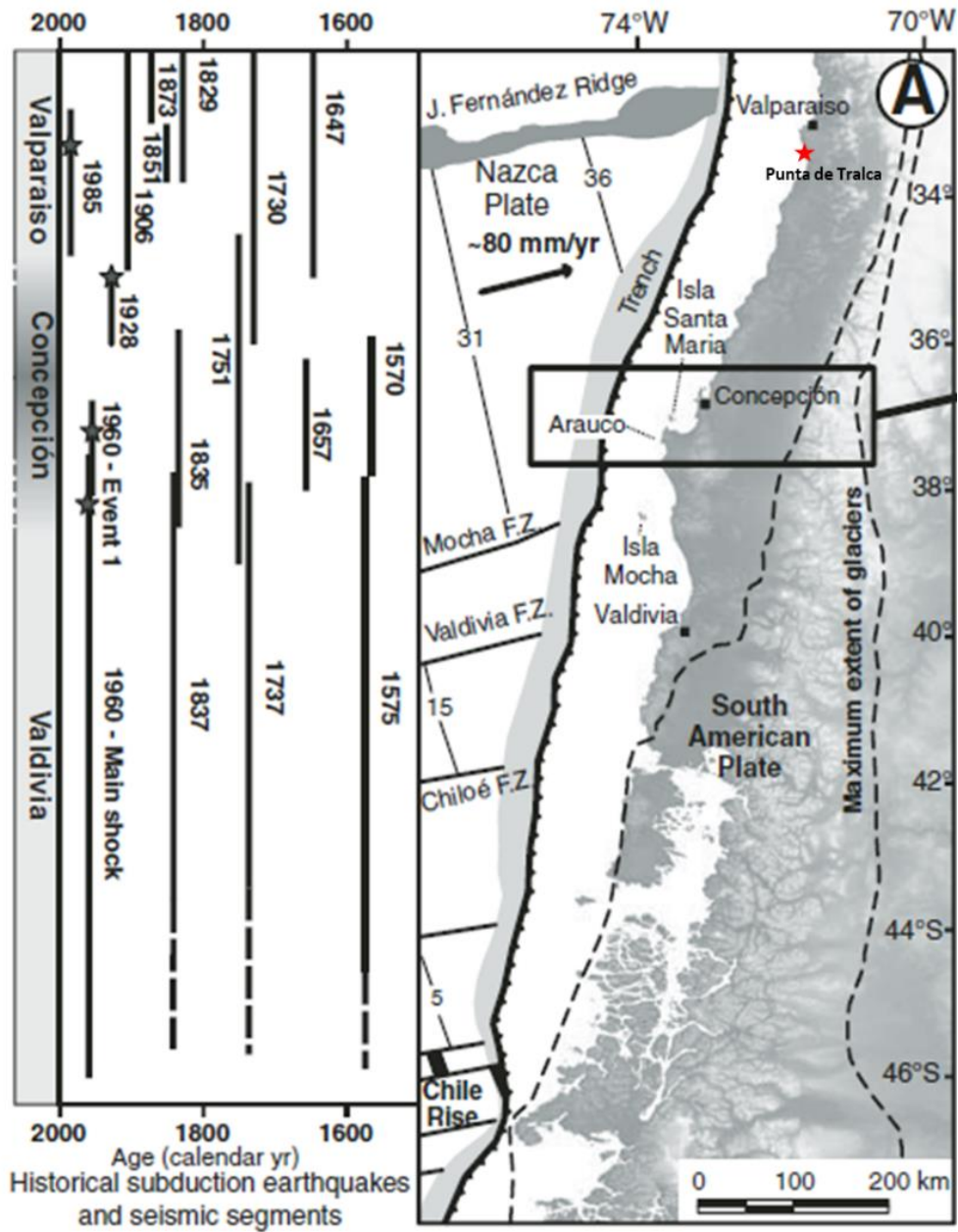


Figure 10. Seismotectonic segments, rupture zones of historical subduction earthquakes, and main tectonic features of the south-central Andean convergent margin. Earthquakes were compiled by Melnick et al. (2006) from Lomnitz (1970, 2004), Kelleher (1972), Comte et al. (1986), Cifuentes (1989), Beck et al. (1998), and Campos et al. (2002). Nazca plate and trench are from Bangs & Cande (1997) and Tebbens & Cande (1997). Maximum extension of glaciers is from Rabassa and Clapperton (1990). F.Z.—fracture zone. Figure obtained from Melnick et al. (2006). Red star showing the location of Punta de Tralca has been added by the author.

1.6.2 Seismicity in the central coast

Being a seismic country, Chile has a long record of earthquakes throughout its written history. With a rough estimate of 240 earthquakes per year (considering magnitude (M) ≥ 5 earthquakes in the last 6 years), 9 magnitude (M) ≥ 7 earthquakes with estimated epicenters relatively close to Punta de Tralca or that have been reported to affect the area, have occurred since 1570 (Table 3).

Local Date (dd-mm-yyyy)	Local time (hh:mm)	Latitude S	Longitud E	Magnitude Ms	Magnitude Mw	Depth (km)
17-03-1575	10:00	33.40	70.60	7.3		
07-08-1580	~ 19:00	N/D	N/D	7.3 ^a		
13-05-1647	22:30	35.00	72.00	8.5		
12-07-1687	2:00	32.75	70.73	7.3		
08-07-1730	4:45	33.05	71.63	8.7	9.1 - 9.3 ^b	
19-11-1822	22:30	33.05	71.63	8.5		
26-09-1829	14:00	33.05	71.63	7.0		
08-10-1847	11:30	31.61	71.18	7.3		
06-12-1850	6:52	33.81	70.22	7.3		
02-04-1851	6:48	33.32	71.42	7.0 - 7.5 ^c		
07-07-1873		32.76	73.73	8.0 ^d		
15-08-1880	8:48	31.62	71.18	7.7		
16-08-1906	19:48	33.00	72.00	8.4	8.0 - 8.2 ^e	25
29-01-1914	23:30	35.00	73.00	8.2		
01-12-1928	0:06	35.00	72.00	8.4 ^f		
18-03-1931	4:02	32.50	72.00	7.1		
13-09-1945	7:17	33.25	70.50	7.1		100
28-03-1965	12:33	32.42	71.10	7.4		68
08-07-1971	23:03	32.51	71.21	7.5	7.8	40
16-10-1981	0:25	33.13	73.07	7.5		33
03-03-1985	19:46	33.24	71.85	7.8	8.0	33
08-04-1985	21:56	34.13	71.62	7.5		37
16-09-2015	19:54	31.55	71.86		8.4	11.1

Table 3. Table shows record of largest earthquakes from 1570 to date between 31° - 35° S and 70° - 74° W. The earthquakes that occurred closest to or have been reported to affect the area near Punta de Tralca have been highlighted. Those highlighted in purple are the ones with highest magnitudes. Data obtained from the Chilean National Seismologic Center (CSN) and from (a) Cisternas et al. (2012); (b) Carvajal et al. (2017b); (c) Lomnitz (2004); (d) Benjamín Vicuña Mackenna (1877); (e) Carvajal et al. (2017a).

Most of the seismic activity in the area is caused by the interaction of Nazca and South American Plate in the interplate seismogenic zone. These subduction earthquakes are compressional with reverse faulting mechanism and their magnitude is proportional to the setoff and displacement area. Interlocked plate-zone earthquakes take place at shallow depths (0-60 km) and cause typically strong movements (Comte & Suárez (1994); Araujo & Suárez (1994)) with the possibility of generating tsunamis.

The Great Santiago Earthquake in 1647 was reported to have destroyed Santiago, with rockfalls in Santa Lucía Hill and the Andes, and liquefaction episodes. It is said to have lasted 90-100 seconds and caused around 1.000 deaths in Santiago. Reports from beyond Santiago are scant and unreliable because of the low population density (Lomnitz (2004)).

The Great Valparaíso Earthquake in 1730 highlighted in Table 3, caused damage for a length of ~1000 km along the coast with destructive tsunamis in Concepción and Valparaíso (Udías et al. 2012; Cisternas et al., 2014) that even reached the coasts of Japan (Soloviev & Go (1975)). The 1822 event left Melipilla in ruins and casualties in Valparaíso reached 72 deaths (Lomnitz (2004)). The 1822 tsunami amplitude was ~ 4 m, although with no reported damage. Only a few years later, the 1829 earthquake at Valparaíso was interpreted as a possible aftershock of the 1822 event.

The “Destruction and Fire of Valparaíso” event in 1906 was a M_w 8.0-8.2 earthquake (Carvajal et al. (2017a)), that caused the death of 3.800 people. It was felt from Tacna to Chiloé and from Juan Fernández Islands to Buenos Aires. The port area of Valparaíso was razed, but no damage caused by the ~1.5 m-amplitude tsunami was reported (Lomnitz (2004)).

A first order observation from the data gathered in Table 3, is the tentative recurrence of large events around the same area, considering rupture lengths. Therefore, different

authors have proposed and supported the hypothesis of “seismic gaps” (McCaan et al. (1979); Nishenko (1985)) to describe the evolution of large earthquakes seismic cycle in subduction areas. This means that after a large earthquake another with similar characteristics can be expected in the same subduction area, and the occurrence probability increases with time. Consequently, large earthquakes were anticipated for northern and central Chile at that time (around the year 1980), since there had not been any for several decades. Coincidentally, large earthquakes did take place in 1985 at Valparaíso and in 2014 at Iquique. Also, as shown in Table 3, the sequence of big earthquakes in the area -1647, 1730, 1822, 1906 and 1985- (highlighted in blue) could be interpreted as an example of seismic cyclicity associated to the mentioned gaps.

For instance, the 1985 earthquake ruptured a well-studied seismic gap along the Chilean subduction zone. The epicenter of this event was located near the center of an approximately 300 km long region which ruptured in the 1906 event. The northern portion of the 1906 zone has since ruptured in 1971 and 1973. Christensen & Ruff (1986), suggested that the region south of the 1985 rupture zone, which includes the 1928 zone, could be the next candidate for future large events.

Despite this, seismologic knowledge has certainly increased in the last few decades and the concept of “variable rupture” is now recognized. The same area can also experience different lengths, widths and setoffs between cycles ((Xue-Ze (2001); Bilek et al. (2003); Bilek (2007); Briggs et al. (2014); De Pascale et al. (2014); Moernaut et al. (2014); Shennan et al. (2016); Cisternas et al. (2017)). For instance, Carvajal et al. (2017b) explain how large earthquakes have historically ruptured into the likely rupture zone of the 1730 earthquake: the southern portion of the region has been ruptured by great $M_w > 8$ interplate earthquakes centered largely to the south in the years 1570, 1657, 1751, 1835, and 2010 (Lomnitz (2004); Udías et al. (2012)).

Later, the 1906 earthquake overlapped about 200 km of the northern Maule rupture (Okal (2005)), whereas the 1960 Valdivia earthquake overlapped with the southern ~90 km of

the Maule rupture across the Arauco Peninsula. As for the 1985 Valparaíso earthquake, it partly overlapped with the northern Maule rupture (Barrientos (1988); Jara-Muñoz et al. (2015)). Also, for different earthquakes, slip distributions derived from geodetic data show patches of high and reduced slip among rupture areas (Moreno et al. (2012); Lin et al. (2013)), probably related to irregularities in the subduction interface, highlighting the complex nature of these events.

During the last couple of decades several studies attempted to quantify interseismic coupling along the Chile margin based on surface velocities estimated from GPS data (Klotz et al. (2001); Brooks et al. (2003); Khazaradze and Klotz (2003); Moreno et al. (2008); Ruegg et al. (2009); Vigny et al. (2009)). These studies suggested that interseismic coupling is characterized by lateral variations at scales of tens to hundreds of kilometers. For the 2010 Maule earthquake in particular, Moreno et al. (2012) in the search for a tectonic control of earthquake segmentation, noticed that the pattern of co-seismic slip correlates with inflections in the curvature of the slab, which may produce variations in shear stresses on the megathrust, also affecting the dynamic propagation of the rupture.

Additionally, recent geophysical and geodetic observations suggest that megathrust faults are frictionally segmented at depth, a condition that seems to allow the occurrence of supercycles of giant tsunamigenic earthquakes. Ignoring regions of previous seismic energy release, giant earthquakes seem capable of propagating from the deeper plate interface all the way to trench, producing both strong shaking and devastating tsunamis (Carvajal et al. (2018)).

An example of this complex seismic behavior is the 2011 M_w 9.0 Tohoku earthquake, which ruptured the lower part of the seismogenic zone and propagated onto the previously thought aseismic shallow zone. The downdip frictional segmentation of Tohoku allowed the 2011 Japan event to grow to such a giant tsunamigenic earthquake (Lay et al. (2011c); Koper et al. (2011); Ammon et al. (2011); Ozawa et al. (2012); Satake et al. (2013)).

A similar behavior is expected for the metropolitan Chilean megathrust, that enclosed between the rupture zones of the Maule 2010 and Illapel 2015 earthquakes (Carvajal et al. (2018)). In this region, large earthquakes ($M_w > 8$) have historically occurred with a remarkable temporal regularity as mentioned beforehand (see Table 3); however, it is well established that the 1730 event was by far the largest of the sequence and the only one capable of producing a large tsunami. The rest of the earthquakes have instead been better characterized by coastal uplift than by their tsunamis.

Uplift of the coastal region around Valparaíso was systematically observed in the earthquakes of 1822, 1906 and 1985 (Lomnitz (2004)), but not in the largest earthquake of 1730. Carvajal et al. (2018) propose that these observations can be explained by a dual seismogenic behavior, in which the 1822, 1906 and 1985 events ruptured downdip segments of the large 1730 earthquake rupture zone. Because little or no shallow slip has been released in over 289 years, surpassing the minimum recurrence for large tsunamis in the region as revealed by paleotsunami studies, their results imply increased tsunami hazards for the most populated coast of Chile.

1.7 SEISMOTECTONICS

It is of great importance to analyze the seismic record of this area, since the relationship between coastal uplift and seismic activity has been broadly studied and suggested (Darwin et al. (1846); Kaizuka et al. (1973); Comte et al. (1986); Leonard & Wehmler (1991); Nelson & Manley (1992); Ortlieb et al. (1996b); Marquardt et al. (2004); Melnick et al. (2006); Farías et al. (2010); Baker et al. (2013); Yildirim et al. (2013); Gallen et al. (2014); Wesson et al. (2015)); Jara-Muñoz et al. (2015); Jara-Muñoz & Melnick (2015); Martinod et al. (2016); Melnick (2016); González-Alfaro et al. (2018)). The link between vertical deformation and coseismic elastic rebound during recent megathrust earthquakes has been therefore well-constrained (Vigny et al. (2011); Moreno et al. (2012)), although

the relationship between the long-term uplift of coastal areas and the subduction earthquake cycle remains controversial (Melnick (2016)).

This controversy is due to potential interseismic subsidence counterbalancing coseismic uplift and also affecting long-term vertical deformation measurements through time. If not taken into consideration, this complexity can lead to underestimations regarding coseismic and/or long-term uplift calculations.

Table 4 shows uplift measurements for some of the main seismic events that have affected the study area, as well as other earthquakes with well documented coseismic uplift values which are described below.

As mentioned beforehand, coseismic uplift -as well as interseismic changes in ground elevation- has been observed and well documented since the nineteenth century. For instance, Darwin and FitzRoy measured coseismic uplift around the Arauco Peninsula for the 1835 megathrust earthquake that affected the region. Coseismic uplift values for this event ranged from 0.6 m at Isla Mocha, 1.5 m at the harbor of Talcahuano, and up to 3 m at Isla Santa María (Darwin (1851)).

The Great Valparaíso earthquake of 16 August 1906, which caused severe damage in a region about 365 km long, extending from Illapel (31.7° S) to Curepto (35° S), has been studied and reported by Zegers (1906), Steffen (1907), De Ballore (1911), Lomnitz (1970), Lomnitz (2004), Okal (2005), and Carvajal et al. (2017a), for instance. Uplift of the coastline of 80 cm (at Zapallar) to 40 cm (at Llico) was measured (Steffen (1907); De Ballore (1911)). For the 1822 earthquake, with an estimated rupture zone between Illapel and San Antonio, the shoreline near Quintero and Valparaíso was uplifted 1.2 m and 0.9 m, respectively (Graham (1824); Perrey (1854)).

As for the 1985 earthquake, Comte et al. (1986) gave preliminary estimations of the permanent coastal uplift in the region, with values of 0.1 and 0.28 ± 0.05 m for Valparaíso and San Antonio, respectively. These two data are in agreement with the elevation changes predicted and proposed by Barrientos et al. (1988), which achieve maximum values of more than 0.4 m in the 130 km-long regions between Valparaíso and Pichilemu.

Year	Estimated Magnitude	Measurement location	Coseismic Uplift (m)	Distance from the trench (km)	References
1822	Ms 8.5	Valparaíso to Quintero	0.9 - 1.2	~105	Graham (1824); Perrey (1854)
1835	Ms 8.5	Arauco Peninsula	0.6 - 3	75	Darwin (1851)
1877	Mw 8.8	Punta Lobería	~ 1.2	~74	González-Alfaro et al. (2018)
1906	Mw 8.0 - 8.2	Llico to Zapallar	0.4 - 0.8	~108	Steffen (1907); De Ballore (1911)
1960	Mw 9.5	Isla Mocha	1.8 ± 0.2	~76	Plafker & Savage (1970)
		Lebu, Maule Region	~ 1.5	~75	Álvarez (1963)
		Lebu, Maule Region	1.3 ± 0.2	~75	Plafker & Savage (1970)
1985	Mw 8.0	Valparaíso to Pichilemu	0.4 - 0.5	~110	Barrientos et al. (1988)
		San Antonio	0.28 ± 0.05	~120	Comte et al. (1986)
1995	Mw 8.1	Mejillones Peninsula	0.15 - 0.8	~74	Ortlieb et al. (1996a)
2007	Mw 7.7	Tocopilla	~ 0.34	~103	González-Alfaro et al. (2018)
2010	Mw 8.8	Arauco Peninsula	~ 2.5	~75	Farías et al. (2010)
		Arauco Peninsula	2.4 ± 0.2	~75	Vargas et al. (2011)
		Yane, Maule Region	1.33 ± 0.2	~75	Vargas et al. (2011)
		Piure, Maule Region	2.4 ± 0.4	~75	Vargas et al. (2011)
		Lebu, Maule Region	1.72 ± 0.1	~75	Vargas et al. (2011)
		Santa María Island	2.6 ± 0.5	~75	Vargas et al. (2011)
		Lebu, Maule Region	~ 2.5	~75	Melnick et al. (2012a)
		Arauco Peninsula	1.75 ± 0.03	~80	Vigny et al. (2011)
		Morguilla	~ 2.4	~80	Melnick et al. (2012a)
		Arauco Peninsula	2.5 ± 1.2	~86	Farías et al. (2010)
		Arauco Peninsula	1.45 ± 0.03	~95	Vigny et al. (2011)
		Arauco Peninsula	0.55 ± 0.35	~105	Farías et al. (2010)
		Ramuncho, Maule Region	0.6 ± 0.2	~105	Vargas et al. (2011)
		Arauco Peninsula	0.25 ± 0.2	~108	Farías et al. (2010)
		Arauco Peninsula	0.81 ± 0.03	~110	Vigny et al. (2011)
		Arauco Peninsula	0.44 ± 0.01	~115	Vigny et al. (2011)
Punta Tumbes, Maule Region	0.5 ± 0.1	~125	Vargas et al. (2011)		

Table 4. Summary table of some earthquakes that have affected the study area (location in bold letter), in addition to other events where coseismic uplift has been measured. Some events affecting the area have been poorly documented and, therefore, no

specific uplift information is available. They are mentioned in Table 3, but have been omitted in this table. Magnitudes M_S and M_W are surface-wave and moment, respectively. Note how, tentatively, areas closer to the trench seem to entail higher coseismic uplift.

For the 1960 Valdivia earthquake, the largest recorded by modern seismology (Plafker & Savage (1970); Cifuentes (1989); Moreno et al. (2009)), Seivers (1963) measured a coseismic uplift of 1.7 m at Isla Mocha in front of the coasts of Arauco Province, Bío-Bío Region, immediately after the earthquake. Later, 1.8 ± 0.2 and 1.0 ± 0.4 m were measured by Plafker & Savage (1970) at the western and eastern coast, respectively, suggesting some landward tilting. South of 38.5°S , 1960 land level changes along the coastline were dominated by subsidence, which reached 2.7 m near the city of Valdivia at 40°S (Plafker & Savage (1970)). For that same event, coseismic uplift of 1.5 m was registered immediately after at Lebu, Arauco Province, Bío-Bío Region (Álvarez (1963)), at the same locality Plafker & Savage (1970) measured 1.3 ± 0.2 m in 1968.

As for the north of Chile, short-term vertical deformation affecting the Mejillones Peninsula was evidenced by geodetic and geological observations following the 1995 M_w 8.1 Antofagasta earthquake. During this event, the area underwent a coseismic uplift of approximately 0.15 - 0.80 m (Ortlieb et al. (1996a)). More observations around the area can be considered as coherent evidence for a strong coseismic uplift that likely occurred during the last 1877 $M_w \sim 8.8$ megathrust earthquake. Specifically, a coseismic uplift of 1.2 m was inferred at Punta Lobería in Mejillones Peninsula (González-Alfaro et al. (2018)).

In addition to these measurements, many more have been registered by different authors. For the M_w 7.7 Tocopilla earthquake in 2007, coseismic uplift of up to ~ 0.34 m was measured (González-Alfaro et al. (2018)). For the 2010 M_w 8.8 Maule earthquake in Central Chile coseismic uplift of $1.3 \pm 0.2 - 2.6 \pm 0.6$ m was measured (Farías et al. (2010); Vargas et al. (2011b); Vigny et al. (2011)).

The observations for the 1960 Valdivia earthquake along with the definition of seismic segments, subsequently led Kaizuka et al. (1973) to propose that the Arauco Peninsula was uplifted by accumulated coseismic uplift during both Valdivia and Concepción earthquakes.

Furthermore, observations of northern Chile and new geodetic data following the 2007 M_w 7.7 Tocopilla event, indicate that coastal uplift results from cumulative coseismic vertical displacement with low subsequent interseismic subsidence recovery driven by both deep-moderate and large megathrust earthquakes (González-Alfaro et al. (2018)).

These observations and conclusions are key in supporting the tectonic analysis that is proposed in this work since, as stated before, the emergence of the different platforms at Punta de Tralca is believed to be triggered by several seismic events, as well as long-term uplift, considering recovery subsidence taking place at interseismic phases. This topic will be addressed in detail in the Discussion section (Chapter Four) below.

1.8 TAFONI

1.8.1 What are tafoni?

In order to explore the age of the geomorphic surfaces along the study area, a review of what tafoni are and how they can help with this endeavor is insightful, since they are vastly present at Punta de Tralca.

The Sicilian word tafoni means “windows” (singular: tafone) and are cavities that form naturally by weathering and erosion in rocks. This type of weathering was first studied in the type locality of Corsica, France. With a variety of shapes and sizes, tafoni typically

develop as groups in highly inclined surfaces along many lithologies and regions around the world (Goudie & Viles (1997)).

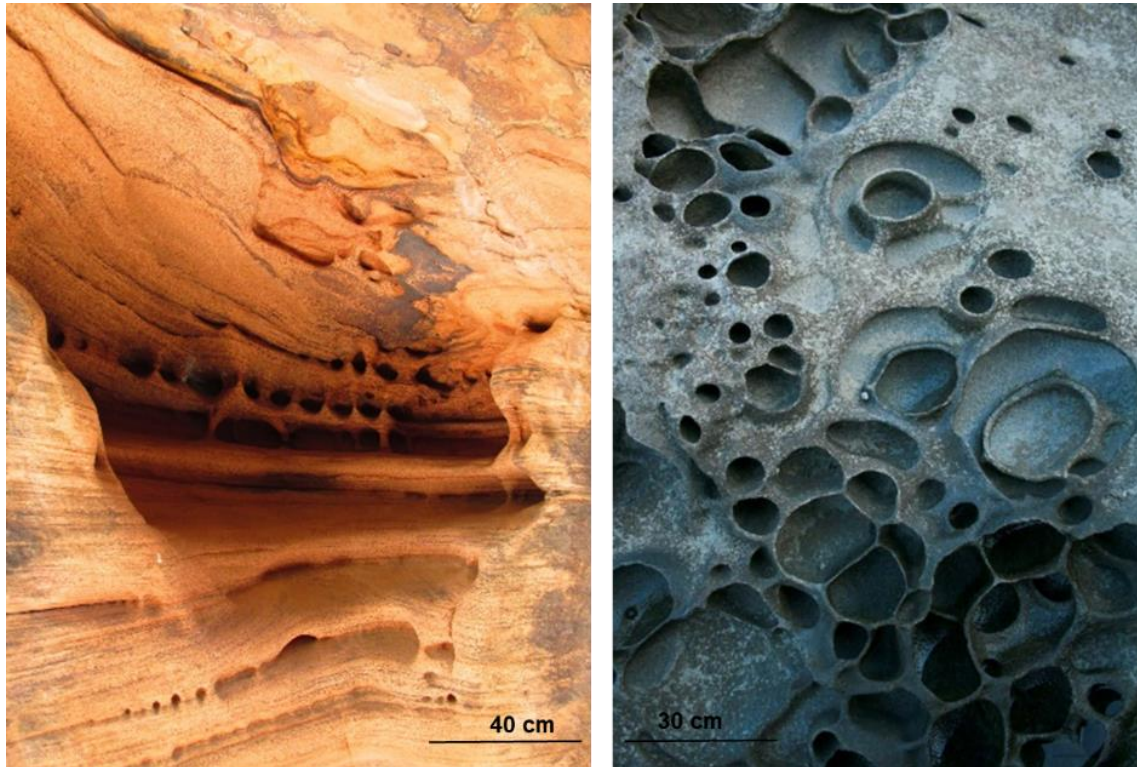


Figure 11. Left: tafoni in sandstone at Zion National Park, Utah. Photo by the author. Right: honeycomb tafoni and some nest tafoni at Koh Kut, Thailand; photo by Jennifer Bright obtained from <https://fineartamerica.com/featured/rock-erosion-3-koh-kut-jennifer-bright.html?product=beach-towel>.

Tafoni typically form in spherical and elliptical shapes, have arched-shaped entrances, concave inner walls, overhanging visors and gently sloping debris-covered floors (Goudie (2003)).

The size can range from few cm to several meters in diameter and depth. They can be isolated hollows or interconnect with time. Closely spaced tafoni development leaving narrow intricate walls between them, is termed “honeycomb weathering” (Figure 11,

Figure 12), in which case the hollows are no larger than 1 meter and are called alveoli instead of tafoni. Nonetheless, the relationship between both has not been clearly defined so the distinction is one of size and shape only.

Another feature that can be developed from this form of rock decay is “case-hardening”. Induration of the surface of rocks, especially siliceous sandstones, occurs through the accumulation of silica, carbonate, or iron oxides (Merrill (1906)). This forms a cemented and more resistant layer -relative to the rest of the rock- that comprises the “overhanging visors” mentioned above and shown in Figure 13.

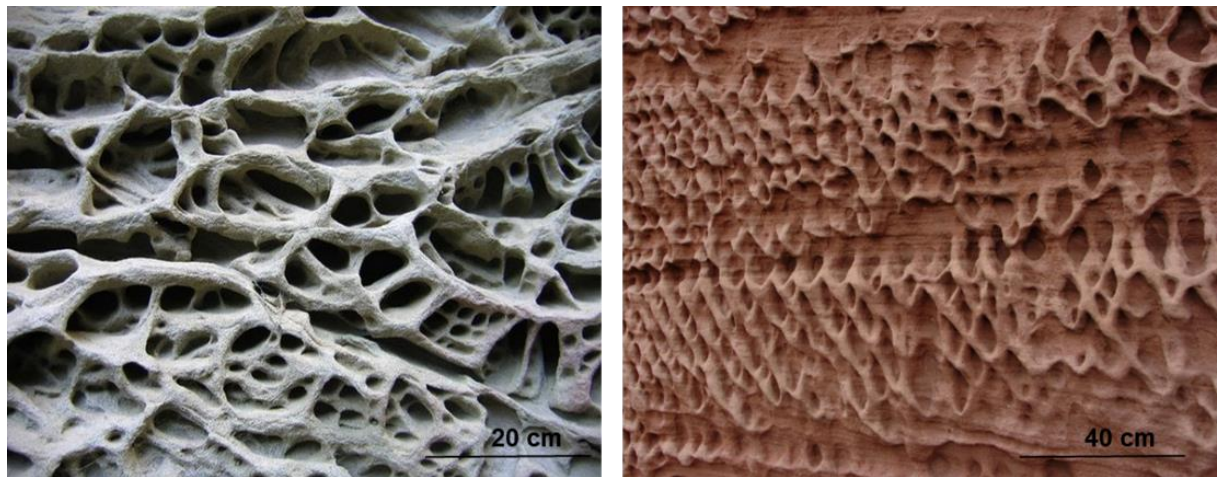


Figure 12. Left: intricated tafoni pattern at El Corte de Madera Creek; photo by Dawn Endico obtained from <https://www.flickr.com/photos/candiedwomanire/84148980/>. Right: Honeycomb tafoni in sandstone at Drachenfels, Wabenverwitterung, Germany. Photo from <https://mapio.net/pic/p-14183158/>.

Regarding possible locations for tafoni development, they are most prolific in salt-rich environments, and have also been documented in deserts (McGreevy (1985)) and coastal areas (Mottershead & Pye (1994)), which have high salt concentrations and occasional to frequent desiccating conditions in common. They can also be found in different types of rock such as sandstone, limestone and in medium and coarse-grained granites, along

with tonalites, dolerites, lacustrine silts and conglomerates. It appears to be that only rocks with relatively closely spaced discontinuities (bedding planes, foliation and joints) such as shales and slates, are “safe” from these cavernous weathering forms.

Goudie (2003), defines two types of tafoni: basal and side-wall. As the name states, basal are found on ground level or along discontinuities (where weathering rates are relatively greater), whereas side-wall tafoni develop on highly inclined or vertical surfaces. Martini (1978) concluded that minor structural variations may control the initial zone of tafoni development, such as small fractures. Also, tafoni can develop and propagate easier in high permeability areas like along lithological contacts, bedding planes or even around concretions.

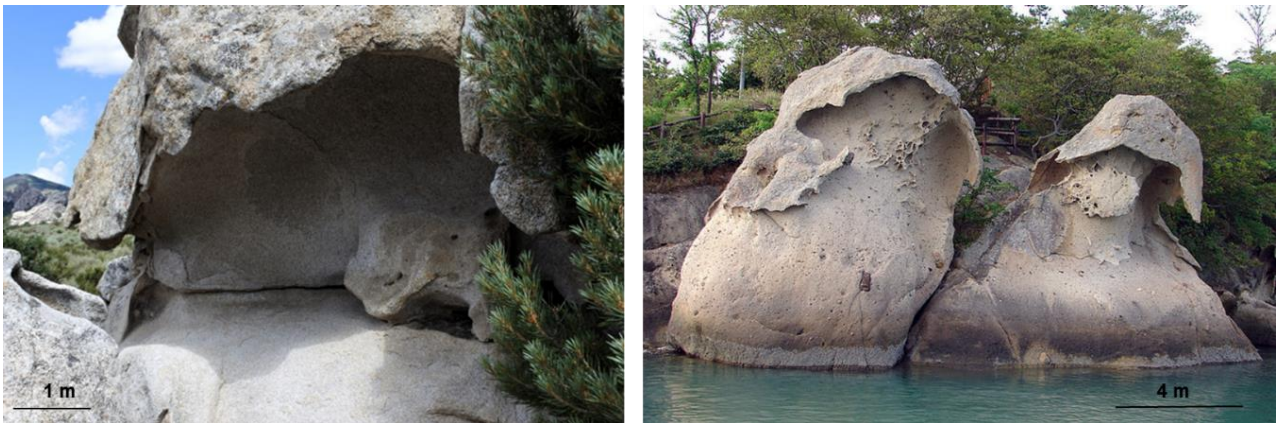


Figure 13. Left: Tafoni and case-hardening in Almo Granite, Idaho; photo by Mark Wilson obtained from <http://woostergeologists.scotblogs.wooster.edu/2017/07/26/>. Right: Tafoni and case-hardening in sandstone at South Jeolla in South Korea; photo obtained from <https://creativecommons.org/licenses/by-sa/3.0>.

Also, Smith and McAlister (1986) propose a positive feedback on tafoni development: the recently created hollow provides a more suitable environment for weathering, thus, for its growth. In the contrary, Matsukura & Matsuoka (1991) suggest a negative feedback

relationship where, as tafoni develop, exposure of the depressions decrease so that desiccation necessary for salt weathering occurs less often.

Although early studies of cavernous weathering indicate that caverns were created by the action of the wind, it is now known that the main processes involved in its formation include insolation weathering, wetting and drying weathering, frost weathering, chemical weathering of mineral content, and salt weathering. The importance of the later is evidenced by the presence of salt crystals on walls (and cavern floors and cracks) of both coastal and desert tafoni and alveoli (McGreevy (1985); Matsukura & Matsuoka (1991); Mellor et al. (1997)), as well as in Antarctica (Wellman & Wilson (1965)).

Salt is responsible for chemical and mechanical weathering in tafoni formation. It increases the solubility of silicates in wet conditions and it crystallizes along fractures during dry periods, causing flaking and removal of mineral grains (Mustoe (1982); Young (1987)) generating these particular features among rocks.

1.8.2 Tafoni as indicators of time

Cavernous or tafone weathering of crystalline rocks is considered a curiosity, despite its global distribution. Although many descriptive terms and classifications have been proposed and used by different authors, it has not been strictly defined in the literature and it is complex enough to generate debate about its formation and processes for many years.

The first reference of tafoni in history is F.F. Tuckett's description of these cavernous features while visiting Corsica (Tuckett (1884)) the actual type locality. Early attempts to explain these weathering forms range from aeolian erosion to abrasion by snow in polar regions (Blackwelder, 1990). Later in time, chemical weathering was studied and accepted as a major process in tafoni formation (Dragovic (1969); Twidale (1976)). It is

also agreed nowadays that besides lithology, salts, climate and exposition, an arid period during the year is essential for the formation of tafoni. That aside, major controlling processes for tafoni weathering are still poorly understood (Huinink et al. (2004)) as well as weathering rates.

Some publications propose equations for the temporal development of tafoni of known maximum ages (Matsukura & Matsuoka (1991); Sunamura (1996); Norwick & Dexter (2002)). Matsukura & Matsuoka (1991) calculate tafoni ages indirectly considering uplift of coastal platforms, although it is possible that tafoni began developing after the uplift of those platforms. Their data also show how tafoni develop more effectively during the initial phase rather than the mature phase, i.e., growth rate decreases exponentially with time as shown in the Equation (1):

$$z = 20.3 [1 - \exp(-0.005t)], \quad (1)$$

where z is the depth of the tafoni (in centimeters) and t is the time (in years). They study tafoni on a cliff face of an uplifted shore platform developed in Miocene tuffaceous conglomerate, and determine a maximum develop rate of 1.67 mm/a. Other authors have also calculated tafoni development rates in coastal areas (Table 5), although none of them studied tafoni development in intrusive -therefore, more resistant- rocks.

Area	Lithology	Rate (mm yr ⁻¹)	Period (years)	Remarks
Gourmalon, Clion-sur-Mer, France (1)	Crystalline schist	1.1 (max)	62 (1898–1960)	Honeycombs on blocks in a sea wall.
Aoshima, Miyazaki, Japan (2)	Pliocene sandstone	5.2 (max)	20 (1951–1971)	Tafoni-like depressions on a masonry bridge pier.
Otway, Victoria, Australia (3)	Cretaceous greywacke	a few (max) ^a	38 and 32 (1943/9–1981)	Honeycombs on sea walls.
near Bellingham, Washington, USA (4)	Arkose	.6 ^b	78 (1903–1981) ^c	Honeycombs on a sea cliff.
Nojima-zaki, Boso Peninsula, Japan (5)	Miocene tuffaceous conglomerate	1.7 (max)	66 (1923–1989)	Tafoni on a cliff face of an uplifted shore platform.
Weymouth, Dorset, UK (6)	Jurassic oolitic limestone	0.03 (mean)	135 (1855–1990)	Honeycombs on columns of a hotel entrance.
Westone-super-Mare, Avon, UK (7)	Lower Cretaceous sandstone	>1	105 (1888–1993)	Honeycombs on coping stone of sea walls.
Aoshima, Miyazaki, Japan (8)	Pliocene sandstone	2.2 (max)	18 (1971–1989)	Remeasurement of Takahashi's (1975) site.

Table 5. Time-averaged rates of coastal tafoni development. Sources: (1) Grisez (1960); (2) Takashi (1975, fig. 18); (3) Gill et al. (1981); (4) Mustoe (1982); (5) Matsukura & Matsuoka (1991); (6) Viles & Goudie (1992); (7) Mottershead (1994); (8) Takahashi et al. (1994). ^a Based on pls. 10 and 11. ^b Calculated from tafoni depth in this study. ^c The year 1981 from G. E. Mustoe (1991, pers. commun.). Table obtained from Sunamura (1996).

Sunamura (1996) proposes another equation (Figure 15) for tafoni development rate in coastal environments, considering a time lag between the exposure of the rock and the initiation moment of a tafone (see conceptual evolution model depicted in Figure 16). In order to use this equation, a weathering profile of the affected rock must be obtained and studied in thin section so the depth of the weathering front in the rock, z_c , (and subsequent mineralogy) can be determined. Also, a rock strength (S) profile over time is implicitly considered in the equation, like the one presented in Figure 14. This profile is obtained from the Equation (2):

$$S = (S_0) \exp[-A(z - z_c)^2 t] \quad \text{for } 0 \leq z \leq z_c, \quad (2)$$

where S is rock strength, t is time, S_0 is the rock strength at the initial stage ($t = 0$), A is a constant with a unit of $[T^{-1}L^{-2}]$, z is the depth that is positive inwards from the surface of rocks, and z_c is the critical depth where the weathering front is. Another implicit variable considered in Equation (2) is a strength reduction coefficient, k , with a unit of $[T^{-1}]$. This variable is related to S according to Equation (3):

$$S = (S_0)exp(-kt), \quad (3)$$

that represents the initial conditions of weathering, where $S = S_0$ at $t = 0$. The validity of Equation (3) was examined by Oguchi et al. (1994), through the investigation of temporal change in mineralogical, chemico-physical, and mechanical properties of rhyolite by weathering in a humid, temperate region of the Pacific. He tested the properties of different rhyolites (erupted in different times) at the same area, such as compressive and tensile strengths, using both dry and wet rock specimens. From this analysis, Oguchi et al. (1994) obtained data that fit the curve from Equation (3) and determined values for S_0 and k in both compressive and tensile-strength cases. It is important to highlight that Sunamura (1996) considers the functional form of k rather than the specific value experimentally obtained by Oguchi et al (1994). Also, since many forces and processes affect the rock with different intensities, it is arduous to specify which strength parameter, compressive or tensile, best describes the resistance against these multiple forces. Sunamura (1996) applies Equation (3) without specifying this.

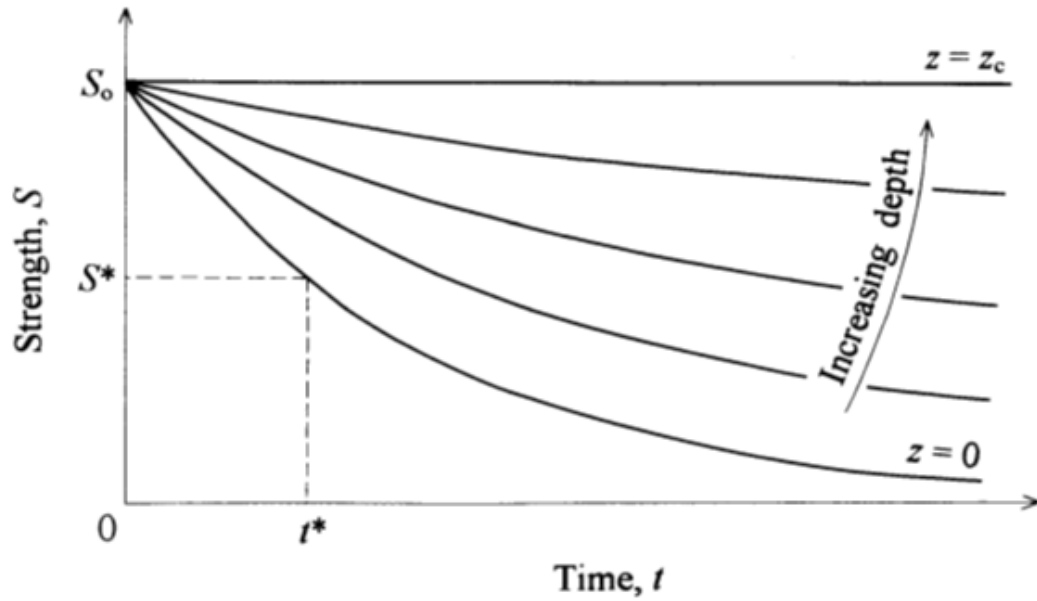


Figure 14. Schematic diagram showing equation (2) that describes the reduction in rock strength with time t and depth z ; t^* is the time when the rock surface ($z = 0$) attains the critical strength S^* for the onset of mechanical breakdown. Figure obtained from Sunamura (1996).

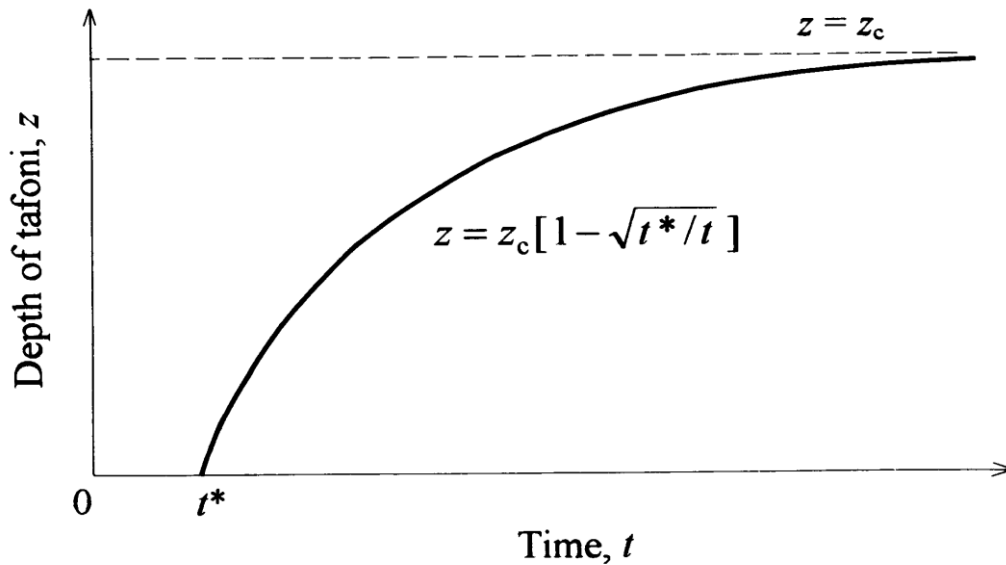


Figure 15. Temporal change in tafoni depth and respective equation, where z is the depth of the tafoni, z_c is the depth of the weathering front, t is time and t^* is the time

when the rock's strength or resistance to weathering is critical and the tafoni starts to grow. Obtained from Sunamura (1996).

Conca & Rossman (1985) studied tonalite cavernous weathering in Catavina, Baja California, US. Hardness testing was measured using an abrasion resistance hardness tester (ARHT) developed for that purpose. This instrument abrades the material by means of a diamond coring bit turning slowly using a constant-torque motor under constant normal force. The measured time required to abrade to a fixed depth is related to the abrasion resistance of the material. The hardness value of a material, Ha , and the coefficient of relative hardening for an exterior surface, C [dimensionless], are defined in their work. Ha is dependent on several factors that combine to determine the resistance to abrasion, such as the kinetic coefficient of friction, average mineral hardness and the character of the intergranular bond.

Ha was found to be 50×10^5 [N-sec/m] for an unweathered granitic rock. Conca & Rossman (1985) also present an empirically obtained curve for the relationship between Ha and kaolinite content, since its presence indicated weathering conditions in their study (Conca & Rossman (1985), Fig. 5). Abrasion resistance hardness values vary inversely with kaolinite contents, suggesting that kaolinite formation is related to changes in the rock's physical properties. Small variations in the amount of kaolinite produce large differences in the hardness.

Brandmeier et al. (2010) attempted to model tafone weathering considering not only processes but timescales and the nature of the salts involved. In order to do that, geomorphological, geochemical and micromorphological data had to be integrated in the model. They conclude that differences in lithology, microfracturing, properties of the circulating solution, alteration and cementation modify weathering rates, but the impact cannot be accurately quantified. Also, after statistical analysis, they suggest there is no relation between altitude (a.s.l.), distance to the sea and size of the weathering form.

Hence, they cannot propose a single “typical” growth function for different climatic and lithologic settings.

The determination of mathematical modelling for tafoni growth, as described in this section, comprises a challenging problem to which there is no unique and absolute solution. While rock strength can be easy to test, strength profiles are harder to build. Quality data and methodological strictness is necessary in order to attempt a minimal error modelling for this multi-variable type of weathering process.

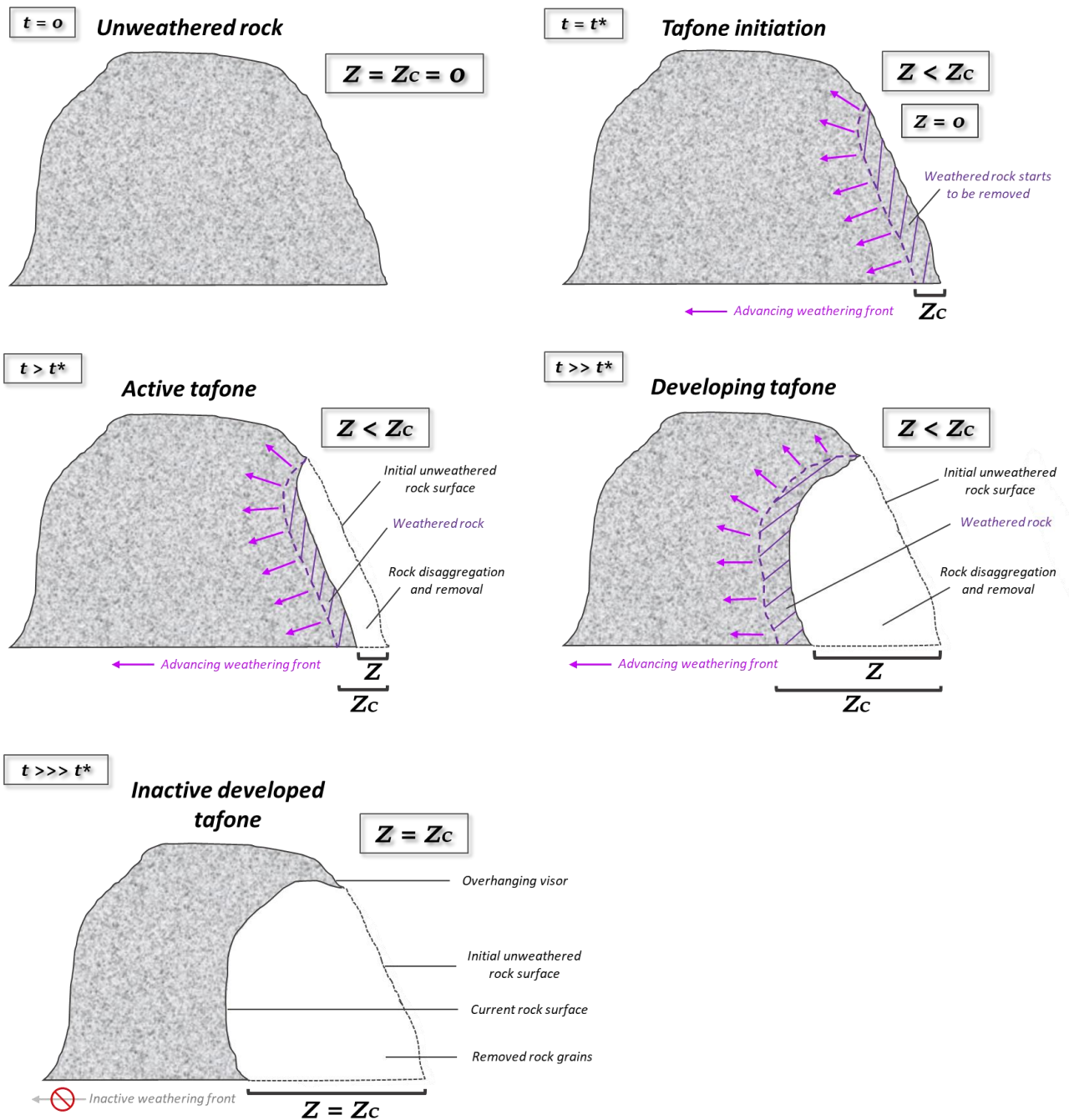


Figure 16. Conceptual tafone evolution model based on Sunamura (1996), from an unweathered rock at $t = 0$ to an inactive well-developed tafone at $t \gg \gg t^*$, where t is time, t^* is the time where the rock is sufficiently weathered for removal of disaggregated material to start, z is the depth of the tafone (surface of the cavernous form in relation to the original unweathered surface at a certain time t), and z_c is the advance-depth of the weathering front in relation to the original unweathered surface. Note that z_c must be greater than z in order for the tafone to be active. If $z = z_c$, the tafone becomes inactive.

2 CHAPTER TWO: METHODS AND INFORMATION SOURCES

The methodology of this thesis can be divided into desktop and field work being both complementary and necessary for the established purposes.

The first part of the desktop work consists of reading, studying and interpreting the available literature. Articles about geomorphology, tectonics, geologic maps and sections regarding the study area and its surroundings, may be useful to establish an historic tectonic context to work with.

The second part consists of field work campaigns in which data collect is the main goal. Aerial photographs and videos obtained from two different drone flights -DJI Phantom 4 and DJI Mavic Air- can be used to develop a method called “structure from motion”, in which digital elevation models are built using a software like Agisoft PhotoScan. Complementary ArcGIS usage is also key for photogrammetry. In addition to this type of information processing, classic field work techniques are required such as: exploration, mapping, description, photography and sample collection.

Finally, more desktop work is necessary in order to analyze and interpret the data obtained from field work and therefore, quantify and characterize recent tectonic activity, tafoni development in the area, develop maps, topographic profiles, and a neotectonic review for the study area.

2.1 GEOLOGICAL MAPS

The regional geology of the study area and its surroundings was firstly reviewed from the following publications:

- a. Mapa geológico del área de Valparaíso-Curacaví; SERNAGEOMIN (1996), at 1:100000.
- b. Mapa geológico del área de San Antonio-Melipilla; SERNAGEOMIN (1996), at 1:100000.

2.2 SATELLITE IMAGES

As a first approach, images from Google Earth software were analyzed (Figure 17) to provide an overview of the general area. Nonetheless, the resolution available for the peninsula, specifically, was not adequate for fulfilling this thesis' goals. All the maps presented here were developed from high resolution drone imagery instead.

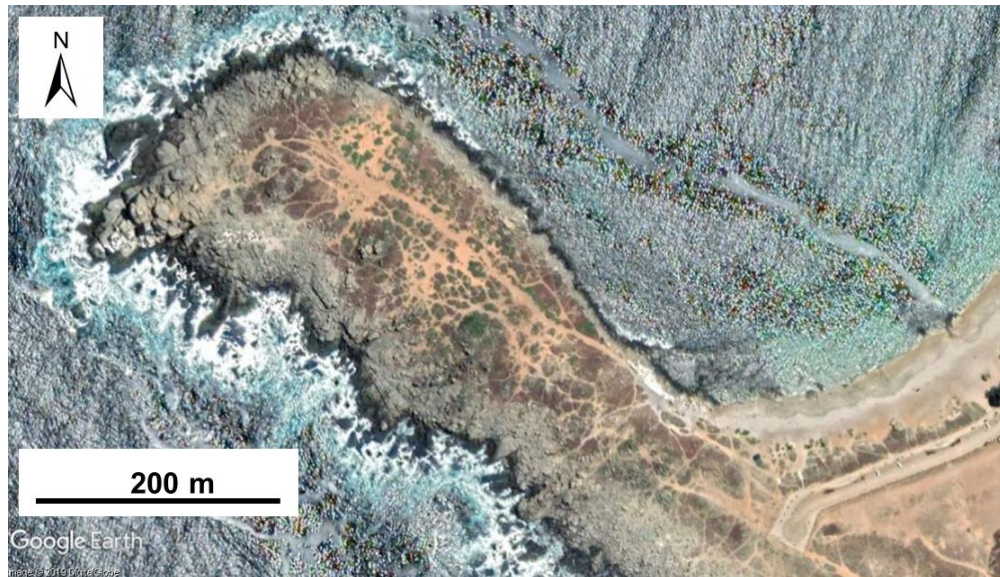


Figure 17. Satellite image of the study area obtained from Google Earth.

2.3 DRONE IMAGERY

In two of the fieldtrips to Punta de Tralca Peninsula, drone images were obtained in order to get high resolution imagery and consequent quality 3D models through the methodology known as Structure from Motion (SfM). With the SfM technique, 3D objects can be represented through high resolution overlapping images taken from different

perspectives. This technique has been broadly used in the engineering and geosciences fields. In this work, two different drones were used: a DJI Phantom 4 drone for the first flight by Gregory De Pascale, and a DJI Mavic Air drone for a second flight by Nicolás Bueno-Core. Two different scale models for each flight were developed: the first flight was done over the whole Punta de Tralca Peninsula, whereas the second flight was done over the seaward end of the peninsula where the distinct platform sequence that comprises the main feature of the study area is located. Both models were developed using the same methods. Some screenshots of the processing for the second model (DJI Mavic Air) are shown below in order to depict the structure from motion method.

Firstly, a flight route was planned and programmed for the drone. This route determined a grid for the image capture (Figure 18). Control points obtained with regular GPS in the field can be taken in order to refine the model horizontal coordinates and elevation (Figure 19). Secondly, the images were processed with the software Agisoft PhotoScan, generating a disperse point cloud of 84.397 points (Figure 19) and a dense point cloud of 6.105.158 points (Figure 20), from which a DEM was generated (Figure 24).

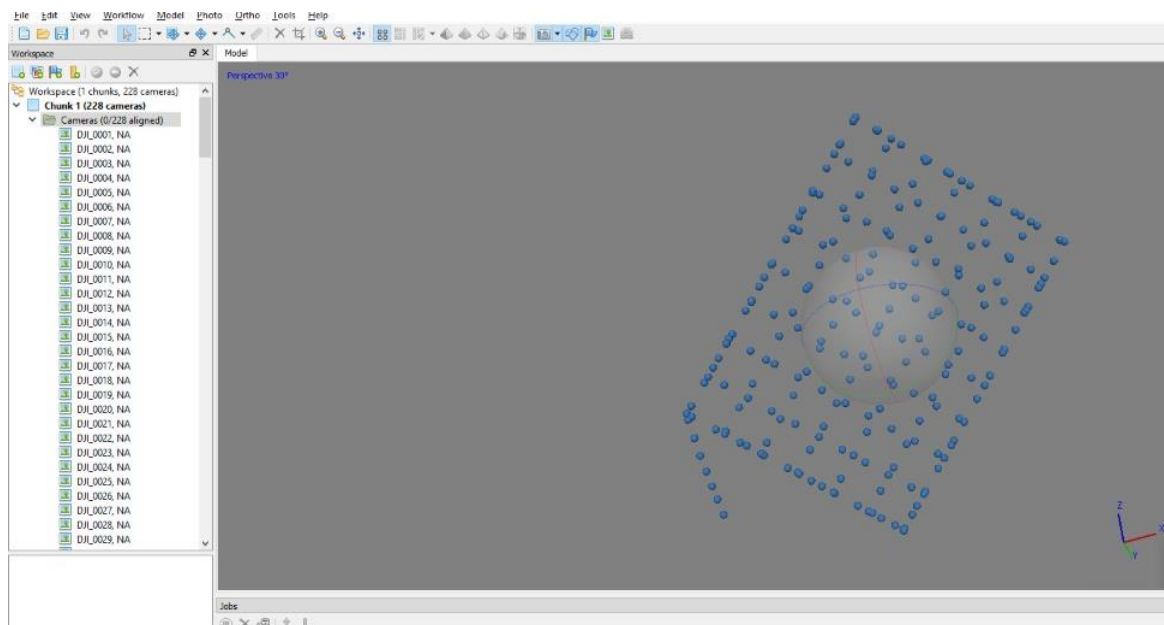


Figure 18. Screenshot of the grid generated from the flight route of the drone, where the blue dots are locations of the orthophotos taken by the drone.

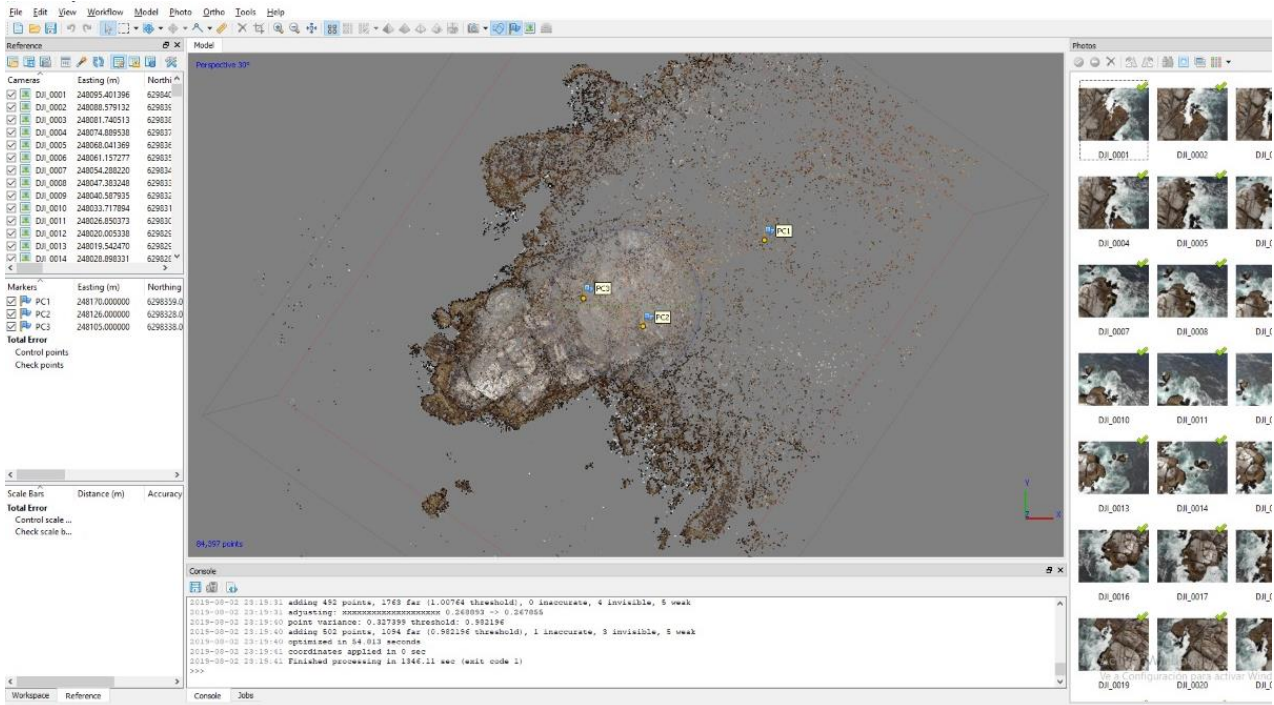


Figure 19. Screenshot of the generated disperse point cloud, with some control-points (PC1, PC2 and PC3) taken in the field with a Garmin GPS, so as to refine the model coordinates.

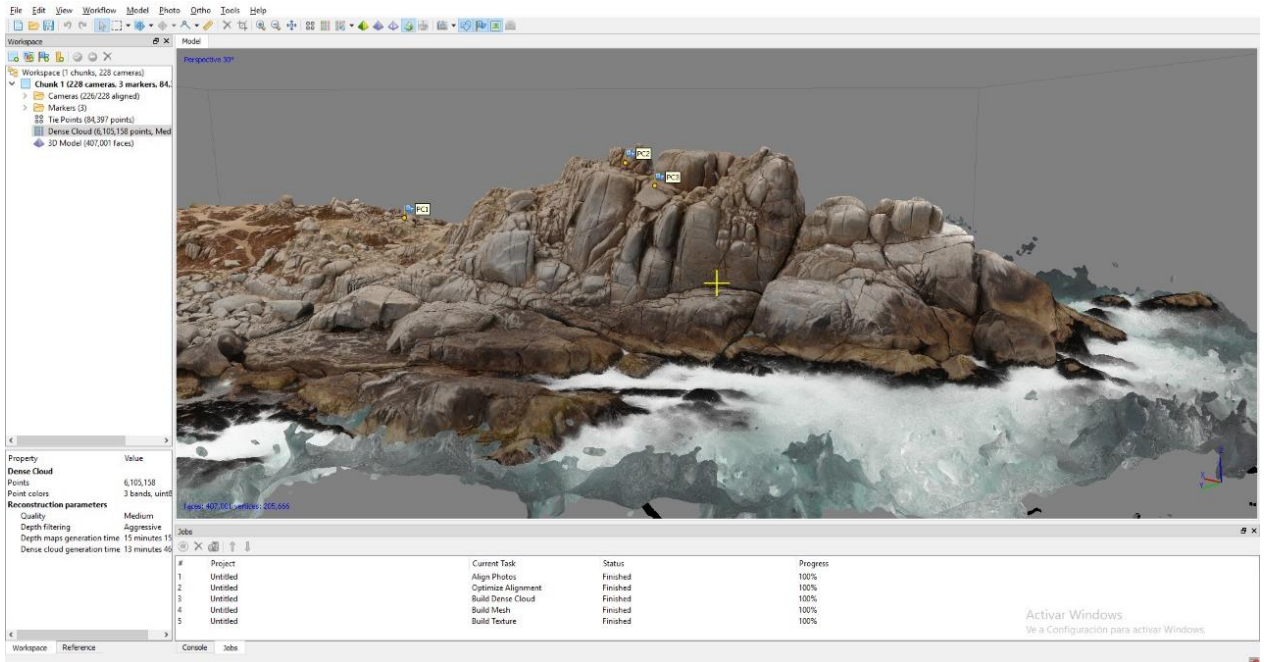


Figure 20. Screenshot of the generated dense point cloud, showing control-points PC1, PC2 and PC3.

With the described methodology, two final models -from the two mentioned drone flights- were developed. The first model corresponds to the whole Punta de Tralca peninsula and a resolution of 26.7 cm/pix was achieved from 246 integrated images (Figure 21). The second model at the seaward end of the peninsula has a resolution of 4.7 cm/pix achieved from 231 integrated images, and was obtained flying at an altitude of ~ 85 m (

Figure 22).

Both models have minimal horizontal (x and y coordinates) error; however, error related to current sea level can reach up to 5 m (sea level calculated by the software would appear to be 5 m under actual sea level). This error has been manually corrected considering level “cero” as the observed mean sea-level in videos, imagery and directly on the field. Tidal at the area has been studied and it is concluded that there are no significant variations to be considered in this work according to the work-scale, and therefore would not comprise a bias in the analysis. Relative height errors (for instance, distance between platforms) have been studied and, according to fieldwork measurements, are proved to be minimal.

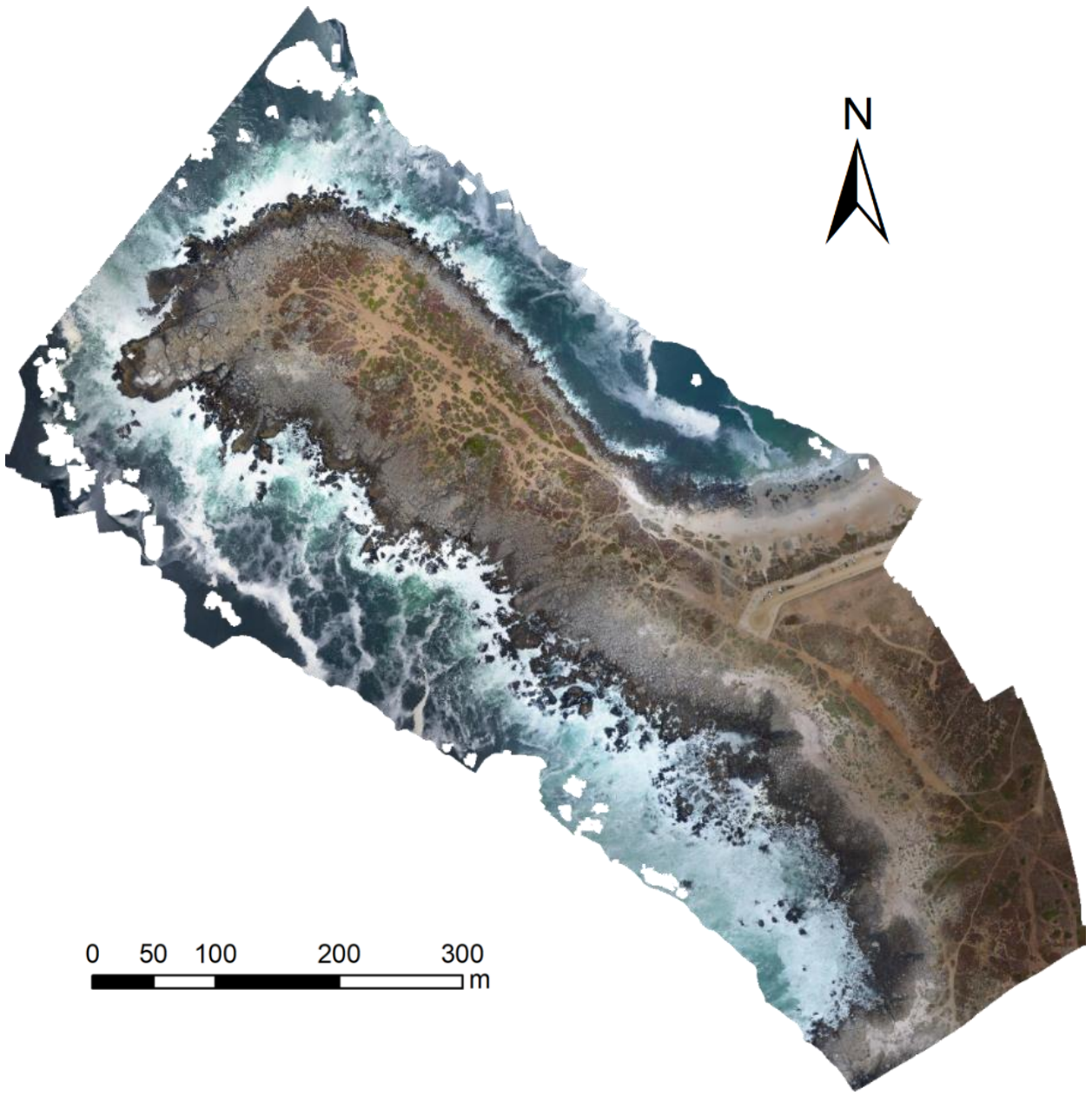


Figure 21. Orthophoto of Punta de Tralca peninsula obtained from the first drone flight during fieldwork. Image resolution is 26.7 cm/pix. Drone used was a DJI Phantom 4. Field photo by Gregory De Pascale.

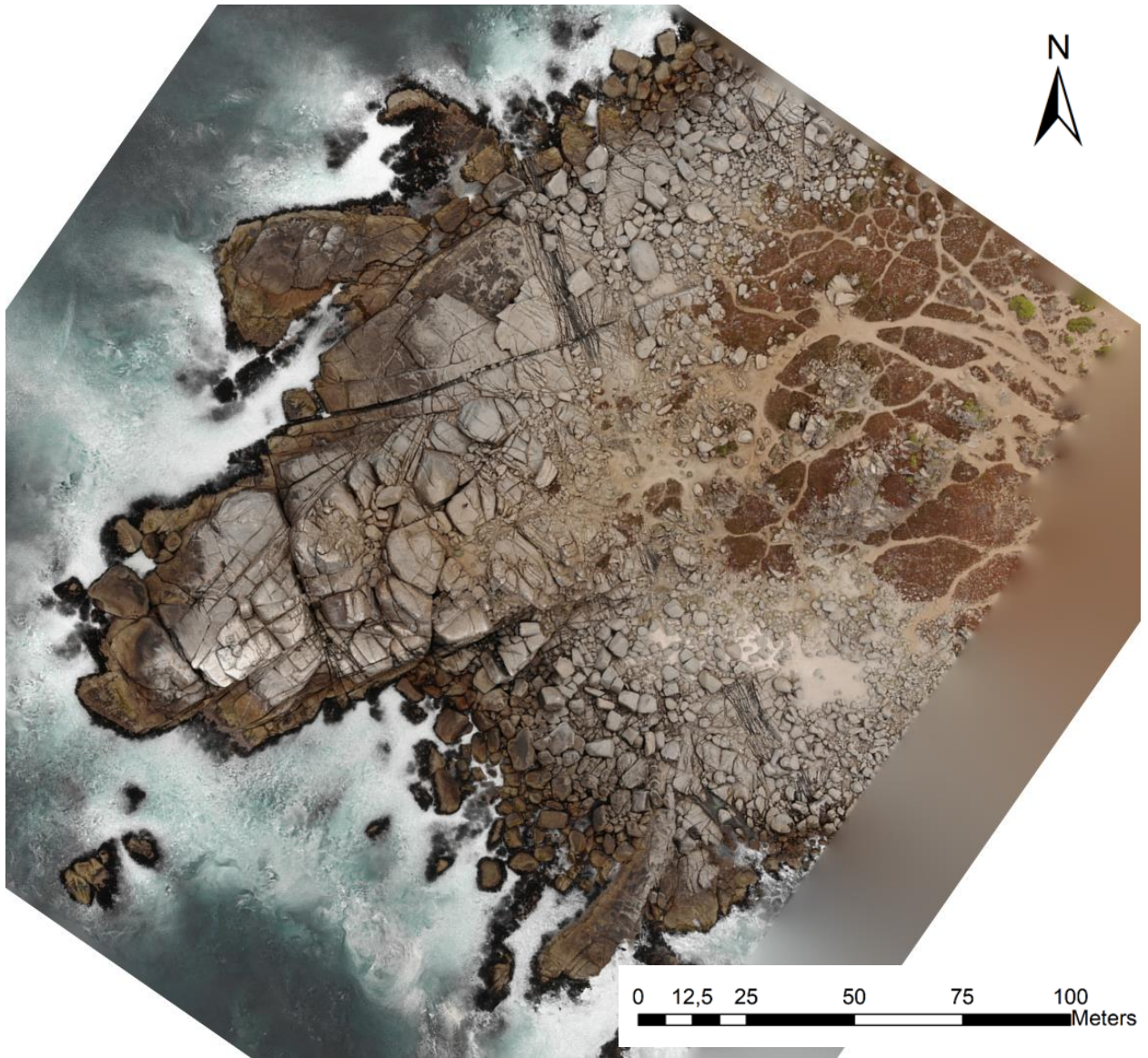


Figure 22. Orthophoto of Punta de Tralca peninsula obtained from the second drone flight during fieldwork. Image resolution is 4.7 cm/pix. Drone used was a DJI Mavic Air. Field photo by Nicolás Buono-Core.

2.4 TOPOGRAPHIC DATA

From the images obtained by the drone flights and subsequent processing in Agisoft PhotoScan and ArcGIS software, two DEMs were prepared: one from the first drone flight

(Figure 23) and two from the second flight with a resolution of 4.86 cm/pix and point density of 423 points/m² (Figure 24 and Figure 25). Additionally, a slope map from the seaward end of the peninsula was obtained from the second DEM (Figure 26). Models shown in Figure 23 and Figure 25, show some height data scatter where current shoreline is, due to wave action (unstable surface).

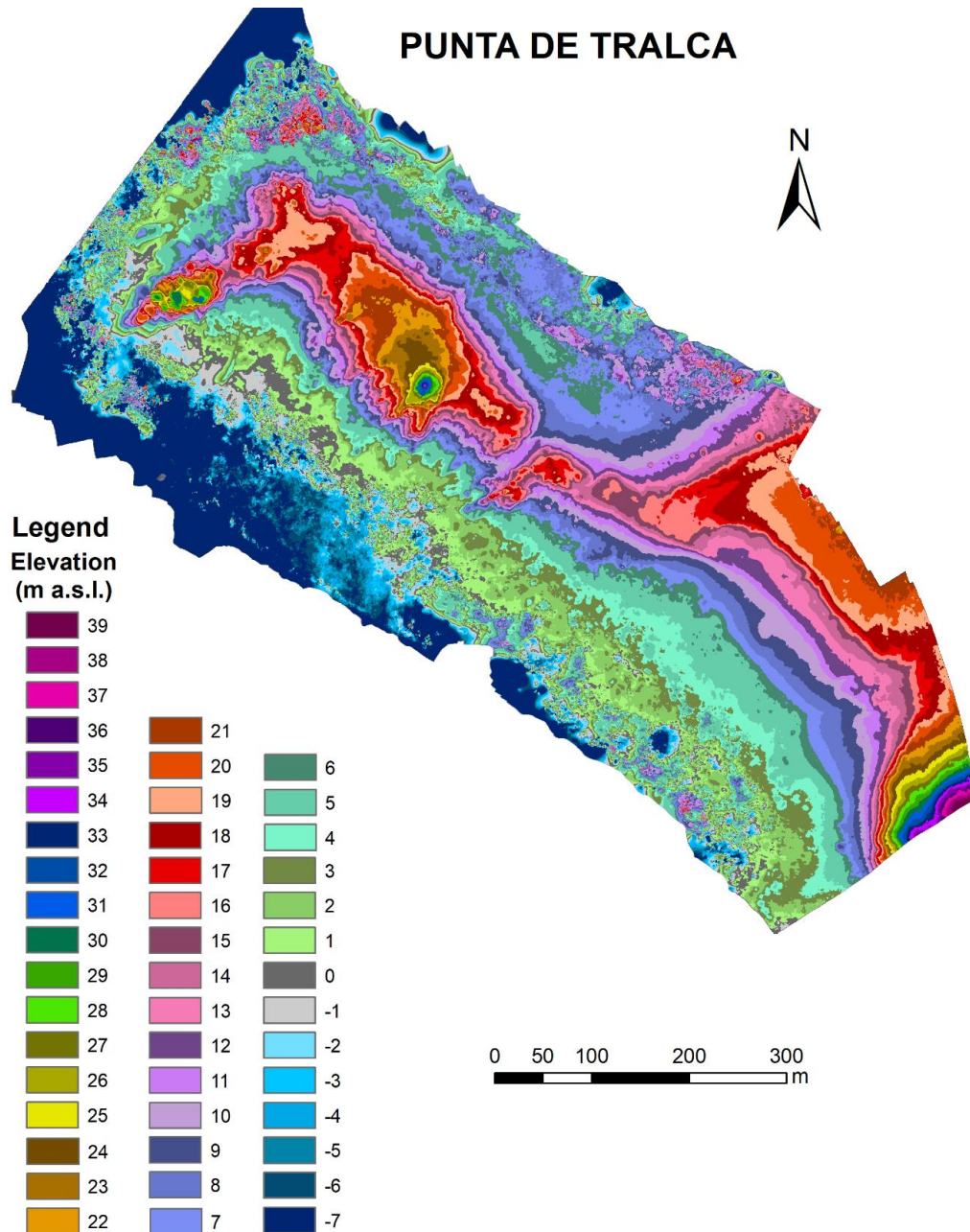


Figure 23. DEM of the whole study area obtained from first drone flight using a DJI Phantom 4 drone. Flight by Gregory De Pascale. Legend has been modified for achieving better visualization of elevation data.

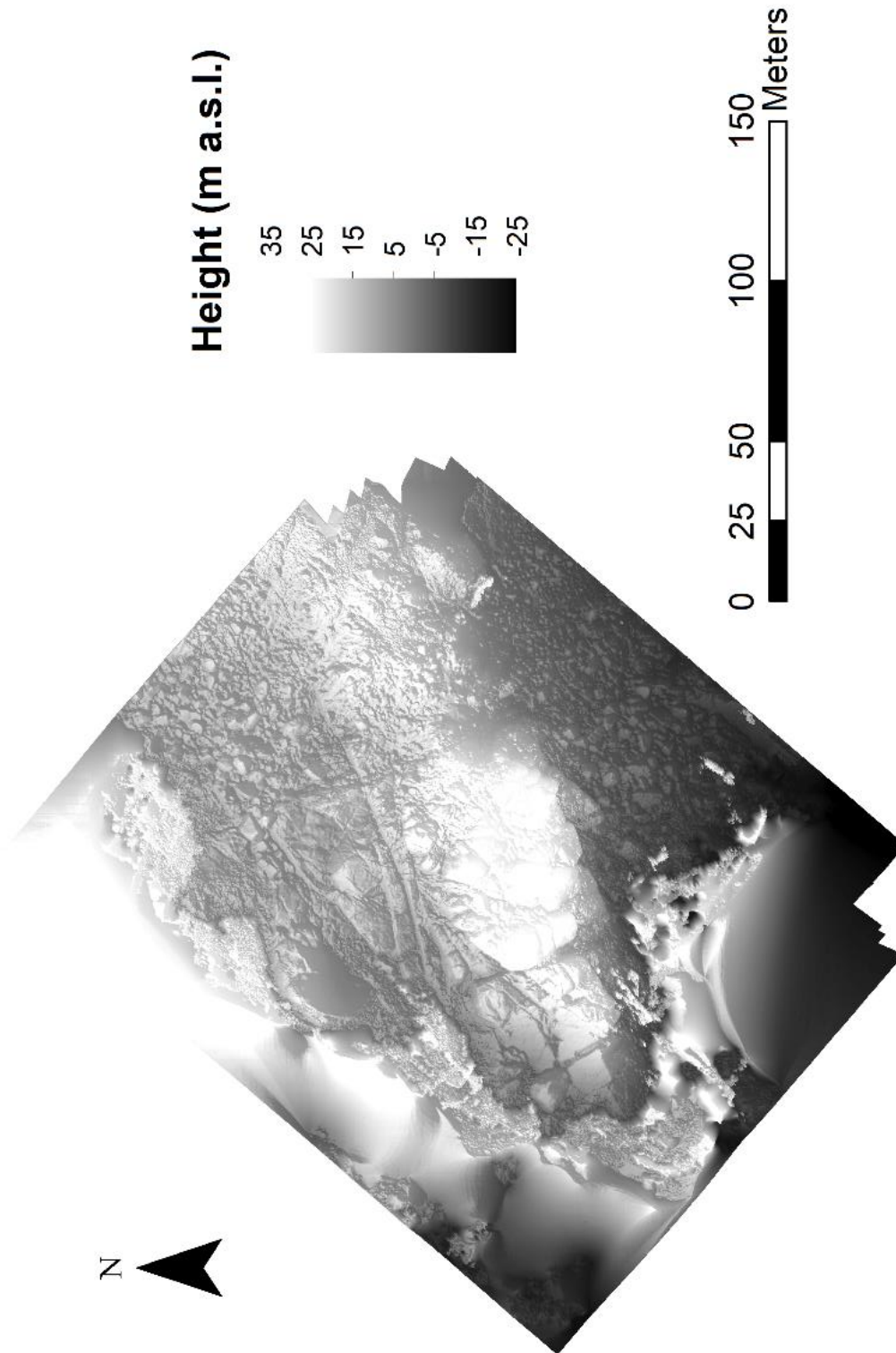


Figure 24. DEM of the seaward end of the peninsula, obtained from second drone flight using a DJI Mavic Air drone. Flight by Nicolás Buono-Core. Hill shade effect has been applied for achieving a more realistic view of the topography.

PUNTA DE TRALCA

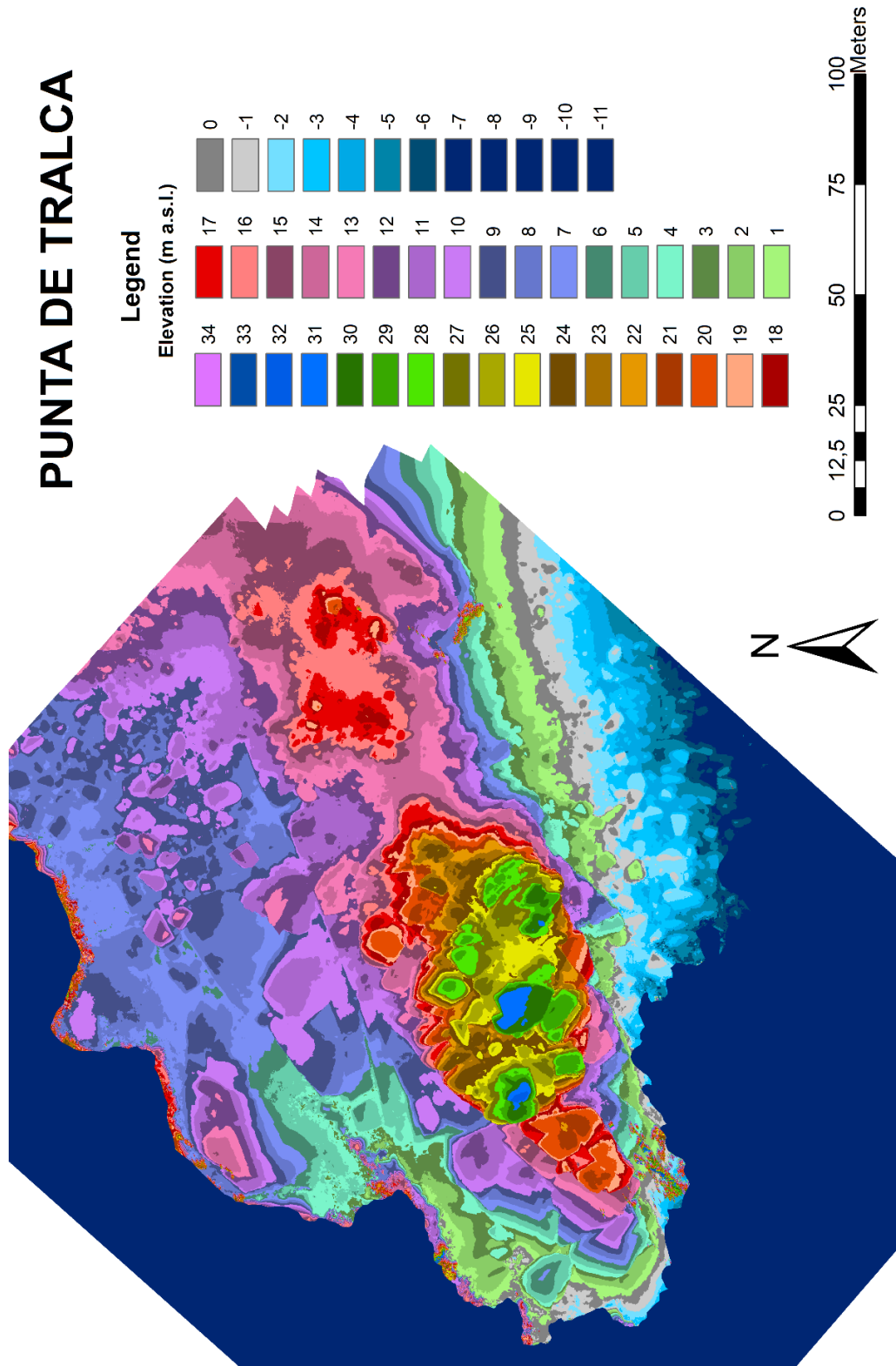


Figure 25. DEM of the seaward end of the peninsula obtained from second drone flight using a DJI Mavic Air drone. Flight by Nicolás Buono-Core. Legend has been modified for better visualization of elevation.

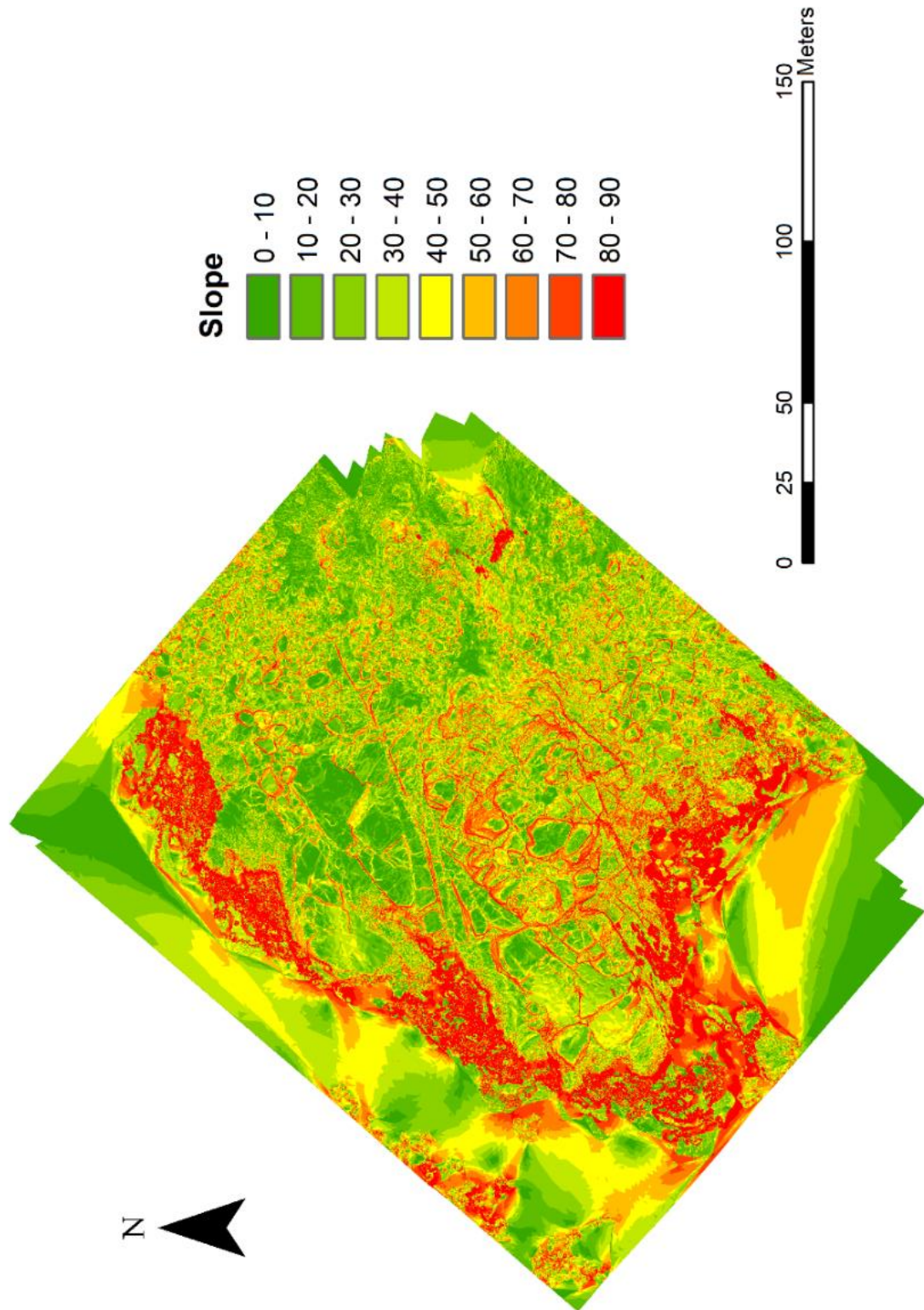


Figure 26. Slope map of the seaward end of Punta de Tralca Peninsula obtained from second drone-flight DEM model. Drone used was a DJI Mavic Air drone. Flight by Nicolás Bueno-Core.

3 CHAPTER THREE: RESULTS

3.1 PLATFORMS

One of the main features of the study area is the sequence of platforms or levels carved in the tonalite rock seen from almost every spot around Punta de Tralca beach.

In order to facilitate further analysis, every level has been mapped out according to the overall characteristics and extension of each platform. Using high resolution images, videos and elevation models obtained from drone flights during different fieldtrips, platform levels were identified and mapped. In this section, two maps from the study area are presented: Figure 27 corresponding to an overall view of Punta de Tralca Peninsula and Figure 28, showing a detailed platform mapping at the seaward-most area of the peninsula. Also, pictures from different perspectives have been edited and interpreted in order to facilitate the visualization of the area.

Seven platforms were recognized: P1, P2, P3, P4, P5, P6, and P7, where P1 is the highest, P6 is the lowest right above sea level, and P7 is currently being eroded by wave action and is shallow enough so seaweed cover can be seen in some areas (Figure 29). Height ranges, covering area and main features for each platform are shown in Table 6. Additionally, different elevation profiles from DEMs were made (Figure 30 and Figure 31 in this section, and Figure 56).

As shown in Figure 27 and Figure 28, P1 (red polygons) comprises a discontinuous ~ 590 m² surface of relict spaced blocks seen at the seaward end of the whole peninsula, in addition to an isolated hillock at the middle of it that actually resembles a pile of eroded blocks when climbing to the top of it.

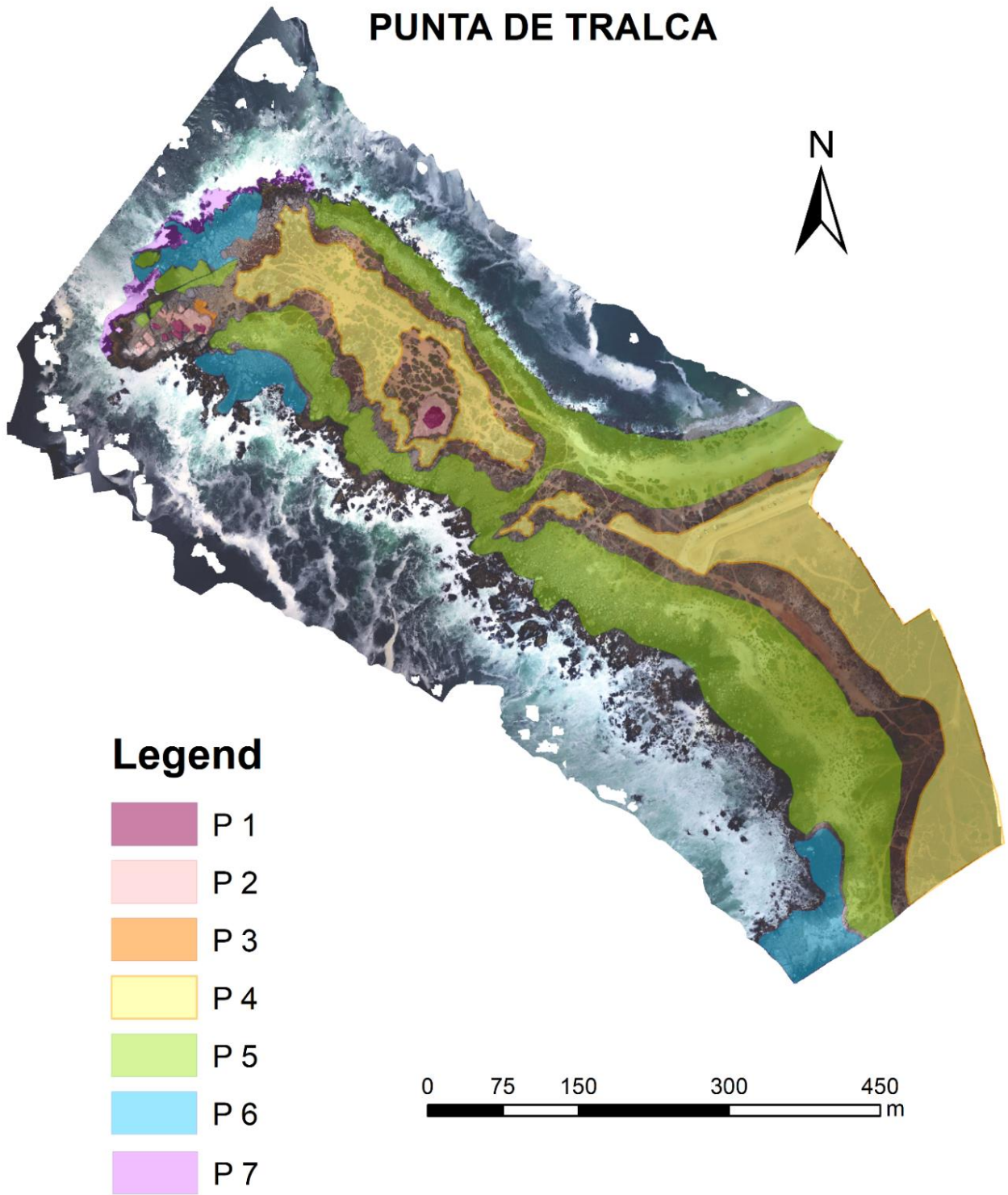


Figure 27. Punta de Tralca Peninsula platform map 1:5000. Basemap obtained with high resolution drone imagery from first flight. Drone used was a DJI Phantom 4. Flight by Gregory De Pascale

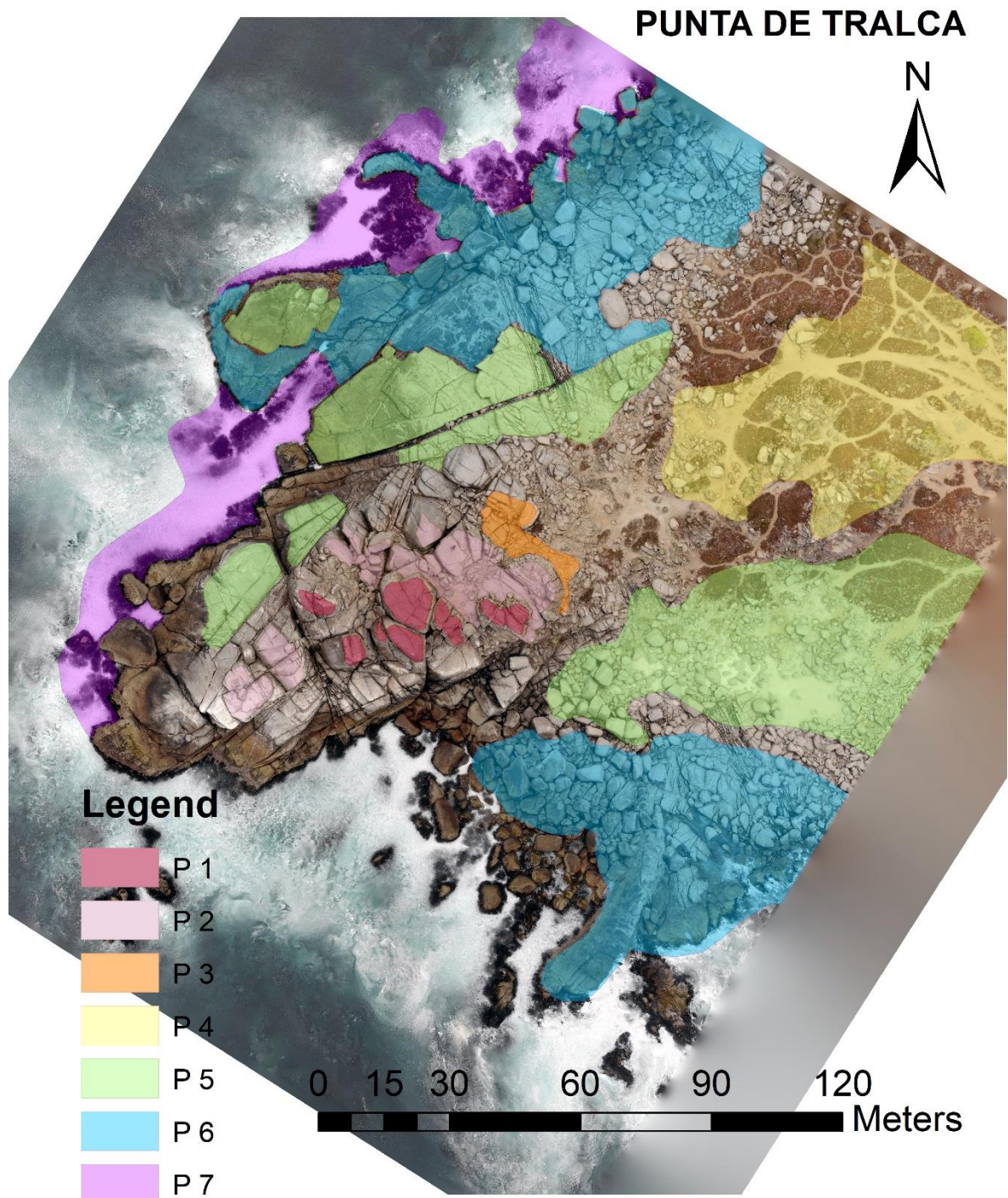


Figure 28. Platform map of Punta de Tralca Peninsula seaward end, 1:1000. Platforms from P1 to P7 correspond to the highest and lowest levels, respectively. Unedited orthophoto obtained with DJI Mavic Air drone; flight by Nicolás Bueno-Core.

Platforms	Elevation range (m a.s.l.)	Mean elevation (m a.s.l.)	Area covered	Main features
P1	29 - 31	30	~ 590 m ²	Highest platform. Discontinuous and poorly preserved in extension. Uncertain wave-cut origin.
P2	24 - 28	26	~ 1500 m ²	Discontinuous surface. Uncertain exclusive wave-cut origin. Pegmatitic vein mentioned before comprises part of the surface.
P3	22 - 24	23	~ 184 m ²	Poorly preserved at the end of the peninsula. Subtle display around middle hillock. Uncertain wave-cut origin.
P4	17 - 21	19	~ 0.053 km ²	Most continuous distinguishable surface. Covered by eolian deposit and medium-coarsed <i>in situ</i> weathered tonalite, shell fragments, soil and vegetation.
P5	4 - 11	7	~ 0.087 km ²	Most extensive level surrounding main platform P4 and well preserved at seaward end of the peninsula.
P6	1 - 5	4	~ 0.014 km ²	Comprises continuous platform at the end of the peninsula. NW dikes appear notoriously on it. Contains several isolated eroded rock blocks.
P7	Underwater		Unknown	Currently covered by tides. Clearly visible at the end of the peninsula. Extension unknown. Expected to emerge eventually.

Table 6. Elevation range and mean elevation per platform (in meters above sea-level), area covered and main features for each platform are summarized here. Elevation was obtained from DEMs.

Right below P1 at the end, P2 (pink polygons) extends for about 1500 m² and it is better preserved at the NE area of the platform sequence. It also appears within P1 hillock previously mentioned. From the SE of the blocky platform-tower an apparent continuation of P2 in a SW direction can be seen (Figure 32). Although it certainly looks regular and correlatable to the rest of P2, it is better associated to a SW-plunging joint set that defines weak planes throughout the peninsula -along with 2 subvertical sets striking NW and NE- eventually developing block-shaped erosive patterns (Figure 33). Around all this area of the peninsula, actual fallen blocks from upper levels can be spotted lying in lower levels, as a result of these structural and erosive conditions.

The third level, P3 (orange polygons), is poorly preserved covering a ~180 m² area at the end of the peninsula, particularly, at the “tower’s” NE face (Figure 28).



*Figure 29. Images shows platform P7 covered by waves in a low tide. Dark seaweed can be observed attached to the surface of the platform. Field photo by the author.
Photo-shot location and orientation shown in Annex 2.*

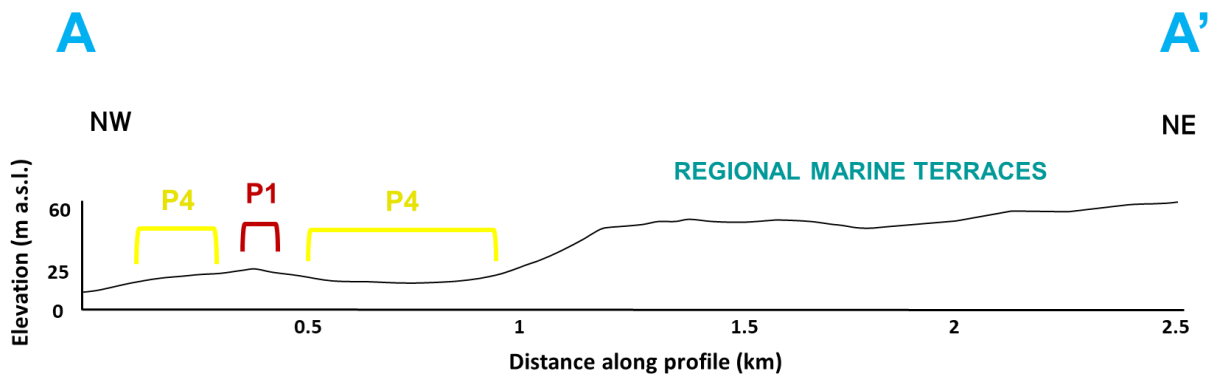
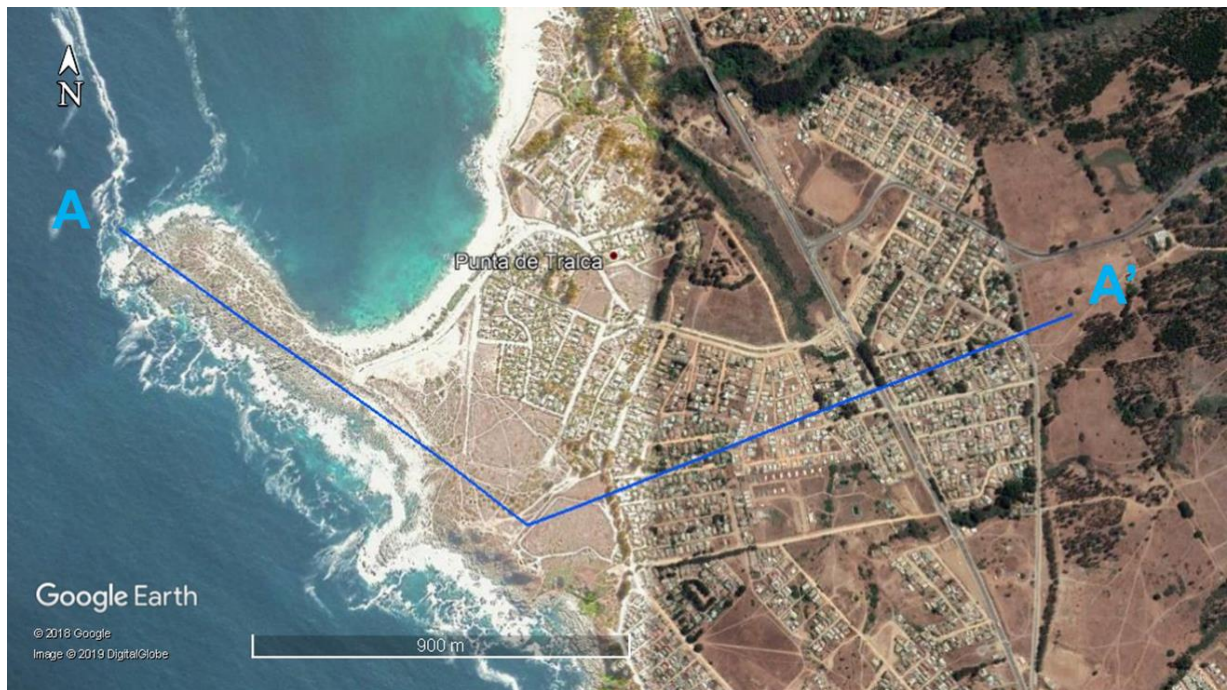


Figure 30. Topographic profile A-A' obtained from Google Earth software. Up: profile trace A-A'. Down: simplified interpretation of the topography with relatively low resolution. Platforms P2, P3, P5, P6 and P7, cannot be distinguished at this scale and resolution.

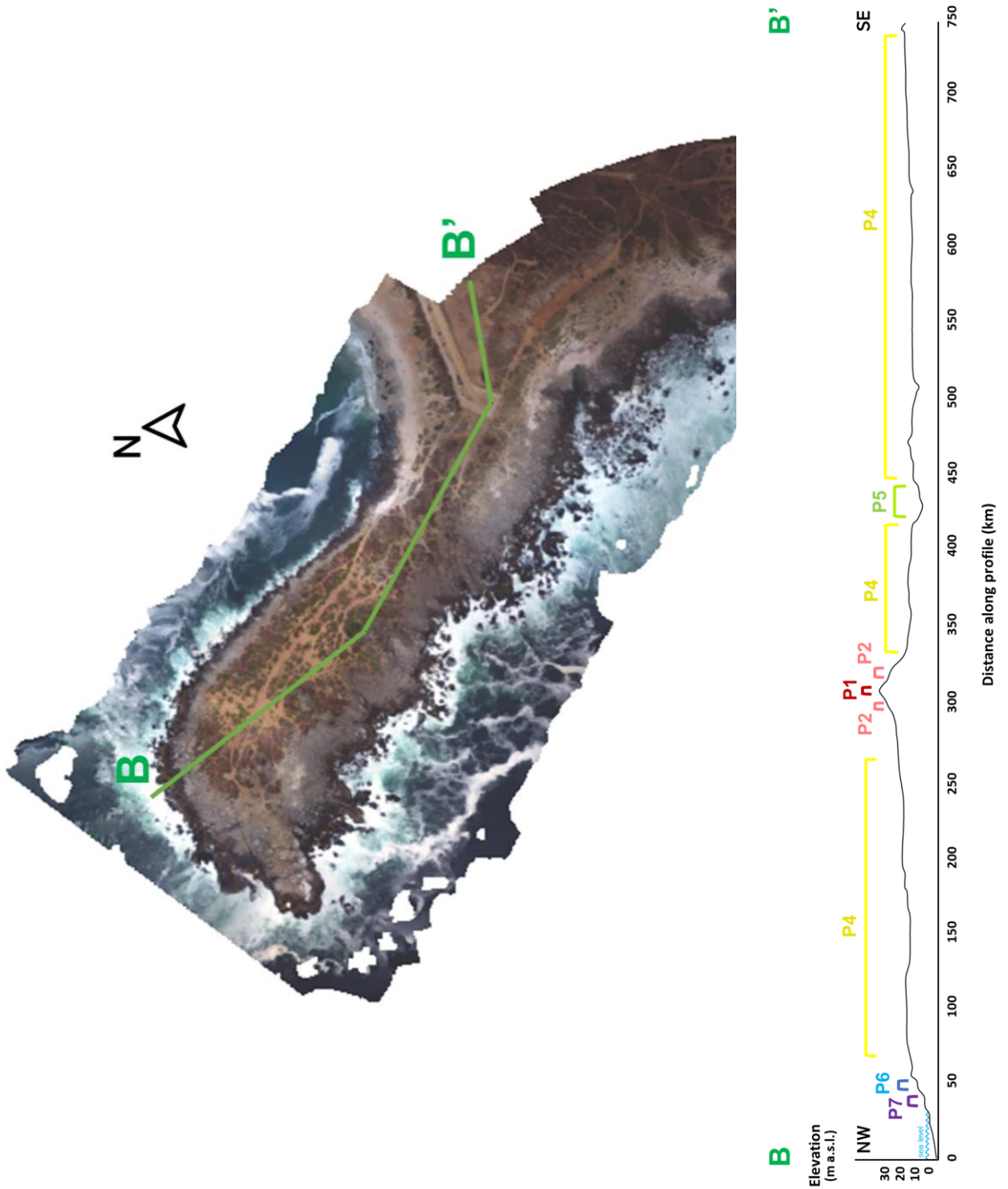


Figure 31. Topographic profile B-B' obtained from DEM developed with drone DJI Phantom 4. Up: profile trace B-B'. Down: interpretation of the topographic profile where P1, P2, P4, P5, P6 and P7, stand for the mapped and described platforms with their respective color index.

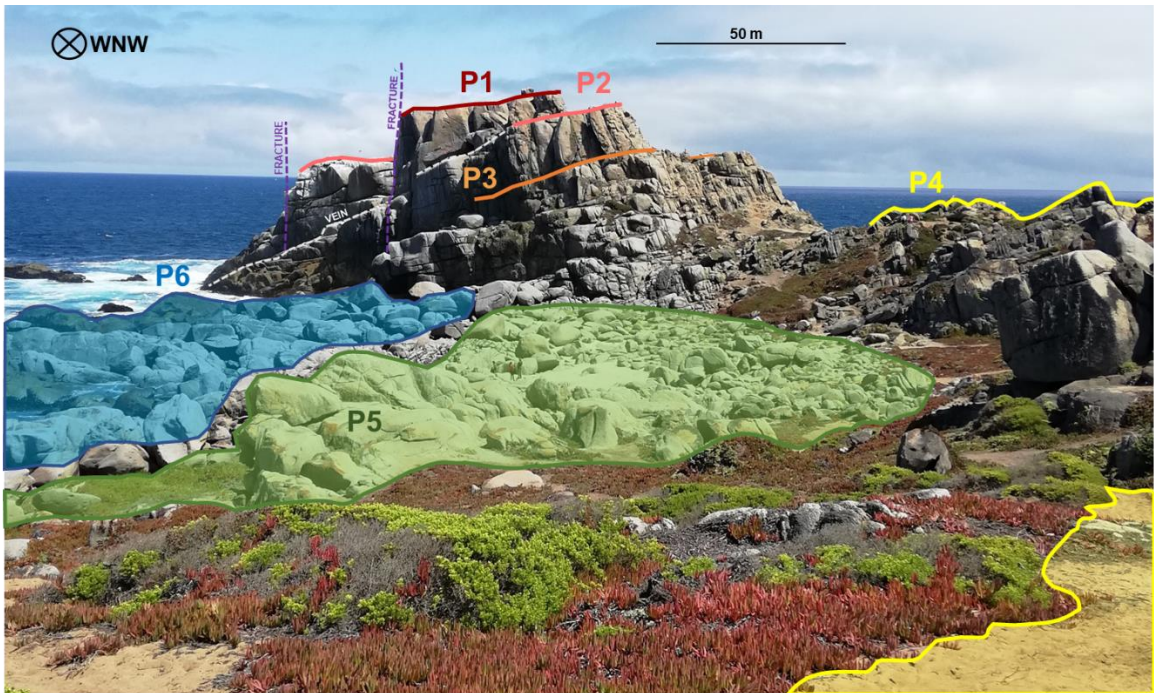


Figure 32. Up: unedited field photo by the author. Down: interpreted image of the seaward end of the peninsula showing platforms 1, 2, 3 and 4 with a WNW view. White dashed line indicates the exposed surface of a notorious quartz-plagioclase-biotite vein emplaced along a fracture. Purple dashed lines show fault planes (the one with a question mark is a fracture in which no apparent setoff could be seen). Photo-shot location and orientation shown in Annex 2.



Figure 33. Photo taken from P6 showing a SSE view of the blocky pattern mentioned in the text. Field photo by author. Photo-shot location and orientation shown in Annex 2.

Yellow polygons correspond to P4 which is the platform that comprises great part of the peninsula covering an area of 0.053 km² (Figure 27). Medium to coarse grained particles generated from *in situ* weathering and erosion of the tonalite, as well as eolian deposits (fine sand), form extense deposits along the peninsula where ground-level vegetation has grown. Shell fragments can also be found among the sand, but only within a centimeter-deep layer overlying soil development. As there are also several unbroken shells, it is believed that human action along with biological activity from bird species in the area, have strongly contributed to their deposit. Nonetheless, geological sources are not discarded: former littoral dynamics or tsunami action could have contributed as well.

Platform 5, P5 (green polygons), covers most of the peninsula -approximately 0.087 km²- but mainly surrounding the most continuous level, P4 (Figure 27). At the far end of the peninsula, P5 is displayed as a mostly even and continuous surface (where the NW dikes

of ETDS can be seen notoriously), except for an apparent vertical setoff along the NE dike of ETDS which is indicated with white arrows in Figure 34, Figure 38, Figure 36, and Figure 37. It appears to have been displaced about 2 meters along the NE ETDS strike, and along a wide fracture cutting the seaward block-tower of the peninsula in a NNW direction (Figure 34). However, no consistent field evidence regarding a fault plane along NE ETDS was found, and drone images from suitable perspectives have shown that the mentioned wide fracture shows no setoff of a distinct vein older than the current erosional forms.

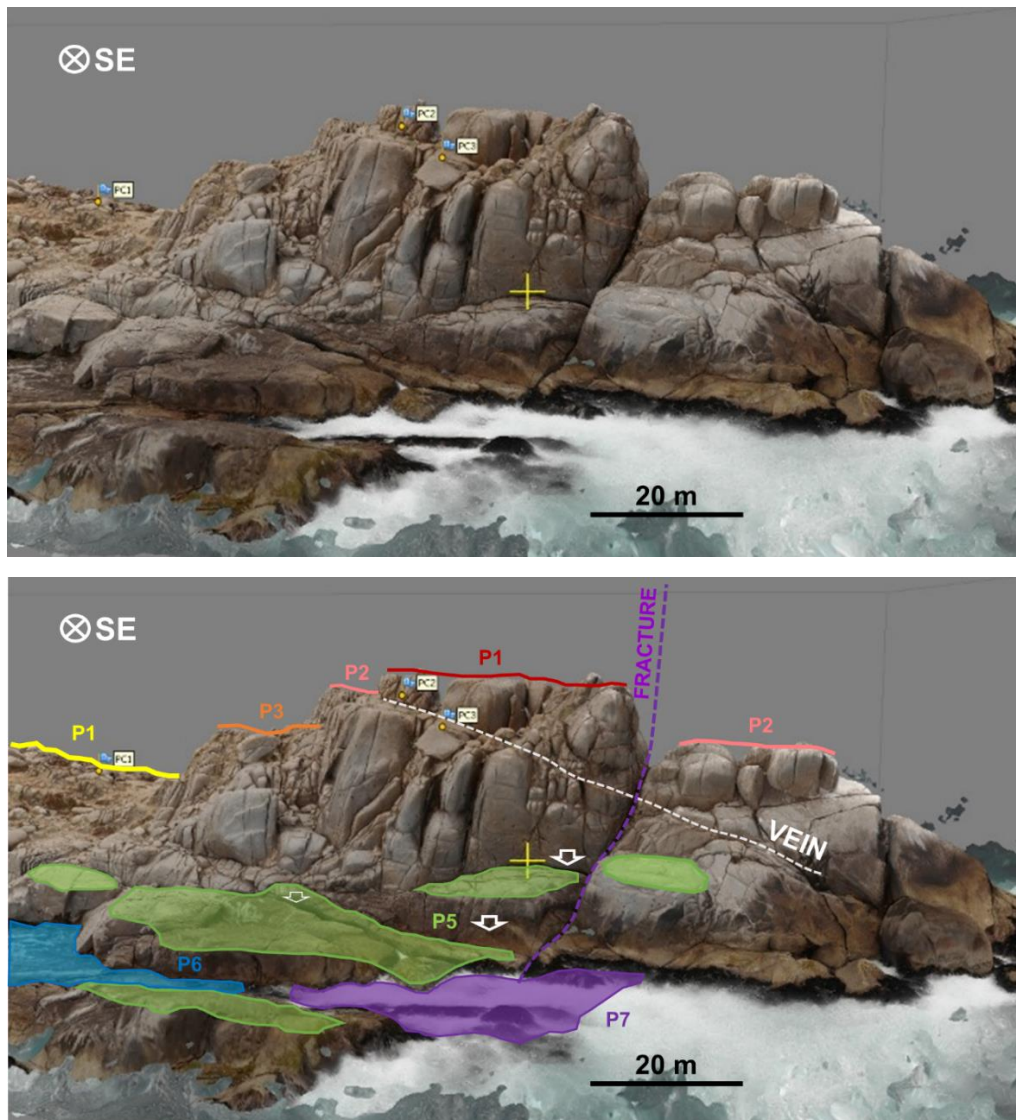


Figure 34. SE view of the 3D drone model corresponding to the seaward end of the peninsula. Up: unedited image. Down: interpreted image. Distinct vein shows no setoff.

White arrows show apparent setoff within platform P5. Photoshoot location shown in Annex 2.

Platform 5 also contains several eroded blocks in the SE side of the peninsula, that could have fallen from eroded upper levels in the past; they could also have been tilted or turned around by wave action within the same platform. Tsunami triggered flip or movement of huge blocks in other places, has been observed and documented before (Goff et al. (2006); Goff et al. (2010)).

The lowest emerged level, platform P6 (blue polygons), covers a ~ 0.014 km² area and is currently the most affected by wave action and tides (Figure 27, Figure 28). P6 at the NW extreme of the peninsula appears darker in color because of constant wetting by waves. Ponds of sea water with growing sea weeds and moss are also found at this level. Additionally, the NW dike swarm outcrops very clearly here (Figure 35). This platform, as well as P5, contains several of the mentioned eroded blocks (Figure 40).

Platform 7, P7 (purple polygons), is mapped only where it is clearly visible between waves at the seaward-most area of the entire peninsula (Figure 28). It is also distinguishable because of the dark seaweed attached to it, partially emerging over-tide (Figure 29). Rough estimates locate P7 around 1 m under the mean tide level. Extension of this platform is unknown since it is still underwater. It is, although, expected to emerge eventually due to long- and short-term tectonic activity, as have allegedly all the other levels.

Although the different platforms that comprise Punta de Tralca Peninsula resemble wave-cut platforms, it is important to note how these interesting topographic features are strongly related to the presence of 3 main joint sets: NW subvertical set, NE subvertical set and subhorizontal to SW-plunging set described in the following section. From different perspectives, some of platforms seem to be highly inclined towards the SW (Figure 32).

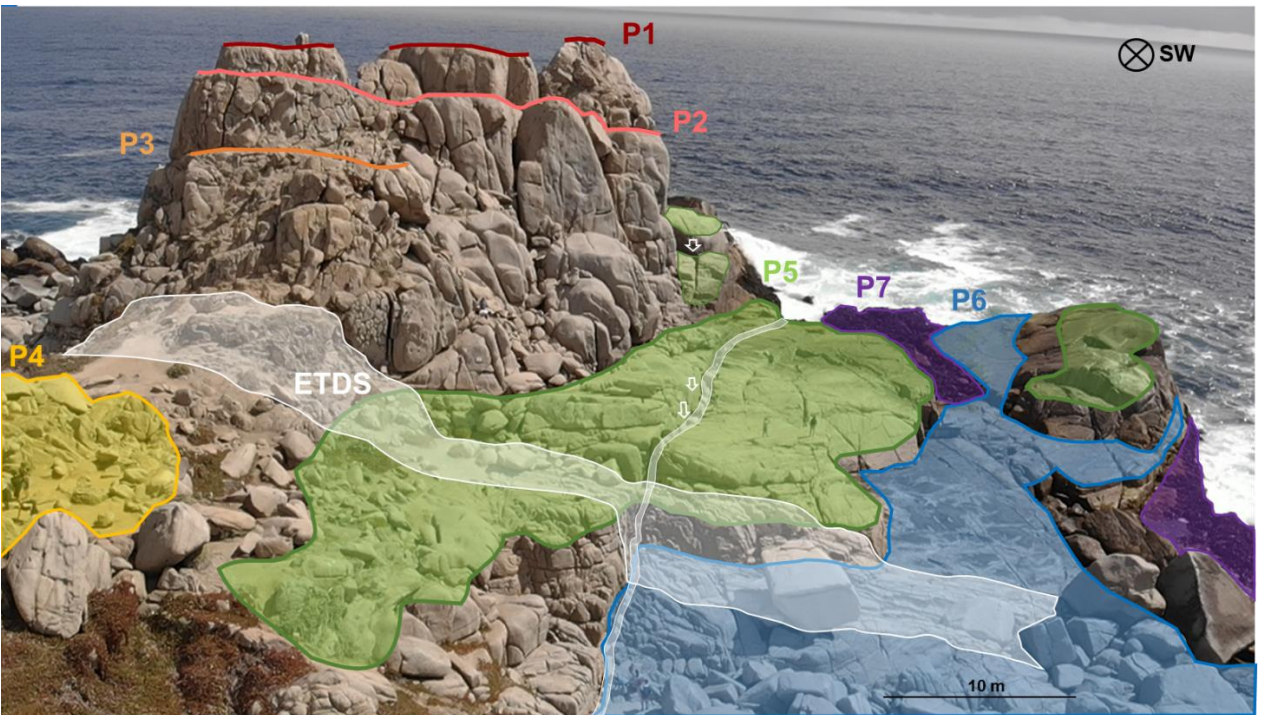


Figure 35. SW view of the peninsula. Up: unedited field photo taken with DJI Mavic Air drone; flight by Nicolás Bueno-Core. Down: edited image showing platform levels in different colors. P1 is the highest recognized platform level, whereas P6 is the lowest emerged. P7 is underwater and seen between waves. White polygons in NW and NE-

strike correspond to El Tabo Mafic Dike Swarm (ETDS). White arrows indicate apparent setoff (see

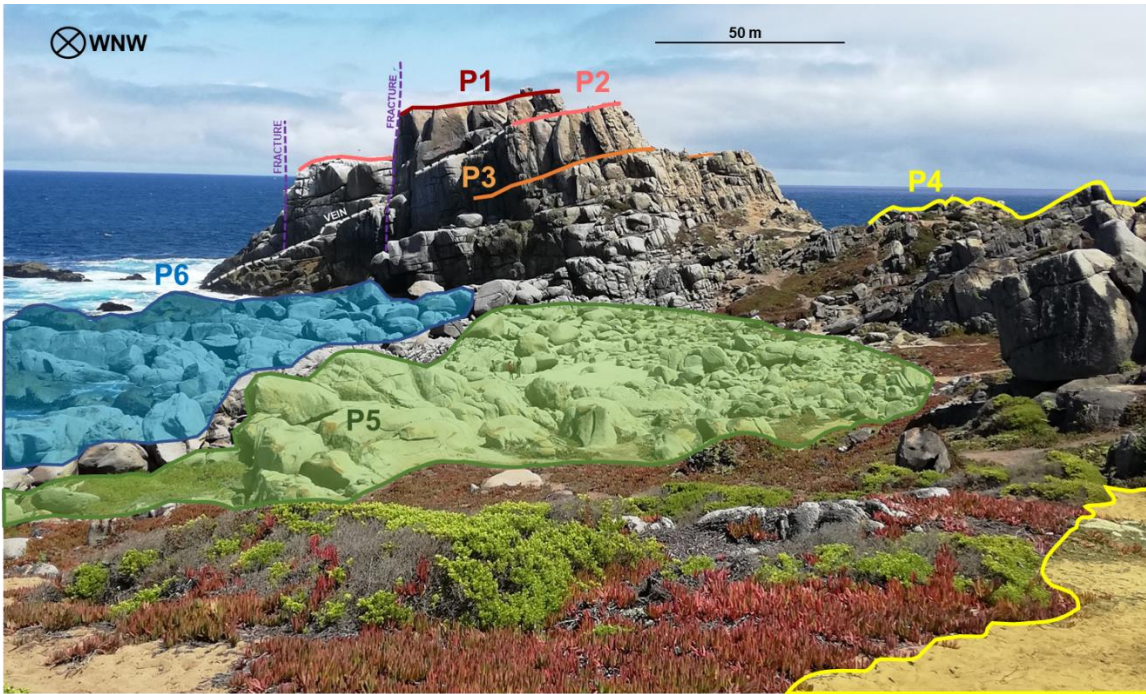


Figure 32 and Figure 36). Photo-shot location and orientation shown in Annex 2.



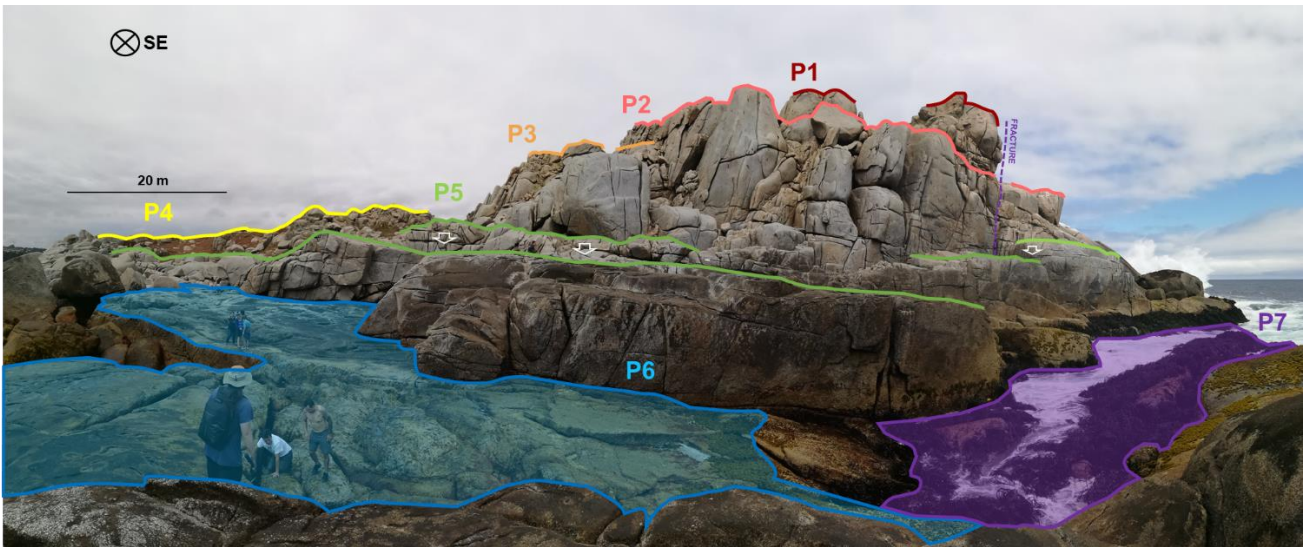


Figure 36. SE view of the peninsula showing platforms from P1 to P7. Up: unedited field photo by author. Down: interpreted image with mapped platforms, scale and orientation. Purple dashed line shows recognized subvertical fault trace. White arrows show apparent setoff (see text for discussed interpretation). Photo-shot location and orientation shown in Annex 2.



Figure 37. SW view of the peninsula showing apparent displacement of P5 (white arrow) along the NE dike strike of ETDS. Field photo by author. Photo location and orientation shown in Annex 2.

3.2 FRACTURES AND FAULTS

One of the first order observations about the peninsula is the presence of 3 main joint sets: NW subvertical set, NE subvertical set and subhorizontal to inclined set, in which SW-plunging joints prevail and occasional NE-plunging fractures and veins appear (Figure 38 and Figure 39). These 3 main sets determine intense blocking around this area. Widespread fallen isolated blocks with well-developed tafoni -compared to the actual platform they are at- can be associated to higher levels being constantly weathered and eroded. In P6 several fallen blocks (due to this blocky-pattern erosion) with different tafone-development degree are found (Figure 40).





Figure 38. SW view of the seaward end of the peninsula. Up: unedited field photo taken with DJI Mavic Air drone; flight by Nicolás Bueno-Core. Down: interpreted image showing the El Tabo Dike Swarm (ETDS), both NW and NE-striking components. Photo-shot location and orientation shown in Annex 2.





Figure 39. Panoramic southward view of P4 scarp (with inherent panoramic-effect distortion). Up: unedited panoramic field photo by author. Down: interpreted image showing an example of a NE-dipping fracture and vein (white dashed line). NW and NE ETDS are also shown. NE ETDS visible outcrop is indicated with a solid turquoise line, while the dashed line indicates its covered by in situ-formed sand. Photo-shot location and orientation shown in Annex 2.

NW and NE joint-sets can be distinguished in the slope map (Figure 26) and were mapped in detail as shown in Figure 41. They appear more densely distributed close to NW and NE dike swarms (Figure 38, Figure 41), respectively. These joints have been interpreted as self-generated fractures related to shallow dike emplacement during Early-Cretaceous (Creixell et al. (2011)).



Figure 40. Images showing fallen boulders at platform P6 removed from their original location due to a blocky-pattern erosion triggered by the existing joint sets. Field photos by author. Photo-shot location and orientation shown in Annex 2.

Regarding the SE face of the area, it is relevant to note how P2 appears to be a very homogeneous and inclined surface. Nonetheless, imagery and fieldtrip observations helped conclude that part of this level (mapped with a white dashed line in Figure 32) may not be part of the original P2 developing surface and could just correspond to a discontinuity-originated level, since a SW-plunging joint set affects the whole peninsula. A key observation that supports this idea, is the presence of a very distinguishable 30 cm thick quartz-plagioclase-biotite vein (Figure 42) that comprises the surface of this apparent level. Furthermore, inclinations of both surfaces differ: P2 dips 10° to the SW, whereas the vein dips $20-25^\circ$ to the SW.

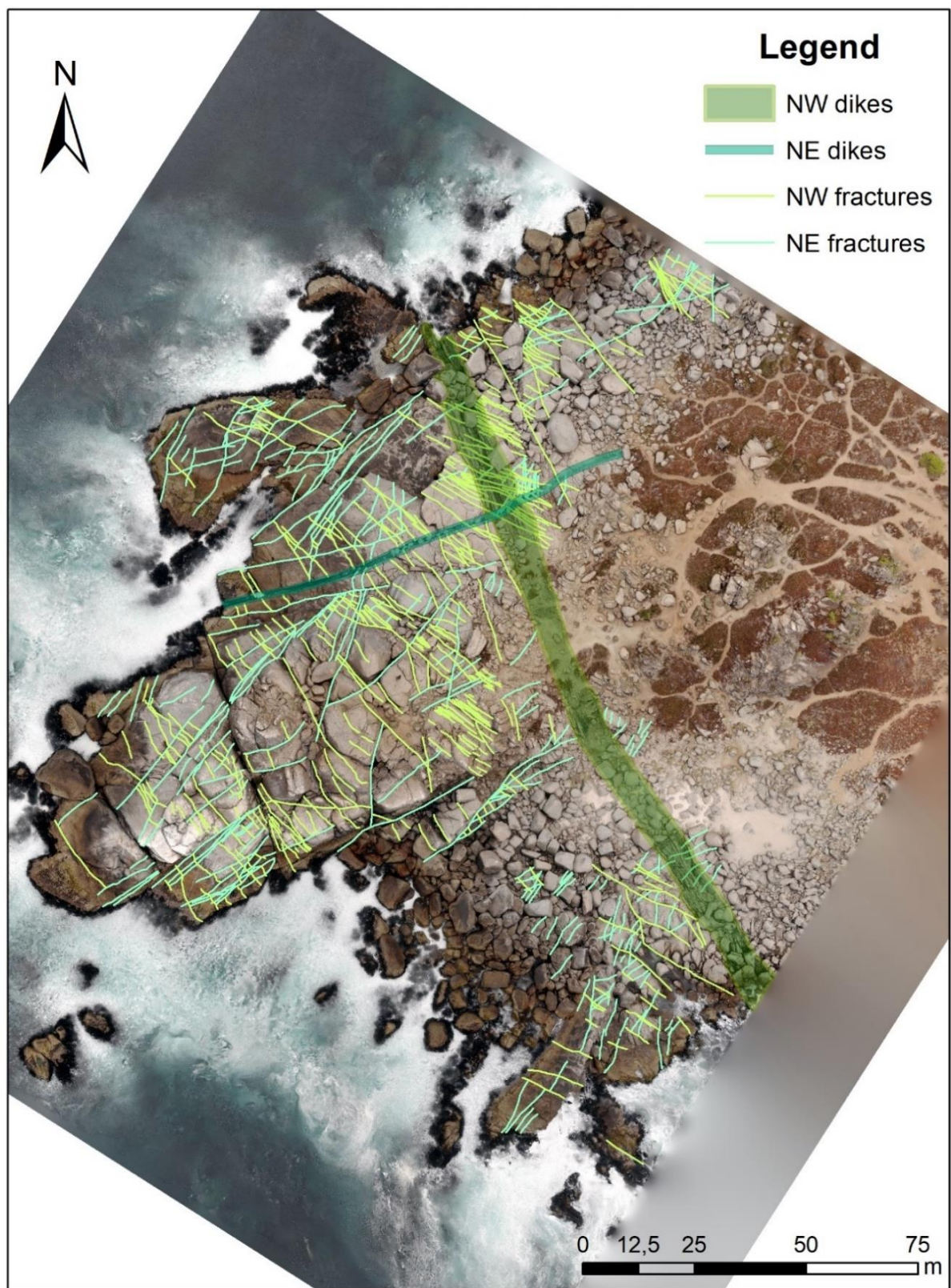


Figure 41. Map showing NW and NE dike swarms, and NW and NE minor fractures.
Photo obtained with DJI Mavic Air drone; flight by Nicolás Buono-Core.

It is also likely that some blocks that comprised P2 (over the mentioned vein level and from the SE perspective) were lost, resulting in this apparent smooth and inclined surface. This premise can be applied to every level in this peninsula, and it is one of the main reasons for not defining upper platforms as undoubted wave-cut platforms or marine terraces.



Figure 42. Quartz-plagioclase-biotite vein. Left: SE view of vein at P2's surface. Right: vein mineralogy close-up. Field photo by author. Photo-shot location and orientation shown in Annex 2.

Regarding the search for faulting in the area, there are two main structures cutting the platform outcrop that, at first sight, look as faults. They are shown in Figure 32. One of them appears to be displacing P5 along a subvertical to NE-dipping plane. Nonetheless, it is shown in Figure 34 how this structure is not displacing the characteristic mentioned vein (Figure 42). Consequently, this structure should be considered as a fracture.

The second structure, immediately SW of the latter, is noticeable because it has widened leaving a gap between the adjacent blocks. Nevertheless, it does not show a clear relative displacement between the involved blocks. Consequently, it is also considered a fracture.

In addition to the mentioned major fractures in the area, a third structure could be considered in the description, since the vertical plane through which the NE-striking dike outcropping at P5 and P6 was emplaced, tentatively marks off some setoff for the surface mapped as platform P5 (Figure 35, Figure 36, and Figure 37). If this was the case, the block to the NW of the NE ETDS would comprise a hanging wall, the block to the SE a foot wall, and structure would correspond to a normal fault.

Within the NE-striking dike, a couple of structures resembling sigma-type kinematic indicators were found (Figure 43), specifically where it crosscuts the NW ETDS (Figure 45). Along these, a fine-grain non-cohesive material is observed. This material resembles intensely weathered minerals and/or fault gouge. These indicators could also be related to the emplacement dynamics of the swarm comprising, for example, dilational jogs. The development of this hypothesis is out of the scope of this work.

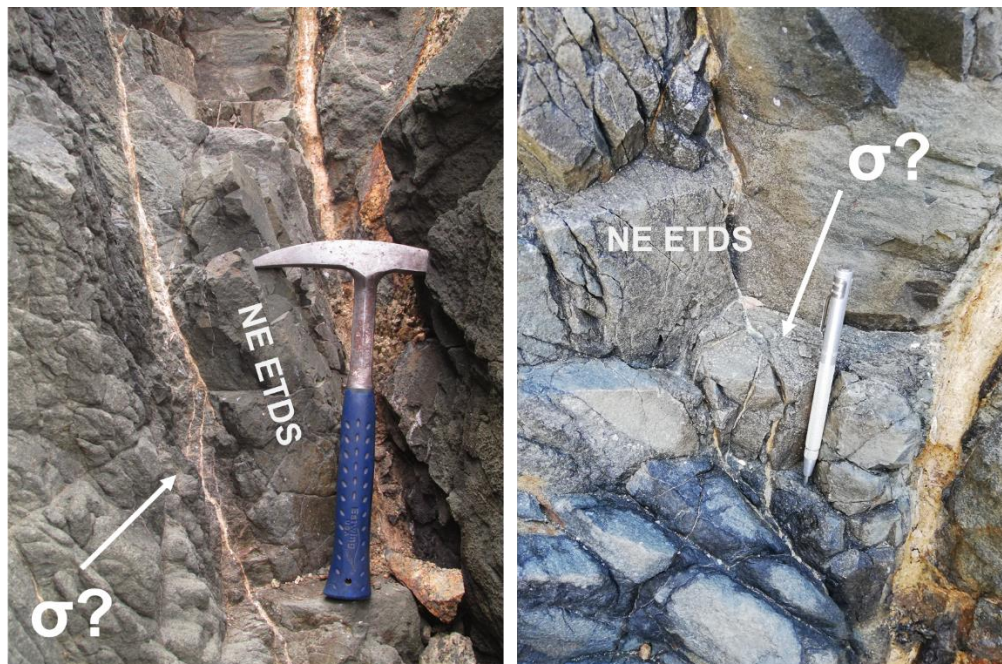


Figure 43. Sigma-type-resembling structures observed in NE ETDS, specifically where NW and NE ETDS crosscut at platform P6. Origin and classification are unclear. View of

the NE dike is oriented towards the SW. Along these structures and parallel to them, fractures with weathered fine-grain non-cohesive material are seen. Field photos by author.

3.3 DIKES AND ENCLAVES

As stated before by other authors, the presence of enclaves and dikes is part of the main features described around Punta de Tralca Peninsula. El Tabo Mafic Dike Swarm (ETDS) has already been described and mapped in previous sections of this work (Figure 41). Literature data such as location, orientation and main characteristics for dikes and enclaves, was checked during field work.

This dike swarm is comprised by a NW-striking swarm showing sinistral kinematic indicators and a NE-striking one which, in this peninsula, is represented by an 80 cm-thick dike (Figure 44). Both are crosscutting each other, as shown in Figure 45.

Dike orientation and continuity were also corroborated in the field and most of the NW dikes show a sinistral kinematic indicator (Figure 44). Also, when NW and NE dikes crosscut each other, some structures were found as shown in Figure 43 in the previous section, although their origin remains unclear.

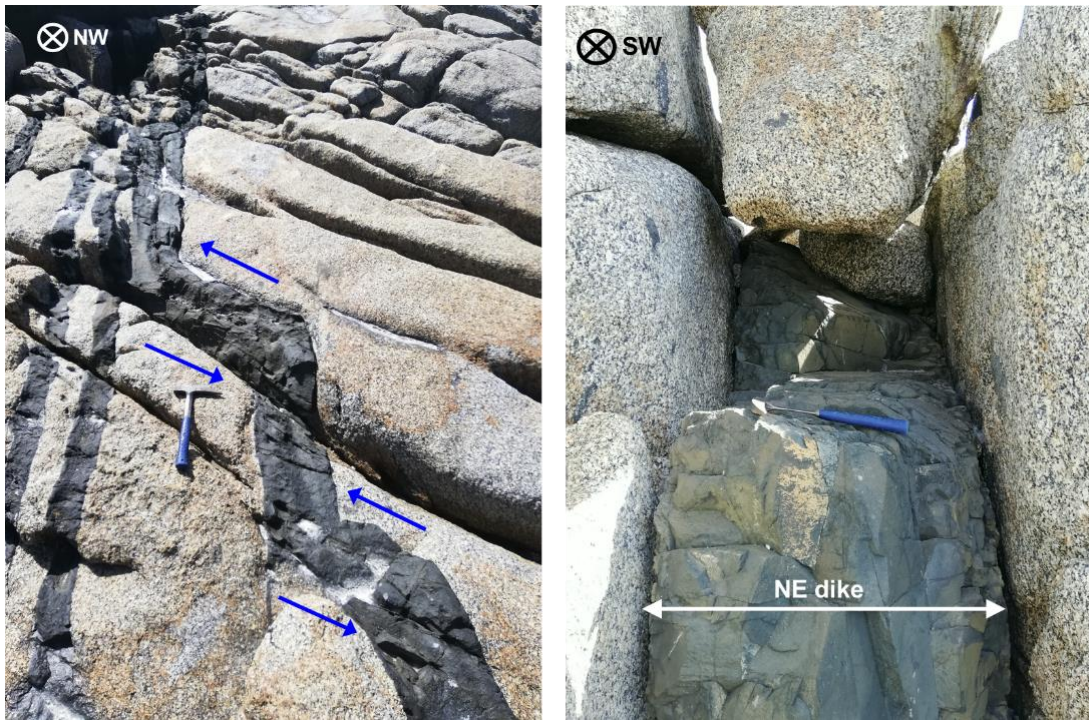


Figure 44. Left: NW dike swarm showing sinistral displacement at P6. Right: NE dike outcrop at P5. Field photos by author.

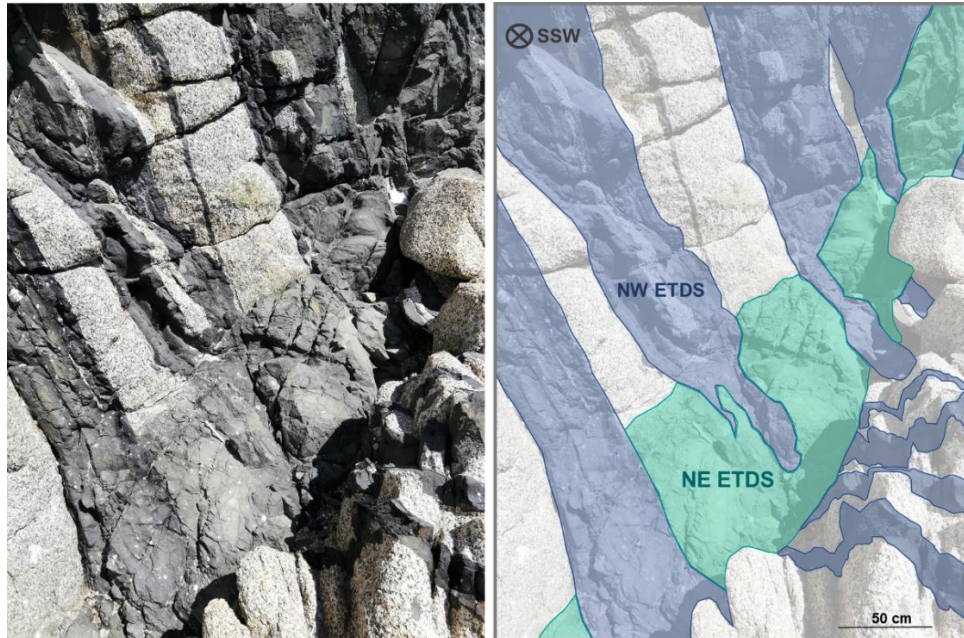


Figure 45. NW and NE-striking dikes from El Tabo Mafic Dike Swarms (ETDS). Left: original image obtained in the field. Right: sketch showing crosscutting relation. Field photo by author.

Moreover, mafic medium grain enclaves appear in every country rock outcrop, with a preferential NW orientation. With elongated shapes and sizes ranging between a few cm and up to 70 cm in their long axis, they are homogeneously distributed throughout the study area. Many of the enclaves -and specially those at seaward end tip of the peninsula- are differentially eroded in relation to the felsic country rock, since their mineralogy is less resistant to weathering than the latter (Figure 46). These mafic enclaves have been studied before by different authors and are one of the main distinguishable features of great part of the Santo Domingo Complex described in the previous geological setting section.



Figure 46. Mafic elongated oriented enclaves of variable sizes. Left: 70-cm enclave with ellipsoidal basal section. Right: NW-oriented enclaves that have been differentially eroded. Elongation axis in both images goes towards the southeast. Field photos by author.

3.4 TAFONI CLASSIFICATION AND DISTRIBUTION

As stated beforehand, the analysis of tafoni is expected to provide some first-approach insights regarding surface exposure ages for the study area. Therefore, they were measured and analyzed.

Tafoni can be seen almost all around the peninsula's seaward-most area, where sea spray salts favor their development (Figure 47). With a vast variety of shapes and sizes, tafoni in this area usually develop responding to previous fracturing (basal tafoni according to Goudie (2003)) and to mafic enclave presence. It is only in the upper four platforms, that regular-tafoni (side-wall type proposed by Goudie (2003)) growth can be spotted.

To facilitate this analysis throughout this work, tafoni were classified into 3 categories according to origin and into 3 categories according development degree (Table 7). Origin categories are: (1) enclave tafoni (Figure 48, Figure 50), (2) joint tafoni (Figure 49, Figure 50), and (3) regular tafoni (Figure 51). Additionally, topographic profiles of the area showing platform distribution and presence of tafoni according to development degree (Type I, II and III on Table 7) are shown below in Figure 56.

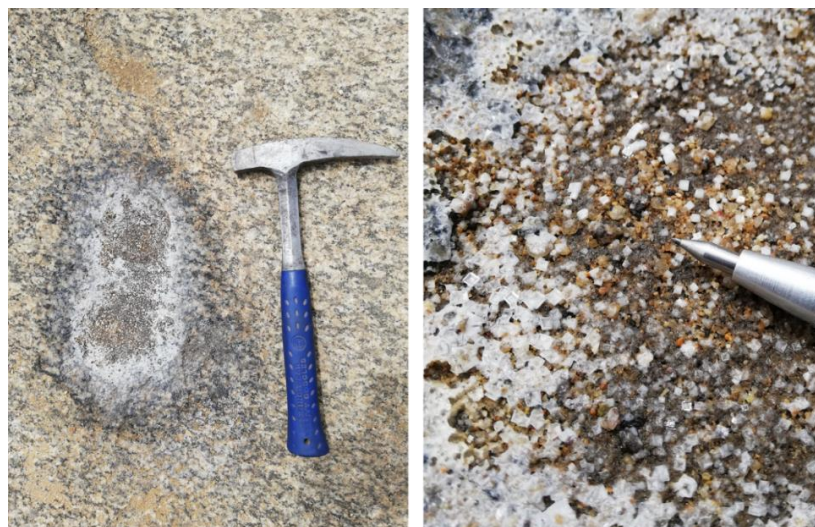


Figure 47. Images showing presence of salt crystals from sea spray in enclaves (Left), favoring weathering processes. Right: hopper crystals close-up. Field photos by author.



Figure 48. Enclave tafoni (Type III) of about 20 cm in long axis. Tafone at the right, shows additional erosion spots within. Field photos by author.

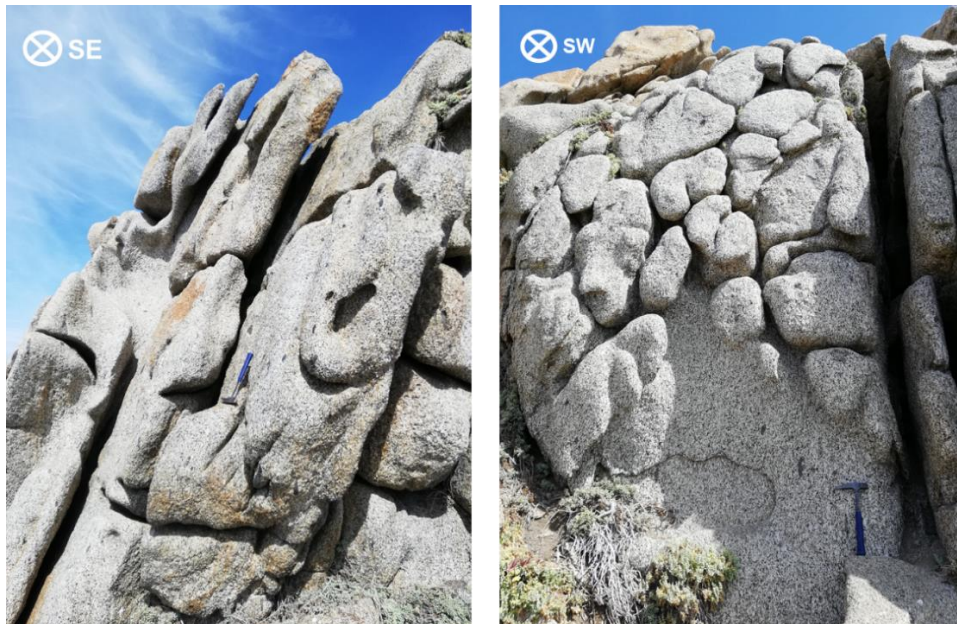


Figure 49. Left: Type II Joint tafoni at P2 scarp. Right: Type III Joint tafoni at wall located close to intersection of ETDS (see Figure 38). Some joint-defined blocks have already been removed by erosion. 33 cm geological hammer for scale. Field photos by author.



Figure 50. Image shows some joint tafoni (Type II) and enclave tafoni at the surface of P2 and scarp of P1 platforms. Field photo by author. Photo-shot location and orientation shown in Annex 2.

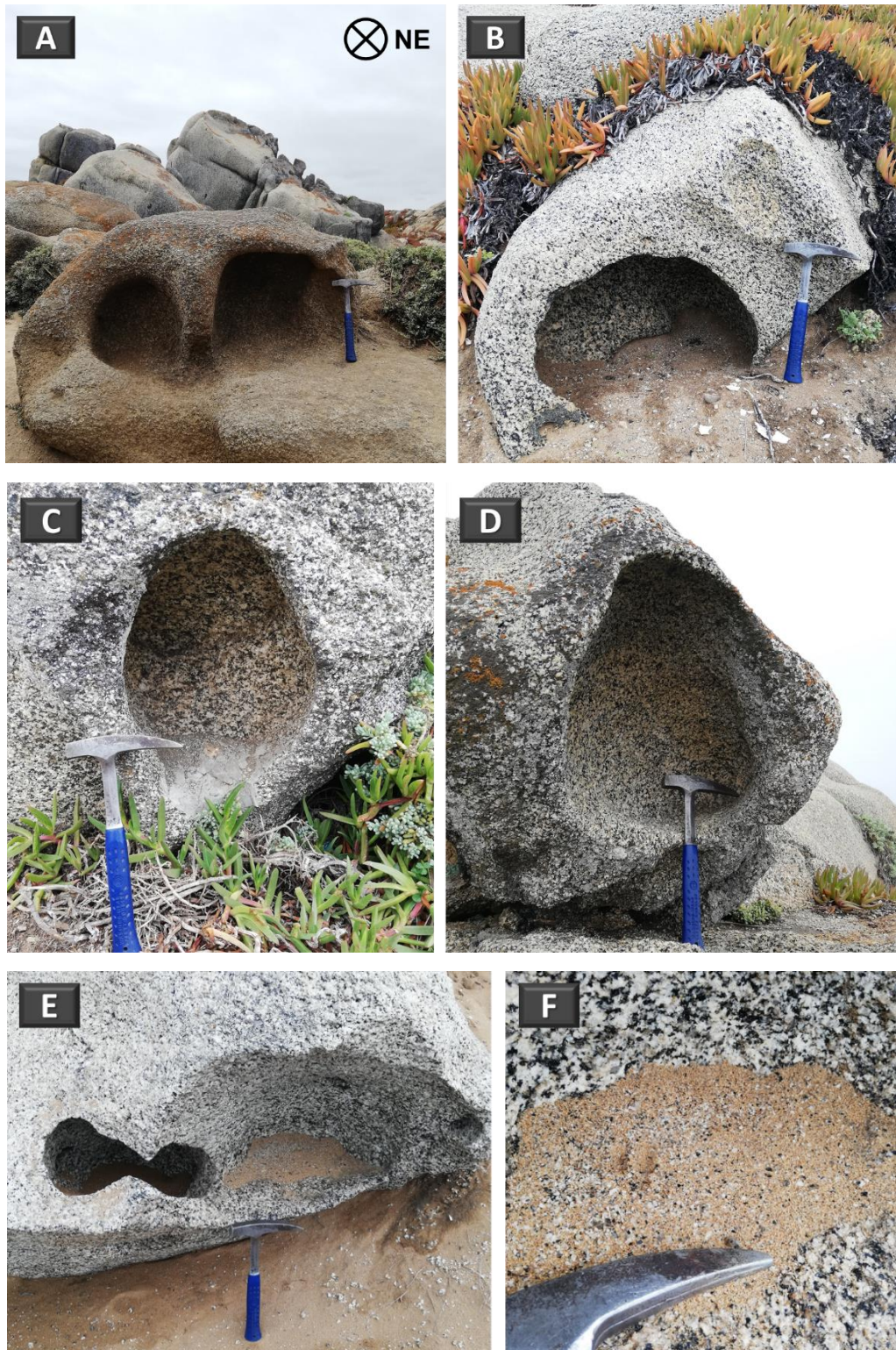


Figure 51. Regular tafoni found at platform P4. Photos A-E show Type I tafoni. Photos E and F show disaggregated tonalite minerals (mixed with sand from P4 deposit) inside the tafone indicating that it is still active. Field photos by the author.

TAFONI DEVELOPMENT SCALE





TYPE	REFERENCE IMAGE		GENERAL CHARACTERISTICS
 INCREASING DEVELOPMENT	I		<p>Tafoni present well-developed cavities (cavernous-type weathering) with regular shapes (A). On the other hand, relicts of former tafoni that have been weathered in very irregular shapes can be distinguished (B).</p>
	II		<p>Of cavernous-type forms, but without reaching significant development (up to 20 cm deep). Also, they can display shapes that have been conditioned by previous existence of crosscut and/or parallel joints. Joint width can vary between 20 - 100 cm.</p>
	III		<p>No important cavernous forms are distinguished. Only cavities with depths of a few cm (< 20 cm). Furthermore, joint-tafoni width reaches up to 20 cm.</p>

Table 7. Tafoni development scale proposed in this work and applicable to the study area. Images correspond to tafoni found at Punta de Tralca Peninsula, specifically. Field photos by author.

Enclave tafoni (basal tafoni considering enclaves as discontinuities in the rock) occur due to differential erosion between tonalite country rock and mafic enclaves, the latter having less resistance to chemical erosion in terms of mineralogy (Figure 48). Also, the interface comprised by enclave borders and country rock determines a weakness plane where erosion can act favorably. As explained beforehand, tafoni development is strongly related to the presence of salts from sea spray among other sources and, in fact, cubic salt-crystals can be found in most tafoni (specially in tafoni developed in surfaces rather than

scarps) as shown in Figure 47. The intense wave action and strong winds in the area help the occurrence of this process. Also, the grain size between these two lithologies is relevant when analyzing erosion rates for each rock: enclaves have fine to medium grain size, whereas the tonalite is medium to coarse grained. Therefore, enclave tafoni appear in almost every enclave at upper platforms (Figure 50) -surface and scarp- in P1, P2 and P3 (mainly surface; scarp shows less development in general, except at P1 scarp). They are undoubtedly less developed in terms of quantity and depth at P5 and P6.

Despite enclave tafoni being less developed than joint tafoni, at P1 for instance, this type of tafoni is abundant. Around 150 enclave tafoni were distinguished in the north face of P1's scarp, although not every one of them could be directly measured (most of them where located at unreachable heights). A representative amount of enclave tafoni was measured instead (Table 8). The south face of the staircase-like area is mainly covered by a white layer of bird feces and some lichen (Figure 52), hindering tafoni detection. Several enclave tafoni were also measured at P2's scarp, although joint tafoni are the most remarkable in this zone (Figure 49, Left).



Figure 52. Lichen-covered surfaces at SE face of the main platform sequence outcrop. At the background of the image, the main regional platform of this coastal area can be

distinguished. Field photo by author. Photo-shot location and orientation shown in Annex 2.

Joint tafoni (basal type tafoni) are the ones that develop in response to preexistent fractures along the rock. Since there are 3 main joint sets -NW, NE and subhorizontal to inclined- affecting the whole peninsula, joint tafoni can be distinguished among every platform. They are well developed (Type I tafone according to Table 7) in the scarp between P1 and P2, in the surface of P2, P4 (Figure 53), and locally at P5 and P6 (Figure 7, Right). Erosion has progressively widened the original fractures -sometimes provoking block detachment as shown in Figure 54-, and in places where joint sets coincide, irregular tafoni shapes have been developed in response to this cross-cut fracturing (Figure 49, Figure 51). During fieldwork, 29 joint tafoni were measured in order to have a general idea of the dimensions that this type of weathering-related feature could reach (Table 8).



Figure 53. Image shows highly eroded tonalite outcrop at P4: joint tafoni development through different-striking sets shaped the outcrop, triggering considerable material loss (Type I). Field photo by author.

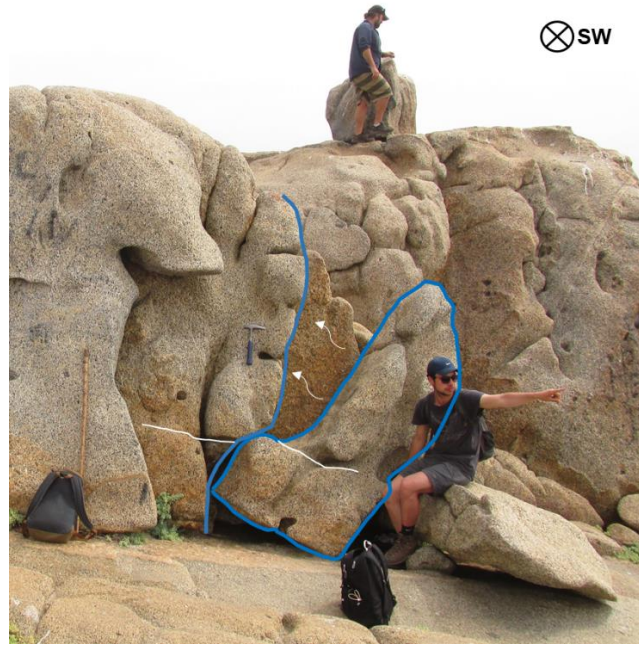


*Figure 54. Image of P1 scarp showing detachment of a block triggered by joint tafoni erosive action. White arrows indicate original position of tilted block outlined in blue.
Field photo by author.*

Regarding regular tafoni, it was found that they are the least abundant in the whole area. A number of 24 tafoni of this type could be measured (Table 8). Many tafoni seemed to be regular tafoni at first sight, but observations of the surrounding fractures and erosion were useful to help classify them properly; in this case, it is very easy to confuse joint-conditioned shapes with regular tafoni. The most representative findings for regular type tafoni or cavernous weathering, are the ones shown in Figure 51 which correspond to Type I tafoni. These were also measured and are included in Table 8.

Regarding tafoni appearance around Punta de Tralca Peninsula, 3 topographic profiles showing platform elevations and distribution of tafoni per type (based on Table 7 classification), have been developed from the Digital Elevation Model (DEM) built with the data obtained from DJI Mavic Air drone. Profile traces are shown in Figure 55 and the profiles with the tafoni-type classification (Type I, II and III) are shown in Figure 56.

	ENCLAVE TAFONI			JOINT TAFONI			REGULAR TAFONI		
	Lenght (cm)	Width (cm)	Depth (cm)	Lenght (cm)	Width (cm)	Depth (cm)	Lenght (cm)	Width (cm)	Depth (cm)
1	8	6	5	32	5	30	40	20	10
2	17	12	8	60	7	20	17	15	7
3	20	8	3	50	20	40	4	3	3
4	5	3	1	25	5	25	4	3	3
5	5	4	2	45	5	30	7	4	3
6	30	5	4	30	15	15	30	15	4
7	8	6	2	30	15	40	40	10	7
8	8	6	5	15	7	20	27	16	7
9	30	15	7	15	5	7	7	6	2
10	9	6	2	15	4	6	25	20	20
11	8	6	2	28	6	13	25	40	17
12	7	5	4	100	13	18	35	10	35
13	10	5	3	80	7	45	50	60	15
14	10	7	4	50	15	10	30	40	20
15	13	8	5	60	30	16	20	30	15
16	25	10	5	30	10	5	30	20	10
17	10	4	3	16	8	10	7	25	6
18	18	10	4	35	60	50	12	33	4
19	15	7	4	100	40	8	60	55	40
20	10	8	4	100	40	25	65	55	30
21	15	10	3	45	17	50	35	25	40
22	12	8	3	400	30	200	25	20	45
23	6	6	3	400	10	200	40	55	20
24	17	13	5	150	7	50	35	35	30
25	14	7	4	50	15	20			
26	17	12	2	150	30	70			
27	15	8	5	60	30	25			
28	15	8	3	55	20	35			
29	14	10	4	70	33	40			
30	12	8	5						
31	12	7	5						

Table 8. Tafoni measurements obtained from fieldwork by author. Colors in each cell represent the surface and/or scarp in which tafone measurement was taken (Platforms: P1-red, P2-pink, P3-orange, and P4-yellow). Lower levels have been omitted since enclave tafoni is poorly developed, joint tafoni are unilaterally well-developed in every platform, and regular tafoni are not present (only in loose boulders that probably fell from upper platforms to lower ones).

ENCLAVE TAFONI	JOINT TAFONI	REGULAR TAFONI
Maximum depth (cm)	Maximum depth (cm)	Maximum depth (cm)
8	40	10
5	200	35
5	70	20
5	40	45

Table 9. Maximum depths measured per type of tafone obtained from data presented on Table 8. Colors in each cell represent the surface and/or scarp in which tafone measurement was taken (Platforms: P1-red, P2-pink, P3-orange, and P4-yellow).

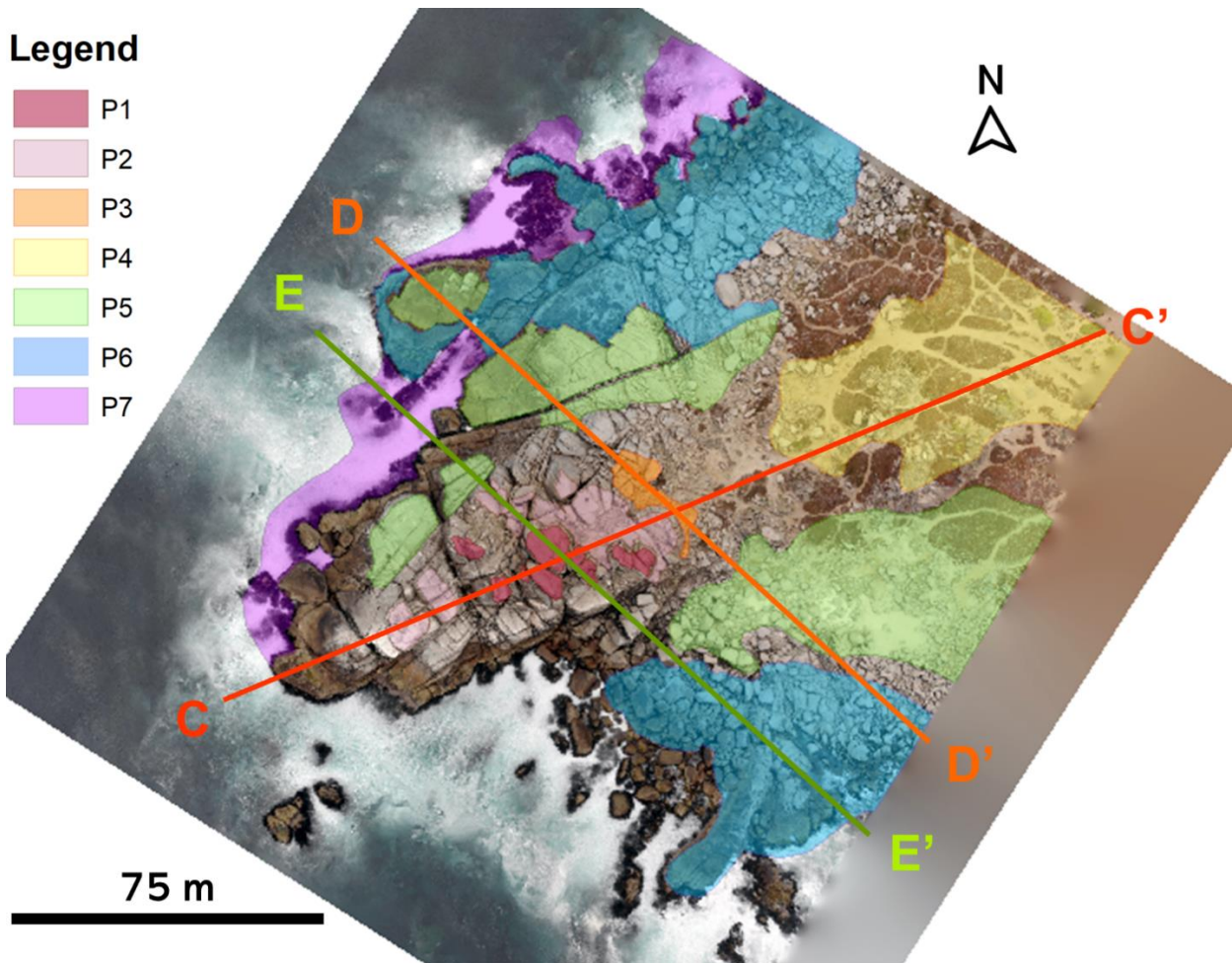


Figure 55. Map of the seaward end of Punta de Tralca peninsula, showing profile traces C-C', D-D' and E-E' interpreted below.

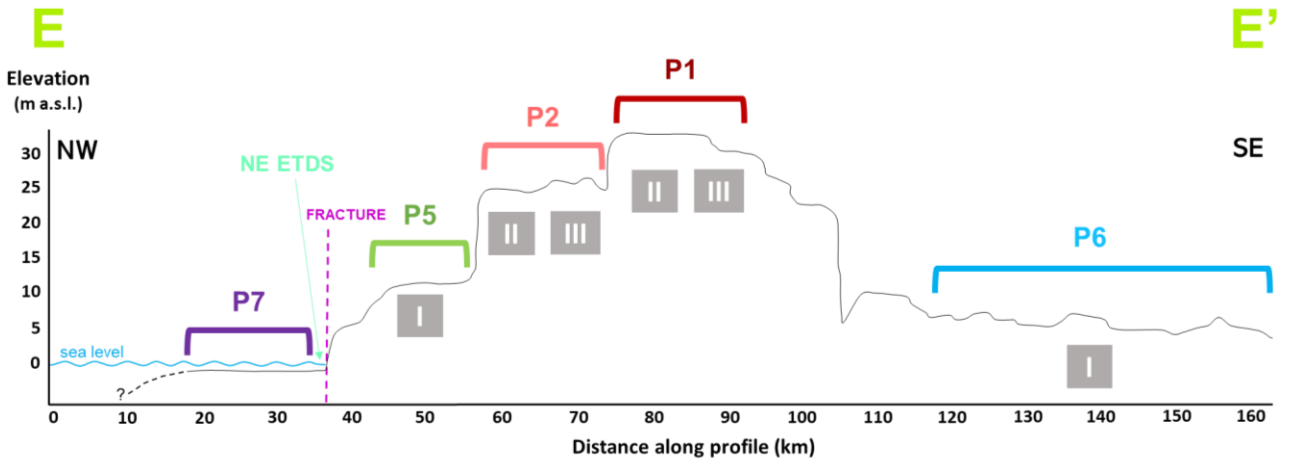
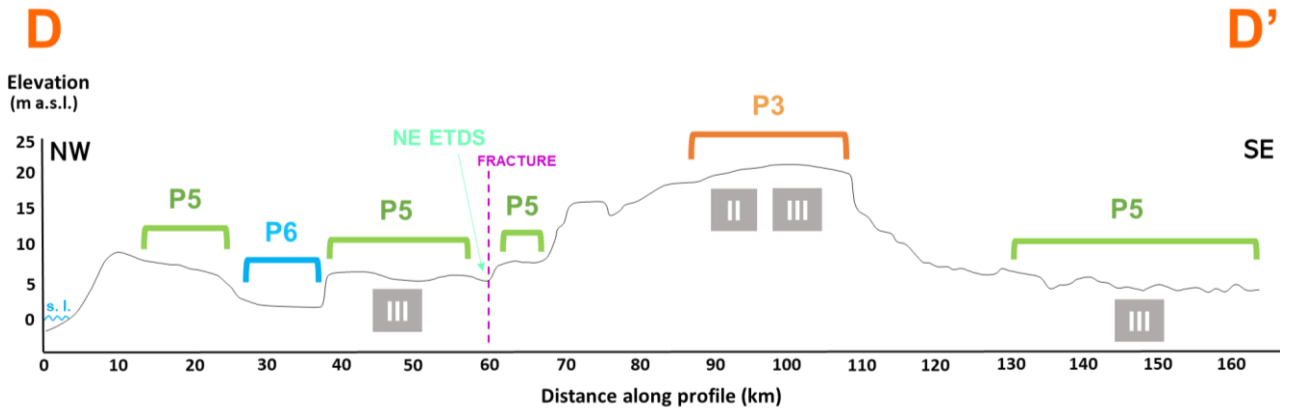
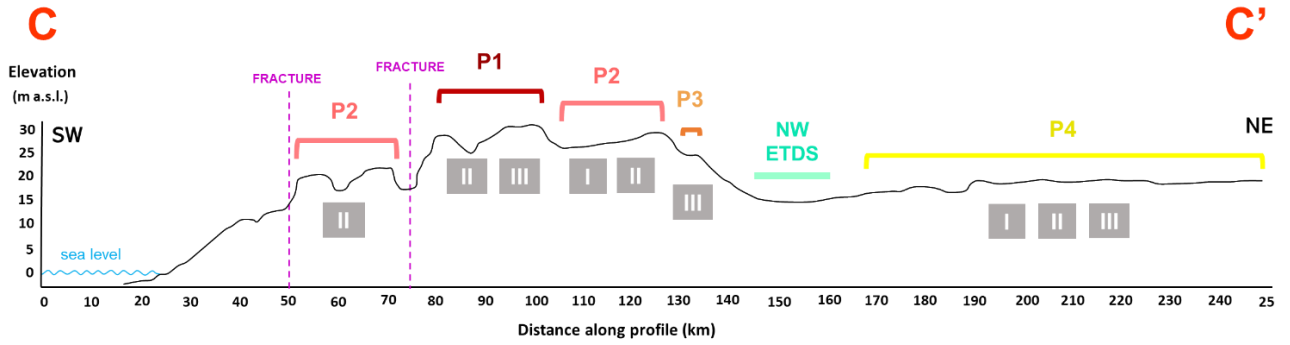


Figure 56. Topographic profiles C-C', D-D' and E-E' from traces shown in Figure 55. Platform location is shown with the respective platform label and color index shown at the beginning of this chapter. NW and NE ETDS correspond to northwest- and northeast- striking El Tabo Mafic Dike Swarms mapped in section 3.3. Major fractures are shown in dashed purple lines. Tafoni development scale indexes are shown in each profile in grey boxes, where I corresponds to well-developed tafoni and III to poorly-developed tafoni, as proposed in Table 7.

4 CHAPTER FOUR: DISCUSSION AND CONCLUSIONS

4.1 DISCUSSION

4.1.1 About Platforms

As explained before, the nature of the distinct feature that characterizes Punta de Tralca Peninsula, the platform sequence, is one worthy of debate. Although it strongly resembles wave-cut platforms, some of the recognized and mapped surfaces may not correspond to that geomorphological process. In particular, platforms that cover a scarce area in relation to the whole peninsula -like P2 or P3-, could be interpreted as stumbling blocks or relicts of higher previously eroded levels responding to this blocky-pattern erosive process affecting the area.

Another remark that supports this idea, is the apparent SW-dipping of P2 as seen from the SE area of the peninsula to the NW (Figure 32), that actually corresponds to an exposed quartz-plagioclase-biotite vein (Figure 42) probably emplaced through a fracture long before the tonalite outcropped and started to be eroded by exogenous processes. This exposed-vein related surface appears to be the continuation of P2 to the SW, denoting how fracturing can be easily confused with the expected dipping wave-cut surfaces. The erosive pattern triggered by the joint sets present at Punta de Tralca is observed throughout the whole study area and comprises a challenge when determining the origin for these morphologies.

A criterion used in the field to define a wave-cut origin for the lower platforms, P5 and P6, was comparing platform seaward dips to adjacent fracture orientation and spacing at contiguous scarps (when possible), in order to discard a joint-related origin for the surface. Also, grooves carved in the surface at different heights, dipping towards the ocean and disposed parallel to the tide front (or very local shoreline) were interpreted as possible inner edges, denoting past tidal levels (Figure 57).

According to the elevation range for P5 and P6 (~ 4 and ~ 7 m a.s.l., respectively), a regional correlation with MIS 1 terraces and/or deposits described along the coast north to Punta de Tralca (Ota et al. (1995); Encinas et al. (2006); Saillard et al. (2009); Saillard et al. (2012); Martinod et al. (2016)) could be proposed, where MIS 1 terraces have been recognized by the referenced authors at elevations varying from 3.8 – 10 m above sea level. However, in this work no dating analysis were developed, therefore P5 and P6 are suggested to correspond to Holocene wave-cut platforms with a higher confidence.

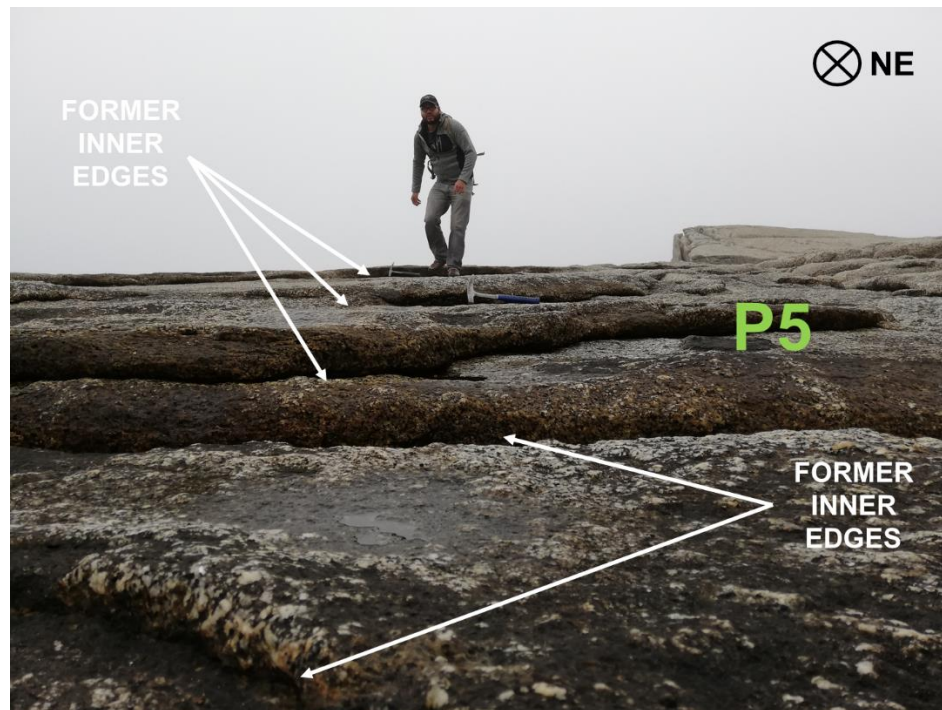


Figure 57. Grooves found at platform P5 interpreted as former inner edges dipping towards the ocean. Hammers for scale. Field photo by the author. Photo-shot location and orientation shown in Annex 2.

Regarding the main level comprising the whole peninsula, P4 (~ 20 m a.s.l.), it is suggested to correspond to an uplifted wave-cut platform (in contrast to mainly wave-built landform), due to the vast presence of tonalite outcrops at ground level, and predominant soil development in contrast to littoral or eolian deposits. It can also be correlatable in

height with regional surfaces inland that resemble marine terraces, either displayed locally or conforming discontinuous surfaces along the proximal coastal areas in the region (Guerrero (in prep.)).

Platforms P3 and P2 are not extensively preserved in the area, obstructing their analysis. Both of them are mainly preserved at the NW side of the main staircase-like tower, facing Punta de Tralca beach and bay. This fact comprises a certain level of uncertainty when attempting to classify these as wave-cut formed surfaces. They could have been formed as relict borders of a former older sea stack, say, around P1). Hints about former extension and characteristics that may have helped their study, are no longer available due to erosion; consequently, a wave-cute origin for these surfaces should not be entirely discarded. Moreover, they will be considered as such for some examples within the tectonic analysis developed in section 4.1.4.

Platform P1 comprises the top of the sequence and the highest elevation (~ 30 m a.s.l.) measured in the whole peninsula. No deposits nor inner edges are observed in this limited surface, and constant biogenic activity from different bird species is suggested to have hindered any evidence of the latter. Only some centimetric enclave tafoni can be spotted in the drone images (Figure 58).

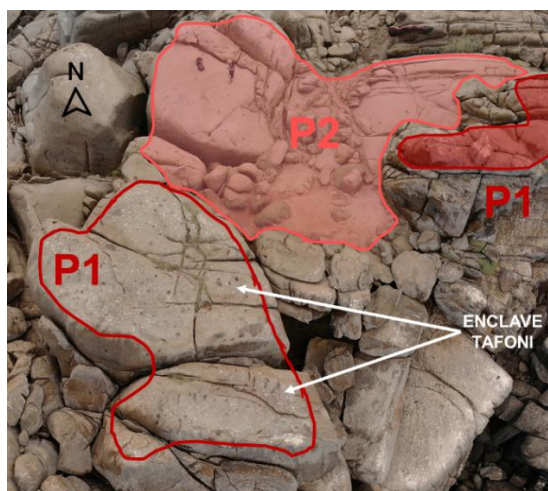


Figure 58. Platform P1 at the top of the staircase-like platform sequence, displaying enclave tafoni. Location of drone photo-shot shown in Annex 2. Person at P2 for scale.

Considering that the regional-scale uplifted marine terraces to the north and south of the area located at higher elevations than P1 are suggested to yield MIS 5 ages or older (Saillard et al. (2009); Rodríguez (2008); Jara-Muñoz et al. (2015); Martinod et al. (2016)), it can be suggested that P1 was formed during a MIS 5 substage (MIS 5a, MIS 5c or MIS 5e) or later in time, in the case of corresponding to a wave-cut platform.

4.1.2 About Fractures and Faults

The intense fracturing of the peninsula is one of the evident characteristics of the area. As shown in previous sections, 3 main sets are distinguished. The subvertical NE- and NW-striking sets can be related to the ETDS emplacement, since they are disposed following the same direction and fracture density increases when getting closer to the dikes.

Regarding the subvertical to inclined set, it has been vastly shown how it contributes to the blocky-pattern erosion of the tonalite, together with the NE and NW sets, comprising a difficulty when studying the platforms.

On a larger scale, it is hard to neglect the fact that the peninsula is displaced in a NW-striking preferential direction, as well as many other peninsulas along the Chilean coast. Coincidentally, the majority of the recognized faults observed in the coastal area around the region display the same orientation. This pattern is consistently observed along the coast and may be exerting a morphostructural control over the coastline development. This is suggested despite the fact that the major faults in the area, Melipilla and Río Maipo, are not directly north or south of Punta de Tralca. It has not been established whether one of these faults or even the branching feature of Melipilla Fault to the west is controlling the preservation of the peninsulas in this specific study area.

4.1.3 Tafoni and relative dating

Tafoni development in this peninsula is another distinct and interesting feature to pay attention to. They have been described in detail in this work as they comprise a complementary tool towards understanding temporality of tectonic and geomorphological history of this constrained study area. Also, their tentative distribution in terms of development per platform is displayed in the topographic profiles shown in Figure 56.

Firstly, and from fieldwork observations, it is concluded that tafoni development is currently active in the peninsula. Only some areas, like part of the SE face of the distinct “tower” that comprises the platform sequence, show tafoni-inactivity due to lichen covers that inhibit their development. This biogenic layer constitutes a protective shield against erosion and weathering. It is also not a coincidence that in the areas that are sheltered from direct sunlight, lichens have developed more intensely and tafone development has become somewhat or completely inactive.

In addition to these observations, the extense fine to coarse-grain deposit covering most of P4 (eolian and *in situ* weathering origins), supports the hypothesis of a currently active erosional and weathering process. Even inside tafoni (regular and enclave, mainly) grains and flakes are found from mechanical breakdown of the rock (Figure 51, (F)).

Regarding the temporal analysis that can be established from tafoni depth measurements, it is important to firstly understand the possible and inherent biases related to the attempt of studying a place like this, where erosion is constantly removing blocks and, therefore, implying considerable information loss. From fieldwork observations, it is noticed how regular tafoni are not as abundant as expected to be in upper levels of the main staircase-like hillock and, instead, the best-developed tafoni of this kind are found at P4 (Figure 51).

Moreover, well-developed regular type tafoni are also observed in lower platforms like P5 or P6; nonetheless, these are contained in loose blocks that are currently lying there but that are most likely to proceed from upper levels (Figure 59). It is not appropriate -or yet possible- to attempt to relate an isolated fallen block to a specific upper platform, even if it shows flagrant tafoni development in it, since it probably continued to be eroded while lying at that lower level. Besides, outcrops or boulders located closer to sea level (although not permanently covered by waves, which protect the rock from sea-salt crystallization weathering), are more likely to be weathered in a faster rate than higher and relatively drier areas that do not get as much sea spray, hence, more amount of salts that favor chemical and consequent mechanical weathering (this is valid for comparisons between a boulder and a corresponding outcrop of origin above the sea spray weathering zone).



Figure 59. Well developed (Type I) regular tafone found in a loose block at platform P5 scarp. Field photo by author.

Another process to have in mind when analyzing tafoni development in upper platforms as an indicator of time is, as a matter of fact, the issue of constant block detachment. This, because every time a tafoni-containing block is detached from its original outcrop, the temporal information those tafoni beheld is instantly lost, resetting tafoni development in that location, and comprising a bias when measuring the remaining and recently exposed wall or surface. In that situation, measurements are more likely to correspond to new tafoni and, therefore, estimated ages of exposure time for that surface could be highly underestimated. An analogous situation where that kind of underestimation could be incurred into, would be the determination of a cosmogenic isotope age in a surface without the consideration of erosion rates affecting that very surface. In that case, isotopes contained in the eroded mineral grains are removed from the surface, lowering the final isotope count and deriving in exposure age underestimation (Martinod et al. (2016)). This is why current cosmogenic isotope-related studies take into account erosion rates in their analysis.

In the present study, ages for tafoni development (surface exposure) will be calculated using the greatest depths measured for these morphologies (Table 9). This, because the aim is to obtain a minimal age for tafoni initiation (implicitly considering possible resetting of these processes), one that will hopefully be correlatable to the emergence time of other regional scale surfaces of known ages, as well as uplifting episodes for younger ones (P5, P6, or P7 eventually), triggered by seismic activity.

In addition to the block-loss bias mentioned before, one about tafoni types could also be addressed. From worldwide studies and cavernous weathering type analysis, it is fairly known that some factors can trigger higher rates for tafoni development. One of these factors is the presence of preexistent joint sets that comprise weakness planes through which erosion can act in a more effective way and condition the shapes of tafoni (Roqué et al. (2013)).

This is broadly observed at Punta de Tralca, where the weirdest and most irregular tafoni forms are directly responding to the 3 main existing joint sets, as shown previously. This also applies for enclave tafoni, since the lithological difference between enclaves and country rock already implies differential erosion acting on the rock. The interface between the enclave boundary and the country rock comprises a weakness plane. No wonder why almost every enclave at the peninsula displays this feature.

Bearing this in mind, the most reliable result to be obtained in any study of this kind, should be one obtained considering regular tafoni measurements in areas with preferably less complex erosive conditions. In order to use the other two types of tafoni in a more reliable way, a different model considering new variables (different than the ones proposed by Matsukura & Matsuoka (1991) or Sunamura (1996)) would probably have to be proposed.

Nonetheless, this present study will analyze and calculate ages for the three proposed types of tafoni using the methodology proposed by Sunamura (1996), since one of its goals is to show how tafoni can comprise a useful tool for a temporal analysis of this kind, rather than attempt to calculate an absolute exposure age, which would be a far-fetched goal given the complex Punta de Tralca scenario.

Taking into account everything that has just been exposed, age calculations are explained as it follows.

After literature research, it is considered that the methodology and equations (Equation (4)) proposed by Sunamura (1996) are appropriate for the temporal analysis of these tafoni as well (see Figure 16 for tafone evolution based on Sunamura (1996) model). As stated before, when calculating initiation ages for tafoni or surface exposure ages, it is important to consider two other variables besides time, t (years), and depth, z (cm): there is a time lapse, t^* (years), between rock exposure and effective initiation of tafoni growth, because weathering processes do not affect the rock instantly. The concept of weathering

front has been proposed and corroborated (Conca & Rossman (1985); Oguchi et al. (1994); Sunamura (1996); Brandmeier et al. (2010)) through the study of mineralogy variations with depth. This weathering front inward boundary determines the portion of the host rock that is being currently altered. The depth of the weathering front from the original rock surface is the variable z_c (cm). Equation (4) shown in Figure 15 relates these variables:

$$z = z_c \left(1 - \sqrt{\frac{t^*}{t}}\right). \quad (4)$$

Understanding these concepts, some conditions proposed by Sunamura (1996) have to be established in order to use Equation (4). For instance, the depth of the weathering front must be at least the same as the tafone depth; therefore, if the weathering front is not advancing and the depth of the tafone (the distance from the original surface of the rock to the current one, that represents the loss of material quantified as cm in one dimension or axis) reaches the weathering front inward boundary, they would reach the same value; that is,

$$z = z_c$$

If this condition is met, it means that the tafone is inactive. No weathering is acting on the rock inwards. On the other hand, if the tafone is active, the following condition must be set:

$$0 \leq z \leq z_c$$

This means the weathering front boundary is acting deeper than the current surface of the cavern, hence, the tafone is growing. About the temporal variables, an expected condition would be the following:

$$t^* \leq t$$

This means that the initiation of the tafone does not happen until a time lapse has passed in which the weathering front has already altered the minerals in the rock and therefore the material removal occurs. From that moment onwards, the tafone exists and can be studied.

Despite both variables, t^* and z_c , not been estimated for this study case (this could be done with a tonalite tensile strength profile for the obtention of strength reduction coefficients -like variable k explained in the Tafoni section 1.8, Chapter One- or else), some coherent assumptions can be made and are consistent with the methodology and argumentation proposed by Sunamura (1996). In his work and this, the functional form of the variables -for instance, k - rather than the value itself is relevant to these studies.

According to that argumentation, the maximum depth values measured in each tafone type (Table 9) are considered in this calculation; this, because they are expected to better represent the minimal exposure age of the surface, assuming they have been developing for a longer period of time. Consequently, the following reasoning is presented.

For the case of regular tafoni, the most representative and developed are located at P4 and reach depths of 45 cm (Table 9). Since tafoni in this area are still active (tonalite grains and flakes are visible inside cavities and salt crystals are observed as well), the weathering front, z_c , must be located deeper than 45 cm from the estimated original surface. Mottershead & Pye (1994), study tafoni development in coastal UK greenschists and determine the location of the weathering front based on chlorine penetration of the weathering surface as determined by X-ray fluorescence. For different samples, the maximum value obtained for $(z_c - z)$, was 68 mm. Since a homogeneous intrusive rock like Punta de Tralca tonalite is more resistant to weathering conditions, different and smaller values for z_c than the one obtained by Mottershead & Pye (1994) are considered in the calculation.

In the case of the time lapse, Sunamura (1996) calculates a $t^* = 35$ years for tuffaceous conglomerate at the tip of the Boso Peninsula of Japan. Since tonalite is harder and relatively more resistant than tuffaceous conglomerate, it can be assumed that t^* in this case is greater. Different case scenarios for each type of tafone are presented in Table 10 with the resulting calculations. Also, different values for t^* and z_c are considered for each type of tafone; this, because it is clear that (1) tafoni will develop faster through preexistent joints in relation to a massive homogeneous rock -as regular tafoni would-, (2) they will also develop at higher rates in mafic enclaves rather than in homogeneous tonalite, and (3) tafoni will develop faster through joints than enclaves given the increased availability of weakness planes. It is also likely that z_c is greater for enclaves rather than for tonalite. Field observations support this idea and these considerations were taken into account when choosing suitable values for these variables. These values are indicated in Table 10 for each type of tafone.

As a first approach towards understanding the temporal development of tafoni, it is noticeable how regular tafoni yield the longest exposure time span. This is a consequence of the criteria used when determining the values for the used equation. Another first order observation is the fact that calculated exposure ages seem to decrease with elevation. This apparent contradiction can be explained using the same reasoning for platform origin analysis: since erosional processes play a major role in the current topography of the platform sequence, an important information loss regarding tafoni development in upper (therefore, long exposed) platforms is expected. Fallen blocks lying in lower platforms may behold well-developed tafoni that long before belonged to upper levels.

Second order observations, consist in enclave tafoni calculations being somewhat constrained, showing a mean exposure age close to 400 years BP (year ~ 1620 C.E.). This was expected due to similar enclave tafoni dimensions measured all over the upper levels. No substantial difference between enclave tafoni depth in upper and lower levels is observed, despite that upper enclaves are expected to yield older exposure ages. This could be explained with the information-loss criterion explained in the previous paragraph.

Additionally, exposure ages for joint tafoni also yield interesting results. Great variations in the results are observed and appear to be directly related to the depths measured in the field. Nonetheless, and in spite of joint tafoni developing at expected significantly higher rates, the fact of considering the depth reached by the fractures into the rock for the calculus, could derive to misleading measurements. This, because it is not possible to know the extension of the fractures when they were originally formed. If the formation of these joint sets was indeed triggered by an overall extension of the peninsula, and each uplifting or extensional event that affected the coastal area intensified the fractures penetrative action, depth would not be a suitable parameter to run this calculation. In that likely case, joint tafoni width could possibly fit better into the model. Or even so, joint tafoni could be fairly discarded from this kind of analysis.

Further analysis when choosing suitable values for the equation inputs, depicts high sensibility of both, t^* and z_c , for relatively small tafoni -in comparison to those studied by Sunamura (1996) and other references mentioned before-, like the ones found at Punta de Tralca. It is noted that this equation works best for metric-scale tafoni studies, if the values for the variables are speculative rather than empirical.

In spite of the latter, regular-type tafoni seem to yield the most coherent results in this kind of analysis. Also, the most reliable regular-type tafoni observed at Punta de Tralca Peninsula are the ones observed at P4; therefore, a temporal analysis is addressed and discussed around those values.

The obtained exposure age for platform P4 at ~ 20 m a.s.l., ranges from ~ 15 to ~ 83 ka BP. If attempting to correlate this age with a sea level highstand, a coherent corresponding MIS would be MIS 3. If these simplified calculations comprised a higher error, a MIS 5 age could be in agreement with the results. Understanding that this tafoni study is only a first-

approach tool for temporal analysis, this kind of correlations would have to be supported by other means as well.

Nevertheless, results obtained seem coherent with the estimation of a maximum age for P1 from elevation comparisons, as discussed in section 4.1.1. P1 should not have been formed or exposed before MIS 5 (e.g., MIS 7 or older); therefore, P4 should also be correlated to a MIS 5 highstand (MIS5e, MIS5c, or MIS5a) or a more recent one (e.g., MIS 3). Platforms in between P1 and P4, consequently, should correlate to MIS5 substages in the case of being wave-cut platforms.

As a tool for relative temporal analysis, these calculations seem to fairly represent the expected behavior of tafoni development as a function of weathering action in a temporal scale.

Finally, and in order to improve the accuracy of the obtained ages, additional analysis such as Schmidt hammer, Cone Intender, ARHT testing or other rock-resistance quantification methods and penetration tools, should be applied in this study area. Variation of strength with time, mineral or element content (kaolinite and chlorine, for instance), determination of the weathering front through rock thin-section study at different depths, could significantly help improve these results.

$t^* = 10; 20$ $Z_c - Z = 15; 25$	Z (cm)	Z_c (cm)	t^* (yrs)	t (yrs)
P1	40	55	10	134
P1	40	55	20	269
P1	40	65	10	68
P1	40	65	20	135
P2	200	215	10	2.054
P2	200	215	20	4.109
P2	200	225	10	810
P2	200	225	20	1.620
P3	70	85	10	321
P3	70	85	20	642
P3	70	95	10	144
P3	70	95	20	289
P4	40	55	10	134
P4	40	55	20	269
P4	40	65	10	68
P4	40	65	20	135

JOINT TAFONI

$t^* = 50; 70$ $Z_c - Z = 3; 5$	Z (cm)	Z_c (cm)	t^* (yrs)	t (yrs)
P1	1	4	50	89
P1	1	4	70	124
P1	8	13	50	338
P1	8	13	70	473
P2	5	8	50	356
P2	5	8	70	498
P2	5	10	50	200
P2	5	10	70	280
P3	5	8	50	356
P3	5	8	70	498
P3	5	10	50	200
P3	5	10	70	280
P4	5	8	50	356
P4	5	8	70	498
P4	5	10	50	200
P4	5	10	70	280

ENCLAVE TAFONI

$t^* = 100; 150$ $Z_c - Z = 2; 4$	Z (cm)	Z_c (cm)	t^* (yrs)	t (yrs)
P1	10	12	100	3.600
P1	10	12	150	5.400
P1	10	14	100	1.225
P1	10	14	150	1.838
P2	35	37	100	34.225
P2	35	37	150	51.338
P2	35	39	100	9.506
P2	35	39	150	14.259
P3	20	22	100	12.100
P3	20	22	150	18.150
P3	20	24	100	3.600
P3	20	24	150	5.400
P4	45	47	100	55.225
P4	45	47	150	82.838
P4	45	49	100	15.006
P4	45	49	150	22.509

REGULAR TAFONI

Table 10. Tafoni initiation ages for each type of tafoni considering different values for t^* and Z_c . Values are indicated in the upper-left corner of each table.

4.1.4 Uplift of the peninsula and seismic activity

As a first order observation, the well-defined staircase comprising the main feature of the peninsula suggests a wave-cut related genesis. Since the steps of this staircase-like hillock are displayed at different elevations, coseismic uplift episodes as well as long-term deformation are suspected to be strongly linked to the presence and development of these platforms at Punta de Tralca.

These episodes would have uplifted platform after platform, ceasing wave-cut activity on them, and therefore preserving each level at different heights, for which a temporal scale can be ascribed. Although this could be fairly valid for every platform being all of them alike, after a detailed analysis and understanding of the area's erosional dynamics, it is suggested that platforms P1, P4, P5 and P6, could correspond to original wave-cut platforms with significant certainty. The lowest platform, P7, is subject of speculation since it is mainly covered by wave action and its characteristics and extension cannot be properly defined. Nevertheless, P7 should be expected to emerge over-tide eventually within successive coseismic uplift episodes, as well as through long-term regional uplift.

Firstly, a long-term analysis is addressed, following the reasoning proposed at the end of section 4.1.3, supported by height correlation and tafoni-based exposure ages for the platforms.

As in many marine terrace studies, the elevation parameter that correlates better to the associated sea level highstand during the formation of the platform, is the shoreline angle or inner edge, located in the intersection of the seaward dipping surface and a scarp plane delimiting the platform landward extension. This shoreline angle concept is used by most if not all of the works referenced in section 1.4.2.1 regarding this topic.

In the case of Punta de Tralca, since it is a peninsula, no regular cliffs following the actual shoreline are present, so maximum heights for each platform are used (Table 11).

Platforms	Elevation range (m a.s.l.)	Maximum elevation (m a.s.l.)
P1	29 - 31	31
P2	24 - 28	28
P3	22 - 24	24
P4	17 - 21	21
P5	4 - 11	11
P6	1 - 5	5
P7	Unknown	-1

Table 11. Elevation range and maximum elevation for each platform mapped at Punta de Tralca Peninsula.

From Table 11 and paleo sea-level curves and ages (Table 12), schematic correlations between platforms and sea-level highstands are proposed, including the correspondent long-term uplift rate (Figure 60).

Marine Isotope Stage (MIS)	Age MIS (ka)	Age MIS from	Sea level elevation (m a.s.l.)	Sea level elevation from
MIS 5e	~ 125	Hearty et al. (2007); Pedoja et al. (2011, 2014)	+ 6	Creveling et al. (2017)
MIS 5c	~ 100	Broecker et al. (1968); Mesolella et al. (1969)	-9.4 ± 5.3	Creveling et al. (2017)
MIS 5a	~ 80	Creveling et al. (2017)	- 8.5 ± 4.6	Creveling et al. (2017)
MIS 3	~ 44	Pico et al. (2016)	- 38 ± 7	Pico et al. (2017)
MIS 1	~ 6	Lambeck et al. (2002)	- 4 ± 1	Lambeck et al. (2002)

Table 12. Sea level highstands and their correspondent MIS stage or substage, MIS age and reference.

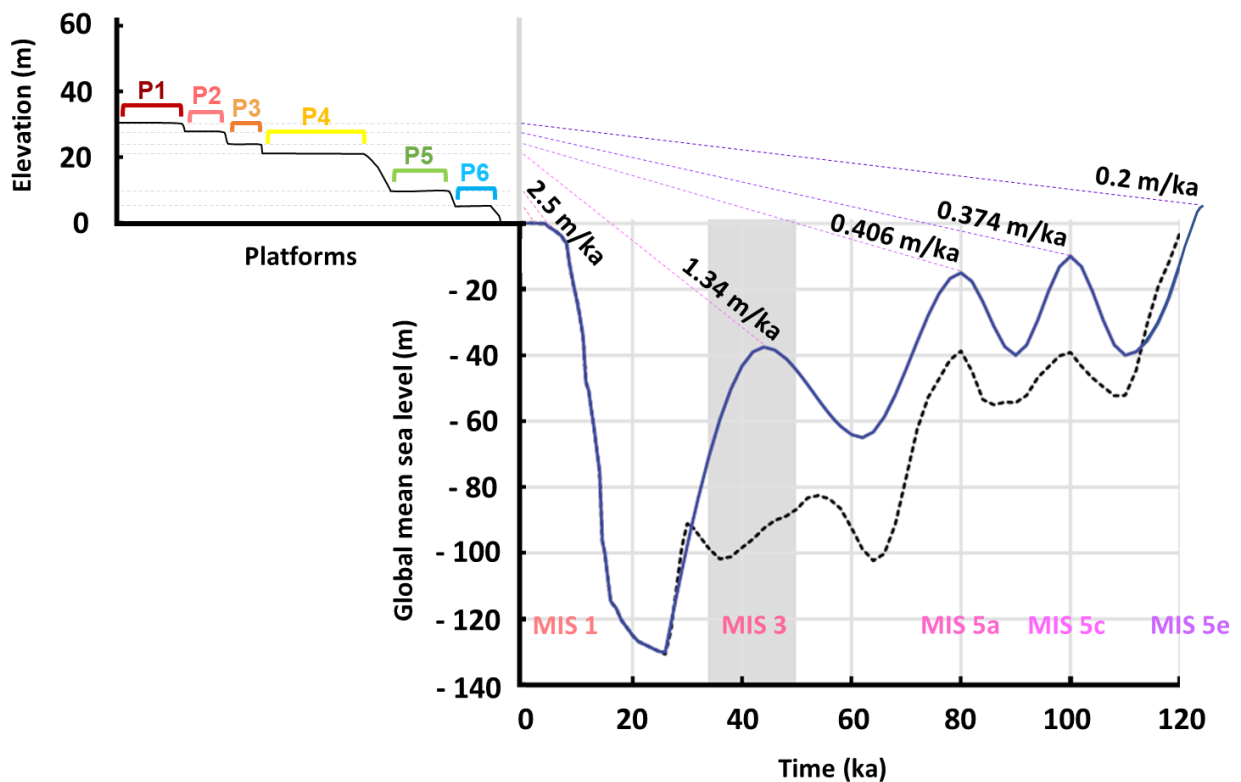


Figure 60. Schematic simplified potential correlation of the platform sequence at Punta de Tralca Peninsula to the late Quaternary global sea level curve based on Lambeck et al. (2002), Creveling et al. (2017), and Pico et al. (2017). Approximate ages used are based on Broecker et al. (1968), Mesolella et al. (1969), Lambeck et al. (2002), Hearty et al. (2007), Pedoja et al. (2011, 2014), Pico et al. (2016), and Creveling et al. (2017).

The correlation between the platforms and sea level highstands presented in Figure 60, comprises a simplified schematic model applicable for the analysis of wave-cut platform or marine terrace sequences formation, especially when having dated samples for the studied surfaces, which would refine the calculations for long-term uplift estimations. In the particular study case presented here, no such dating is available but is certainly suggested for further analysis.

Additionally, some recovery percentages for the model presented in Figure 60 have been estimated as a first approach for 3 main levels in order to check if interseismic subsidence values agree with observations in other coastal areas (Table 13). Interseismic subsidence rates broadly vary between 0 – 1 (mm/a) (e.g., Wesson et al. (2015); González-Alfaro et al (2018); among other works referenced in section 1.4.2.1), so values within this range are chosen for recovery analysis.

Platforms	Maximum elevation (m)	Associated MIS stage	Associated MIS age	Sea level elevation (m a.s.l.)	Permanent vertical deformation % for different subsidence rates (S)			
					S = 0.1 mm/a	S = 0.3 mm/a	S = 0.5 mm/a	S = 1 mm/a
P1	31	MIS 5e	~ 125 ka	~ + 6	16.7	6.3	3.8	2.0
P2	28	MIS 5c	~ 100 ka	~ - 9.4	27.2	11.1	7.0	3.6
P3	24	MIS 5a	~ 80 ka	~ - 8.5	28.9	11.9	7.5	3.9
P4	21	MIS 3	~ 44 ka	~ - 38	57.3	30.9	21.1	11.8
P5	11	MIS 1	~ 11 ka	~ - 4	57.7	31.3	21.4	12.0
P6	5	Holocene	3 ka (*)	0 (*)	62.5	35.7	25.0	14.3

Table 13. Estimated percentage of permanent vertical deformation for each platform according to previously associated MIS stage ages and considering different subsidence rates based on literature referenced in the text. () Arbitrary values were chosen for the Holocene platform P6 in order to study the behavior of the parameter S.*

Regarding the rough estimates for long-term uplift, the values obtained for the main platform P4 and one of the Holocene platforms, P5, seem fairly coherent with measurements in other areas where marine terraces have been dated and studied to the north (up to Mejillones Peninsula) and to the south of Punta de Tralca (up to Arauco Peninsula) that show Quaternary uplift acceleration, as well as permanent deformation percentages between 10 – 30 % considering interseismic subsidence rates of 0.3 – 1 mm/a. In particular, for MIS 3 correlation, Melnick et al. (2006) estimates an uplift rate of 1.8 ± 0.4 m/ka at Santa María Island for the last ~55 ka. Jara-Muñoz & Melnick (2015), estimate an uplift rate of 1.5 ± 0.3 m/ka from radiocarbon dated paleosols in wave-built marine terraces at Santa María Island. González-Alfaro et al. (2018) estimates uplift rates

of 1.36 – 1.68 m/ka and 0.98 – 1.30 m/ka for the footwall and hanging wall of the Mejillones Fault, respectively, at Mejillones Peninsula in the north.

Holocene uplift rates though seem highly scattered along the coast, with estimated rates of ~ 0.4 m/ka at Algarrobo (Encinas et al. (2006)), ~ 0.41 m/ka at Bahía Tongoy (Ota & Paskoff (1993)), ~ 0.85 m/ka at Caleta Michilla (Leonard & Wehmiller (1991)), 3.1 – 9.6 m/ka at Chiloé (Hervé & Ota (1993)), ~ 6.3 m/ka at Isla Mocha (Nelson & Manley (1992)), 1.79 ± 0.18 m/ka at Playa Grande in Mejillones Bay and 0.61 ± 0.11 m/ka at Caleta Michilla (González-Alfaro et al. (2018)). This variability in estimated uplift rates has been usually attributed to morphostructural controls with associated nearby faults and other geological processes.

For specific results, see Paskoff (1970, 1977), Kaizuka et al. (1973), Leonard & Wehmiller (1991, 1992), Nelson & Manley (1992), Ota & Paskoff (1993), Hervé & Ota (1993), Ota et al. (1995), Ortlieb et al. (1996a), Marquardt et al. (2004), Encinas et al. (2006), Melnick et al. (2006), Rodríguez (2008), Saillard (2008), Saillard et al. (2009), Moreno et al. (2009), Farías et al. (2010), Regard et al. (2010), Farías et al. (2011), Vigny et al. (2011), Saillard et al. (2012), Moreno et al. (2012), Rodríguez et al. (2013), Baker et al. (2013), Jara-Muñoz et al. (2015), Jara-Muñoz & Melnick (2015), Martinod et al. (2016), Melnick (2016), Melnick et al. (2017), and González-Alfaro et al. (2018).

It is also important to note how MIS age correlations to platform elevation could be displaced, e.g. P4 corresponding to MIS 5a. Furthermore, some MIS platforms could be absent in this sequence. Also, poorly preserved platforms with uncertain wave-cut attributed origin such as P2 and P3, may not be suitable to correlate with MIS 5 substages. In any case, roughly estimated long-term uplift rates, still seem coherent with observations to the north and south of Punta de Tralca, indicating that the kind of temporal analysis presented in this work could be applicable with a certain confidence if dating for the platforms were available.

Regarding the lower and allegedly younger surfaces present at Punta de Tralca Peninsula, in order to establish a first order attempt to relate seismic events with coseismic uplift and the subsequent contribution to the emergence of the platforms, an extrapolation of coseismic uplift measurements from other regions within the country will be used in the analysis along with seismotectonic segmentation data along the central coast. As expected and shown previously in Table 4, coseismic uplift values for great events (magnitude $M > 7.5$) tend to increase with a higher magnitude in areas like peninsulas or segment boundaries (e.g., Melnick et al. (2009; Melnick et al. (2012a), Jara-Muñoz et al. (2015), Jara-Muñoz & Melnick (2015), Melnick (2016), Melnick et al. (2017), and González-Alfaro et al. (2018)). These values and ranges have been plotted in order to show this relationship in a simplified way, neglecting post or interseismic subsidence as a first approach. A lineal tendency segment has also been added to evince the latter (Figure 61).

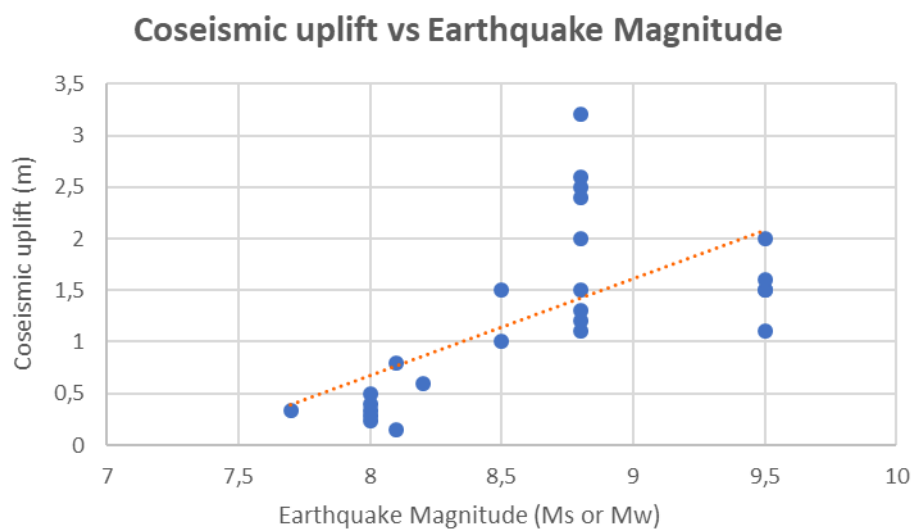


Figure 61. Measured coseismic uplift values for different earthquake magnitudes. Red dotted line shows lineal tendency of the data. Data derived from Table 4 (see references in it) and specific values for the construction of this graph are shown in Annex 1.

It is important to note how for the 1960 M_w 9.5 Valdivia earthquake, no coseismic uplift measurements were taken within the city, since its vicinity underwent a permanent subsidence of about 2.7 m (Plafker & Savage (1970)). Therefore, the data displayed in Table 4 and Figure 61 corresponds to measurements taken at approximately 300 km to the north of Valdivia, around the Arauco Peninsula.

Using this simplified tendency-graph, coseismic uplift values for the study area are suggested for undocumented events. The purpose of this, is to estimate the influence of recent earthquakes on the emergence of lower platforms (P5 and P6). Long term uplift and subsidence rates are not considered in this analysis, since the effect of the latter in this allegedly younger platforms was already addressed (Figure 60, Table 13) and one of the objectives of this work is to explore the short-term deformation scale as well.

Regarding the potential bias of not specifically assessing rupture location and length for each event that have affected the study area, for this thesis purposes, it is assumed that all the events affecting the area behave similarly enough in terms of setoff extent, although the concept of variable rupture and vertical deformation within the same is broadly recognized, as described in section 1.6.2 (see references therein). Comte et al. (1986) estimate rupture lengths for each of the mentioned events (Figure 62).

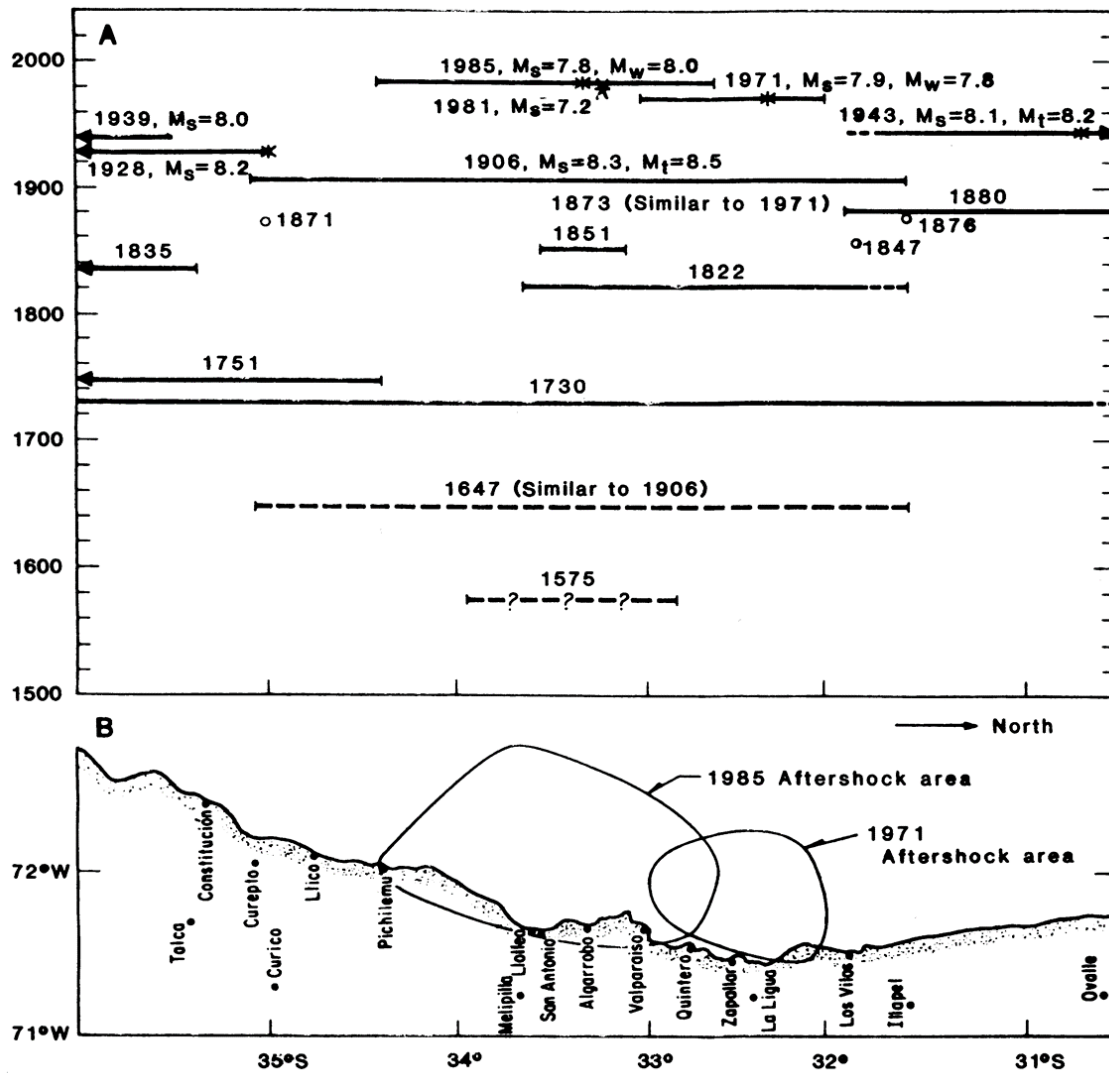


Figure 62. (A) Space-time diagram of central Chile earthquakes. Solid horizontal lines represent estimated rupture lengths. The arrows indicate that the rupture lengths extended farther in that direction. Dashed lines show uncertain rupture lengths. Dashed line with question marks for the 1575 earthquake reflects inadequate reports, which make the estimated rupture length very uncertain. Earthquakes of past centuries that were large but not great ($7.5 > M > 7$) and whose rupture lengths could not be estimated are shown by (O). Locations of this century's main shocks are shown by stars. M_S , M_W , and M_t are surface-wave, moment, and tsunami magnitudes (Abe (1981)), respectively. (B) Central Chile region and aftershock areas of the 1985 and 1971 earthquakes.

Obtained from Comte et al. (1986).

To sum up, and Table 14 are presented below. Minimum elevation values for each platform are considered as a standard and austere values for estimated coseismic uplift are chosen -according to examples from Table 4 and from Figure 61- in pursuance of minimizing biases within this simplified neotectonic analysis.

Year	Estimated Earthquake Magnitude	Estimated Coseismic Uplift (m)
1575	Ms 7.3	0.1
1647	Ms 8.5	1.0
1730	Mw 9.2	1.7
1822	Ms 8.5	0.9
1851	Ms 7.3	0.0
1906	Mw 8.2	0.6
1971	Mw 7.8	0.3
1981	Ms 7.5	0.1
1985	Mw 8.0	0.5
Accumulated coseismic uplift (m)		5.2

Table 14. Table shows measured values for coseismic uplift (see Table 4, References) highlighted in grey, and estimated minimum values from the lineal tendency set in Figure 61. Magnitudes M_s and M_w are surface-wave and moment, respectively. Bars at the side show the number of events -given their uplifting potential- that would have contributed to the rising of platforms P5 and P6. For this analysis maximum height values for each platform are used (Table 11). Estimated accumulated coseismic uplift for all documented earthquakes in the area is also shown.

Table 14 shows a rough estimate for the number of seismic events that would have triggered the uplift of platforms P5 and P6 in agreement with the current observed and measured heights. Since the coseismic uplift values were chosen sternly, it is suggested

that some of the earthquakes could have provoked even more uplift than the estimated here.

From Table 14, it is clear that high coseismic uplift, say a stern range of 0.5 – 1 m, is achieved with relatively high magnitude interplate events ($M > 8.0$), and every ~80 years. It is important to highlight though, that $M > 9$ events such as the 1730 Valparaíso tsunamigenic earthquake, have not occurred for 300 years. Considering a case scenario in which every large earthquake (1985, 1906, 1822, 1730, 1647, and 1575) uplifts Punta de Tralca homogeneously, a simple calculation can throw a tentative emergence period for the platform. This analysis is made despite the uncertainty of the upper platforms P1 – P3 being wave-cut originated and despite the fact that P1 – P4 are also uplifted at long-term scales; but would comprise a very suitable model for earthquakes happening in the last millennium.

The following equations, (5) and (6), are proposed by the author so rapid calculations for emergence time and number of events uplifting a platform can be made:

$$T_E = \frac{H_P}{U_C} \times S_C , \quad (5)$$

where T_E is the time of emergence for the platform (in years before present, BP), H_P is the current minimum height of the platform (in meters), U_C is the coseismic uplift value set by the user (in meters), and S_C represents a seismic cycle of 80 years in this case. For the number of events that uplifted the platform, in terms of the U_C and S_C values set by the user, Equation (6) is proposed:

$$N_E = \frac{H_P}{U_C} , \quad (6)$$

where N_E is the number of seismic events or earthquakes of sufficient magnitude so as to uplift the platform as much as a defined U_C value. Taking these equations into account,

hypothetical emergence times have been calculated for every platform (Table 15). Also, summary Table 16 is presented below in order to provide a better visualization of the analyzed information, where T_E values in years before present (BP) are shown in calendar or common era years (C.E.). Note how P5 and P6 are the ones potentially affected by human-recorded historical earthquakes. Also, a color index has been assigned to each recorded earthquake related to the study area (“N.R.” corresponds to non-recorded events).

Platforms	Elevation H_P (m)	T_E (years) ($U_C = 0.3$ m) N_E	T_E (years) ($U_C = 0.5$ m) N_E	T_E (years) ($U_C = 0.7$ m) N_E	T_E (years) ($U_C = 1.0$ m) N_E	T_E (years) ($U_C = 1.5$ m) N_E
P1	29	7733 97	4640 58	3314 41	2320 29	1547 19
P2	24	6400 80	3840 48	2743 34	1920 24	1280 16
P3	22	5867 73	3520 44	2514 31	1760 22	1173 15
P4	17	4533 57	2720 34	1943 24	1360 17	907 11
P5	5	1333 17	800 10	571 7	400 5	267 3
P6	1	267 3	160 2	114 1	80 1	53 1

Table 15. Estimated emergence time (T_E) in years before present (BP) for each platform considering different coseismic uplift values (U_C) calculated using Equation (5). The number of events or earthquakes (N_E) expected to have affected each platform has also been calculated using Equation (6)

Registered Earthquakes	1575	1647	1730	1822	1829	1851	1906	1971	1981	1985
Color Index										
Platforms	Year ($U_c = 0.3$ m)	Associated earthquake (year C.E.)	Year ($U_c = 0.5$ m)	Associated earthquake (year C.E.)	Year ($U_c = 0.7$ m)	Associated earthquake (year C.E.)	Year ($U_c = 1.0$ m)	Associated earthquake (year C.E.)	Year ($U_c = 1.5$ m)	Associated earthquake (year C.E.)
P1	5714 A.C.	N.R.	2621 A.C.	N.R.	1295 A.C.	N.R.	301 A.C.	N.R.	472 C.E.	N.R.
P2	4381 A.C.	N.R.	1821 A.C.	N.R.	724 A.C.	N.R.	99 A.C.	N.R.	739 C.E.	N.R.
P3	3848 A.C.	N.R.	1501 A.C.	N.R.	495 A.C.	N.R.	259 A.C.	N.R.	846 C.E.	N.R.
P4	2514 A.C.	N.R.	701 A.C.	N.R.	76 C.E.	N.R.	1360 C.E.	N.R.	1112 C.E.	N.R.
P5	686 C.E.	N.R.	1219 C.E.	N.R.	1448 C.E.	N.R.	1619 C.E.	1647	1752 C.E.	1730
P6	1752 C.E.	1730	1859 C.E.	1829 / 1851	1905 C.E.	1906	1939 C.E.	1971	1966 C.E.	1971

Table 16. Summary table showing the calculated exposure ages (in calendar or common era age (C.E.)) for platforms P4, P5 and P6 from Table 14 and the associated registered earthquakes for those values, considering different coseismic uplift long-term mean values (U_c) defined by the user. N.R. stands for “not recorded” seismic events

As shown in Table 16, exposure age calculations for the platforms can be associated to recorded events in different cases, depending on the expected values for U_c . For the case where $U_c = 0.3$ m, platform P6 possibly emerged for the 1730 earthquake (Ms 8.7). For $U_c = 0.5$ m, platform P6 tentatively emerged for either 1829 or 1851 earthquakes (Ms 7.0 and Ms 7.1, respectively). For $U_c = 0.7$ m, platform P6 possibly emerged for the 1906 earthquake (Mw 8.2). In the case where $U_c = 1.0$ m, platform P6 may have emerged for the 1971 earthquake, whereas platform P5 for the 1647 event (Mw 7.8 and Ms 8.5, respectively). Finally, in the extreme case scenario where $U_c = 1.5$ m, platform P6 would have emerged for the 1971 event and P5 for the 1730 one (Mw 7.8 and Ms 8.7, respectively).

Since every earthquake yields different characteristics and the coseismic uplift values and permanent deformation should therefore vary from event to event, values of 0.3 and 0.5 m are considered adequate as inputs in this simplified exercise in terms of mean expected coseismic uplift on a mid- to long- term basis, taking into account the lineal tendency of

earthquake magnitudes throughout recorded seismic history for this specific area and likely interseismic recovery of the vertical deformation. Consequently, platform P6 is suggested to have emerged due to long-term, as well as short-term tectonics, likely with the Mw 9.1 – 9.3 Valparaíso Earthquake in 1730. This same earthquake may have contributed to the intertidal exposure of platform P7. It is suggested that this kind of analysis is more suitable for calculations within even younger markers (~ 1 ka), that would consequently behold lower accumulated subsidence, therefore minimizing overestimations regarding earthquakes-uplifting potential.

Additionally, regional scale faults such as Melipilla Fault could have enhanced the uplift of the peninsula at the 1730 event and throughout the Holocene, favoring the preservation of the platform sequences at Punta de Tralca (see references in 1.4.2.1 about peninsulas and marine terraces). Besides, the presence of crustal faults within the submerged slope of the plate with similar strikes and fulfilling a similar morphotectonic role in the area, cannot be discarded. It is suggested that structures like these may favor the development and preservation of NW-striking peninsulas with their adjacent eastward bays, making temporal correlations about the emergence of morphological surfaces within, possible.

4.2 CONCLUSIONS

4.2.1 Concluding remarks

Punta de Tralca yields distinctive and interesting structural and geomorphological features that have been studied in this work in order to attempt a better understanding of the area's temporal dynamics. It has been broadly shown how these striking features also imply great difficulty within their analysis due to permanently ongoing intense erosive action.

In spite of this, a geomorphological and neotectonic study has been developed in the pursuance of a Quaternary temporal model for the development of the extensively alluded morphological features at Punta de Tralca Peninsula.

The different surfaces observed at Punta de Tralca can be classified as wave-cut platforms with a high confidence degree for the lower ones (P4, P5, and P6) and some uncertainty for the upper ones (P1, P2, and P3), since the mentioned erosive dynamics at the peninsula play an important role on modelling its topography.

The presence and study of tafoni in this work comprises a different and novel approach towards setting a relative timescale that could potentially support tectonic analysis. It was found though, that the complex erosive dynamic that takes place at Punta de Tralca, strongly biases this type of study as discussed in the previous chapter. This, in addition to the lack of specific more-accurate studies, comprises a limitation for the full comprehension of tafoni development and preservation in this distinct area. Nonetheless, and for the establishment of relative dating and understanding of tafoni evolution, the results obtained in this work -P4 potentially formed and emerged during MIS 3 or MIS 5a sea level highstands- and the discussion generated in regards of complications and biases, seems suitable for the case. It is expected that the kind of analysis depicted in this work can be replicated in other areas yielding similar characteristics.

In respect of the long-term tectonic analysis, coherent correlations with < MIS 7 sea level highstands are presented, supported by regional uplift rates that are consistent with observations to the north and south of Punta de Tralca Peninsula, as well as vertical deformation recovery values within ranges that are also consistent with previous observations for the Chilean coast. For a more detailed and accurate analysis, dating analyses should have to be carried out around the area.

Regarding short-term tectonics, the higher confidence degree about the results obtained from this analysis, correspond to the potential emergence the shallower areas within platform P6 attributed to the Mw 9.1 – 9.3 Valparaíso Earthquake in 1730. It is suggested that this kind of simplified analysis is more suitable for emergence date calculations for even shallower markers and considering events that have occurred within the last millennium.

Finally, and considering the general and specific objectives set for this thesis, it is concluded that the methodology and consequent analysis of the information gathered from Punta de Tralca Peninsula, is adequately developed within the expected and discussed limitations proper of this kind of geological dynamic and partially indecipherable landscape.

4.2.2 Suggestions for future work

As stated before and in order to improve the accuracy of the obtained ages, additional analysis such as Schmidt-hammer, Cone Intender, ARHT testing (Conca & Cubba (1986)) or other rock-resistance quantification methods and penetration tools, could be applied in this study area. Variation of strength with time, mineral or element content (kaolinite and chlorine, for instance), determination of the weathering front depth (z_c) through rock thin-section study at different depths among other analysis, could significantly help improve these results.

Suzuki & Hachinohe (1995) gathered data on rock strength in relation to depth at Boso Peninsula, Japan. They used a needle-type penetrometer in a core from a boring drilled vertically into the bedrock, a fine sandstone of Pliocene age. For the case of Punta de Tralca, the realization of an analogue test is suggested in order to find a suitable function for the behavior of strength-reduction coefficient, k , and consequently, an adequate equation for rock strength, S .

Stephenson and Kirk (2000b) ran several Schmidt-hammer tests to determine the degree of reduction in rock strength due to weathering, comparing rebound values between weathered and unweathered exposed rock surfaces. In fact, in recent works, Schmidt hammer test has become a routine methodology to quantify the overall hardness of shore platforms (e.g. Cruslock et al., 2010).

Additionally, and in order to achieve greater accuracy in the determination of long-term tectonics regarding the formation and emergence of the platforms of Punta de Tralca, dating methods should be applied in the study area. In particular, cosmogenic isotope dating is proposed (^{10}Be exposure age models), since no significant deposits are preserved in the area for luminescence dating.

5 BIBLIOGRAPHY

- Abe, K. (1981). Physical size of tsunamigenic earthquakes of the northwestern Pacific. *Physics of the Earth and Planetary Interiors*, 27(3), 194-205.
- Aguilar, G., Riquelme, R., Martinod, J., & Darrozes, J. (2013). Rol del clima y la tectónica en la evolución geomorfológica de los Andes Semiáridos chilenos entre los 27°-32° S. *Andean geology*, 40(1), 79-101.
- Allmendinger, R. W., Isacks, B. L., Jordan, T. E. & Kay, S. M. (1997). The evolution of the Altiplano-Puna plateau of the Central Andes. *Annual Reviews of Earth Science*, 25, 139–174.
- Álvarez, L. (1963). Studies made between Arauco and Valdivia with respect to the earthquakes of 21 and 22 May 1960. *Bull. Seismol. Soc. Am.*, 53, 1315–1330.
- Álvarez, P. P., Godoy, E. & Giambiagi, L. (1999). Estratigrafía de la Alta Cordillera de Chile Central a la latitud del paso Piuquenes (33°35' LS). *In: Proceedings of the XIV Congreso Geológico Argentino, Salta, Argentina*, 1, 55.
- Ammon, C. J., Lay, T., Kanamori, H., & Cleveland, M. (2011). A rupture model of the 2011 off the Pacific coast of Tohoku Earthquake. *Earth, Planets and Space*, 63(7), 33.
- Anderson, R. S., Densmore, A. L., & Ellis, M. A. (1999). The generation and degradation of marine terraces. *Basin Research*, 11(1), 7-19.
- Angermann, D., Klotz, J., and Reiberg, C. (1999). Space-geodetic estimation of the Nazca–South American Euler vector. *Earth and Planetary Science Letters*, v. 171, p. 329–334, doi: 10.1016/S0012-821X(99) 00173-9.
- Araujo, M., Suárez, G. (1994). Geometry and state of stress of the subducted Nazca plate beneath central Chile and Argentina: evidence from teleseismic data. *Geophysical Journal International*, Vol. 116, 2, p.283-303.
- Arce, M. (2002). Condiciones de formación y naturaleza de las estructuras del complejo plutónico Santo Domingo, V Región: evidencias de terreno y de

fábricas magnéticas. *Memoria de Título (Unpublished)*, Universidad de Chile, Departamento de Geología: 80 p.

- Armijo, R., Rauld, R., Thiele, G., Vargas, J., Campos, R., Lacassin, R. & Kausel, E. (2010). The West Andean Thrust, the San Ramón Fault, and the seismogenic hazard for Santiago, Chile. *Tectonics*, 29, TC2007, <http://dx.doi.org/10.1029/2008tc002427>
- Armijo, R., Lacassin, R., Coudurier-Curveur, A., & Carrizo, D. (2015). Coupled tectonic evolution of Andean orogeny and global climate. *Earth-Science Reviews*, 143, 1-35.
- Aron, F., Cembrano, J., Astudillo, F., Allmendinger, R. W., & Arancibia, G. (2015). Constructing forearc architecture over megathrust seismic cycles: Geological snapshots from the Maule earthquake region, Chile. *Bulletin*, 127(3-4), 464-479.
- Ashby, J. R., Ku, T. L., & Minch, J. A. (1987). Uranium series ages of corals from the upper Pleistocene Mulege terrace, Baja California Sur, Mexico. *Geology*, 15(2), 139-141.
- Astroza, M.; Moya, A.; Sanhueza, S. (2002). Estudio comparativo de los efectos de los terremotos de Chillán de 1939 y de Talca de 1928. *In Jornadas Chilenas de Sismología e Ingeniería Antisísmica, No.8. Valparaíso, Chile.*
- Astroza, M.; Sandoval, M.; Kausel, E. (2005). Estudio comparativo de los efectos de los sismos chilenos de subducción del tipo intraplaca de profundidad intermedia. *In Jornadas de Sismología e Ingeniería Antisísmica, No. 9. Concepción, Chile.*
- Audin, L., Lacan, P., Tavera, H., Bondoux, F. (2008). Upper plate deformation and seismic barrier in front of Nazca subduction zone: the Chololo Fault System and active tectonics along the Coastal Cordillera, southern Peru. *Tectonophysics* 459, 174-185.
- Baker, A., Allmendinger, R.W., Owen, L. A. & Rech, J. A. (2013). Permanent deformation caused by subduction earthquakes in northern Chile. *Nature Geosci.* 6, 492-496.

- Bangs, N., and Cande, S.C. (1997). Episodic development of a convergent margin inferred from structures and processes along the southern Chile margin. *Tectonics*, v. 16, p. 489–503, doi: 10.1029/97TC00494.
- Barrientos, S. E. (1988). Slip distribution of the 1985 Central Chile earthquake. *Tectonophysics* 1, 45, 225-241.
- Barrientos, S. (2007). Earthquakes in Chile. The geology of Chile. *The Geological Society, London*, 263-287.
- Barrientos, S., and National Seismologic Center team. (2017). Informe final sobre la secuencia sísmica en Región de Valparaíso. *National Seismologic Center website*. www.csn.uchile.cl
- Beck, S., Barrientos, S., Kausel, E., and Reyes, M. (1998). Source characteristics of historic earthquakes along the Central Chile subduction zone: *Journal of South American Earth Sciences*, v. 11, p. 115–129, doi: 10.1016/S0895-9811(98)00005-4.
- Bilek, S.L., Schwartz, S.Y., DeShon, H.R. (2003). Control of seafloor roughness on earthquake rupture behavior. *Geology* 31, 455-458.
- Bilek, S. L. (2007). Influence of subducting topography on earthquake rupture. *The Seismogenic Zone of Subduction Thrust Faults*, 123-146.
- Blackwelder E. (1990). The hardness of ice. *American Journal of Science* 238: 61–62.
- Bodin, R; Klinger, T. (1986). Coastal uplift and mortality of intertidal organisms caused by the September 1985 Mexico earthquakes. *Science* 233: 1071- 1073.
- Borde, J. (1966). Les Andes de Santiago et leur avant-pays: étude de géomorphologie. 559 s. pp., *Union française d'impression, Bordeaux*.
- Bradley, W. C. (1957). Origin of marine-terrace deposits in the Santa Cruz area, California. *Geological Society of America Bulletin*, 68(4), 421-444.

- Bradley, W. C., & Griggs, G. B. (1976). Form, genesis, and deformation of central California wave-cut platforms. *Geological Society of America Bulletin*, 87(3), 433-449.
- Brandmeier, M.; Kuhlemann, J., Krumrei, I., Kappler, A., Kubik, P.W. (2010). New challenges for tafoni research. A new approach to understand processes and weathering rates. *Earth Surface Processes and Landforms*, 36, 839-852.
- Briggs, R. W., Engelhart, S. E., Nelson, A. R., Dura, T., Kemp, A. C., Haeussler, P. J., ... & Bradley, L. A. (2014). Uplift and subsidence reveal a nonpersistent megathrust rupture boundary (Sitkinak Island, Alaska). *Geophysical Research Letters*, 41(7), 2289-2296.
- Broecker, W.S., Thurber, D.L., Goddard, J., Ku, T.L., Matthews, R.K., Mesolella, K.J., (1968). Milankovitch hypothesis supported by precise dating of coral reefs and deep-sea sediments. *Science* 159, 297e300.
- Brooks, B. A., Bevis, M., Smalley Jr, R., Kendrick, E., Manceda, R., Lauría, E., ... & Araujo, M. (2003). Crustal motion in the Southern Andes (26°–36° S): Do the Andes behave like a microplate?. *Geochemistry, Geophysics, Geosystems*, 4(10).
- Cahill, T.; Isacks, B. L. (1992). Seismicity and shape of the subducted Nazca plate. *Journal of Geophysical Research*, 97, 17503–17529.
- Campos, J., Hatzfeld, D., Madariaga, R., López, G., Kausel, E., Zollo, A., Iannaccone, G., Fromm, R., Barrientos, S., and Lyon-Caen, H. (2002). A seismological study of the 1835 seismic gap in south-central Chile. *Physics of the Earth and Planetary Interiors*, v. 132, p. 177–195, doi:10.1016/S0031-9201(02)00051-1.
- Carvajal, M., Cisternas, M., Gubler, A., Catalán, P. A., Winckler, P., & Wesson, R. L. (2017a). Reexamination of the magnitudes for the 1906 and 1922 Chilean earthquakes using Japanese tsunami amplitudes: Implications for source depth constraints. *Journal of Geophysical Research: Solid Earth*, 122(1), 4-17.
- Carvajal, M., Cisternas, M., & Catalán, P. A. (2017b). Source of the 1730 Chilean earthquake from historical records: Implications for the future tsunami hazard on

- the coast of Metropolitan Chile. *Journal of Geophysical Research (Solid Earth)*, 122, 3648-3660.
- Castilla, J.C. (1988). Earthquake-caused coastal uplift and its effects on rocky intertidal kelp communities. *Science* 242: 440-443.
- Charrier, R., Baeza, O., Elgueta, S., Flynn, J. J., Gans, P., Kay, S. M., ... & Zurita, E. (2002). Evidence for Cenozoic extensional basin development and tectonic inversion south of the flat-slab segment, southern Central Andes, Chile (33°–36° S). *Journal of South American Earth Sciences*, 15(1), 117-139.
- Christensen, D. H., & Ruff, L. J. (1986). Rupture process of the March 3, 1985 Chilean earthquake. *Geophysical Research Letters*, 13(8), 721-724.
- Cifuentes, I.L. & Silver, P.G. (1989). Low-frequency source characteristics of the great 1960 Chilean earthquake. *Journal of Geophysical Research*, v. 94, p. 643–663, doi:10.1029/JB094iB01p00643.
- Cifuentes, I.L. (1989). The 1960 Chilean earthquake. *Journal of Geophysical Research*, v. 94, p. 665–680.
- Cisternas, M., Torrejón, F., & Gorigoitia, N. (2012). Amending and complicating Chile's seismic catalog with the Santiago earthquake of 7 August 1580. *Journal of South American Earth Sciences*, 33(1), 102-109.
- Cisternas, M., Ely, L., Wesson, R., Pilarczic, J., Gorigoitia, N., Dura, T., Melnick, D., Carvajal, M. (2014). The 1730 and 1751 Chilean earthquakes: two major contributors to the seismically prolific 18th century along the Pacific Coast of the Americas. *In: SSA Annual Meeting, Anchorage, Alaska*.
- Cisternas, M., Garrett, E., Wesson, R., Dura, T., & Ely, L. L. (2017). Unusual geologic evidence of coeval seismic shaking and tsunamis shows variability in earthquake size and recurrence in the area of the giant 1960 Chile earthquake. *Marine Geology*, 385, 101-113.
- Collot, J.-Y., Marcaillou, B., Sage, F., Michaud, F., Agudelo, W., Charvis, P., Graindorge, D., Gutscher, M.A., Spence, G. (2004). Are rupture zone limits of great subduction earthquakes controlled by upper plate structures? Evidence

- from multichannel seismic reflection data acquired across the northern Ecuador southwest Colombia margin. *J. Geophys. Res. Solid Earth* (1978- 2012) 109.
- Comte, D., Eisenberg, A., Lorca, E., Pardo, M., Ponce, L., Saragoni, R., Singh, S., and Suárez, G. (1986). The 1985 central Chile earthquake, a repeat of previous earthquakes in the region? *Science*, v. 233, p. 449–453.
- Comte, D., Suárez, G. (1994). An inverted double seismic zone in Chile: Evidence of phase transformation in the subducted slab. *Science*, Vol. 263, 5144, p. 212-215.
- Comte, D., Farias, M., Roecker, S., & Russo, R. (2019). The nature of the subduction wedge in an erosive margin: Insights from the analysis of aftershocks of the 2015 Mw 8.3 Illapel earthquake beneath the Chilean Coastal Range. *Earth and Planetary Science Letters*, 520, 50–62. doi:10.1016/j.epsl.2019.05.033
- Conca, J. L., & Cubba, R. (1986). Abrasion resistance hardness testing of rock materials. *International Journal of Rock Mechanics and Mining Sciences & Geomechanics Abstracts*, 23(2), 141–149. doi:10.1016/0148-9062(86)90340-2.
- Conca, J. L., & Rossman, G. R. (1985). Core softening in cavernously weathered tonalite. *The Journal of Geology*, 93(1), 59-73.
- Contreras-Reyes, E., Ruiz, J. A., Becerra, J., Kopp, H., Reichert, C., Maksymowicz, A., & Arriagada, C. (2015). Structure and tectonics of the central Chilean margin (31°–33° S): Implications for subduction erosion and shallow crustal seismicity. *Geophysical Journal International*, 203(2), 776-791.
- Cordani, U., Munizaga, F., Hervé, F., & Hervé, M. (1976). Edades radiométricas provenientes del basamento cristalino de la Cordillera de la Costa de las provincias de Valparaíso y Santiago, Chile. *In Congreso Geológico Chileno, No.1, Actas, 2, F213-F222.*
- Corvalán, J., & Munizaga, F. (1972). Edades radiométricas de rocas intrusivas y metamórficas de la Hoja Valparaíso-San Antonio. *Instituto de Investigaciones Geológicas, Boletín No. 28, 40.*

- Corvalán, J., Hervé, F., & Godoy, E. (1977). Estudio Geológico del área Quintay-Ruta Gallo, Provincia de Valparaíso, V Región. *Empresa Nacional de Electricidad SA/Universidad de Chile, Inédito*, 61.
- Creixell, C., Parada, M.A., Roperch, P., Morata, D., Arriagada, C., Pérez de Arce, C. (2006). Syntectonic emplacement of the Concón Mafic Dike Swarm, Coastal Range, central Chile (33°S). *Tectonophysics*, 425:101–122.
- Creixell, C., Parada, M.A., Morata, D., Roperch, P., Arriagada, C. (2007). The genetic link between mafic dike swarms and plutonic reservoirs in the Mesozoic of central Chile (30°-33°45' S): insights from AMS and geochemistry. *International Journal of Earth Sciences* 98: 177-201.
- Creixell, C., Parada, M.A., Morata, D., Vásquez, P., Pérez de Arce, C., Arriagada, C. (2011). Middle-Late Jurassic to Early Cretaceous transtension and transpression during arc building in Central Chile: evidence from mafic dike swarms. *Andean Geology* 38 (1): 37-63.
- Creveling, J. R., Mitrovica, J. X., Clark, P. U., Waelbroeck, C., & Pico, T. (2017). Predicted bounds on peak global mean sea level during marine isotope stages 5a and 5c. *Quaternary Science Reviews*, 163, 193-208.
- Cruslock, E. M., Naylor, L. A., Foote, Y. L., & Swantesson, J. O. (2010). Geomorphologic equifinality: A comparison between shore platforms in Höga Kusten and Fårö, Sweden and the Vale of Glamorgan, South Wales, UK. *Geomorphology*, 114(1-2), 78-88.
- d'Orbigny, A.L. (1842). Voyage dans l'Amérique méridionale exécuté pendant les années 1826-1833. III: *Partie Géologie*: 187 p. París.
- Darwin, C., Sowerby, G.B., Forbes, E. (1846). Geological Observations on South America. *Smith, Elder and Co., London*.
- Darwin, C. (1851). Geological observations of South America, geological observations on coral reefs, volcanic islands and on South America—*Being the voyage of the Beagle, under the Command of Captain Fitzroy, R.N., during the years 1832 to 1836: London, Smith and Elder, 279 p.*

- Davison, C. (1936). Great Earthquakes. *Murby, London, 286 pp.*
- De Ballore, C. D. M. (1911, January). Historia sísmica de los Andes meridionales (continuación). *In Anales de la Universidad de Chile (pp. ág-1), Vol. 5.*
- De Pascale, G. P., Quigley, M. C., & Davies, T. R. (2014). Lidar reveals uniform Alpine fault offsets and bimodal plate boundary rupture behavior, New Zealand. *Geology, 42(5), 411-414.*
- Decelles, P. G., Ducea, M. N., Kapp, P. & Zandt, G. (2009). Cyclicity in Cordilleran orogenic systems. *Nature Geoscience, 2, 251–257, <http://dx.doi.org/10.1038/NGEO469>.*
- Deckart, K., Hervé Allamand, F., Fanning, M., Ramírez, V., Calderón, M., & Godoy, E. (2014). U-Pb geochronology and Hf-O isotopes of zircons from the Pennsylvanian Coastal Batholith, south-central Chile. *Andean Geology 41 (1): 49-82.*
- Delaney, P.T.; Pollard, D.D.; Ziony, J.; McKee, E.H. (1986). Field relations between dikes and joints: emplacement processes and paleostress analysis. *Journal of Geophysical Research 91: 4920-4938.*
- Delouis, B., Philip, H., Dorbath, L., Cisternas, A. (1998). Recent crustal deformation in the Antofagasta region (northern Chile) and the subduction process. *Geophysical Journal International 132, 302–338.*
- DeMets, C; Gordon, R.G.; Argus, D.F.; Stein, S. (1994). Effect of the recent revisions to the geomagnetic reversal time scale on estimates of current plate motions. *Geophysical Research Letters 21: 2191-2194.*
- Domeyko, I. (1848). Sur le terrain et le lignes d'ancien niveau de l'Océan du Sud, aux environs de Coquimbo (Chili). *Annales des Mines, Paris, Série 14 (4): 153-162.*
- Dragovic, D. (1969). The origin of cavernous surfaces (tafoni) in granitic rocks of southern South Australia. *Zeitschrift für Geomorphologie (NF 13): 163–181.*

- Dupré, W. R. (1984). Reconstruction of paleo-wave conditions during the late Pleistocene from marine terrace deposits, Monterey Bay, California. *Marine Geology*, 60(1-4), 435-454.
- Ehlers, T. A. & Poulsen, C. J. (2009). Influence of Andean uplift on climate and paleo altimetry estimates. *Earth and Planetary Science Letters*, 281, 238–248.
- Encinas, A., Le Roux, J. P., Buatois, L. A., Nielsen, S. N., Finger, K. L., Fourtanier, & Lavenu, A. (2006). Nuevo esquema estratigráfico para los depósitos marinos mio-pliocenos del área de Navidad (33°00' – 34°30' S), Chile central. *Revista Geológica de Chile*, 33, 221–246.
- Encinas, A., Finger, K., Nielsen, S., Lavenu, A., Buatois, L., Peterson, D. & Le Roux, J. P. (2008). Rapid and major coastal subsidence during the late Miocene in south-central Chile. *Journal of South American Earth Sciences*, 25, 157–175.
- Ernst, W.G.; Liu, J. (1998). Experimental phase-equilibrium study of Al- and Ti- contents of calcic amphibole in MORB- A semiquantitative thermobarometer. *American Mineralogist* 83: 952-969.
- Farías, M., (2007). Tectónica y erosión en la evolución del relieve de los Andes de Chile Central durante el Neógeno. *Tesis para optar al grado de Doctor en Ciencias, mención Geología*.
- Farías, M., Charrier, R. et al. (2008). Late Miocene high and rapid surface uplift and its erosional response in the Andes of central Chile (33°–35° S). *Tectonics*, 27, TC1005, <http://dx.doi.org/10.1029/2006TC002046>.
- Farías, M.; Vargas, G.; Tassara, A.; Carretier, S.; Baize, S.; Melnick, D.; Bátorle, K. (2010). Land-Level Changes Produced by the Mw 8.8 2010 Chilean Earthquake. *Science* 329 (5994): 916. DOI: 10.1126/Science.1192094.
- Farías, M., Comte, D., Roecker, S., Carrizo, D., & Pardo, M. (2011). Crustal extensional faulting triggered by the 2010 Chilean earthquake: The Pichilemu Seismic Sequence. *Tectonics*, 30(6).

- Fock, A. 2005. Cronología y tectónica de la exhumación en el Neógeno de los Andes de Chile central entre los 33° y los 34° S. *MSc thesis, Universidad de Chile, Chile.*
- Fuenzalida, H., Cooke, R., Paskoff, R., Segerstrom, K. and Weischet, W. (1965). High stands of Quaternary sea-level along the Chilean coast. *Geological Society of America, Special Paper 84, p. 473-496.*
- Gana, P., Wall, R., Gutiérrez, A., & Yáñez, G. (1994). Geología de la Cordillera de la Costa, Regiones de Valparaíso y Metropolitana, al oeste de los 71°00' W. *In Congreso Geológico Chileno, No. 7, Actas, 1, 43-46.*
- Gana, P.; Tosdal, R. (1996). Geocronología U-Pb y K-Ar en intrusivos del Paleozoico y Mesozoico de la Cordillera de la Costa, Región de Valparaíso, Chile. *Revista Geológica de Chile 23 (2): 151-164.*
- Gana, P., Wall, R., & Gutiérrez, A. (1996). Mapa geológico del área de Valparaíso-Curacaví, Región de Valparaíso y Región Metropolitana. *Servicio Nacional de Geología y Minería (Chile), Mapas Geológicos, N°1, Escala 1:100000, 1 mapa, 1 anexo.*
- Garzzone, C., Hoke, G. et al. (2008). The rise of the Andes. *Science, 320, 1304–1307.*
- Giambiagi, L. & Ramos, V. A. (2002). Structural evolution of the Andes between 33°30' and 33°45' S, above the transition zone between the flat and normal subduction segment, Argentina and Chile. *Journal of South American Earth Sciences, 15, 99–114.*
- Giambiagi, L., Ramos, V. A., Godoy, E., Álvarez, P. P. & Orts, S. (2003a). Cenozoic deformation and tectonic style of the Andes, between 33° and 34° South Latitude. *Tectonics, 22, 1041, <http://dx.doi.org/10.1029/2001TC001354>.*
- Giambiagi, L., Alvarez, P., Godoy, E. & Ramos, V. (2003b). The control of pre-existing extensional structures on the evolution of the southern sector of the Aconcagua fold and thrust belt, southern Andes. *Tectonophysics, 369, 1–19.*

- Giambiagi, L., Mescua, J., Bechis, F., Martinez, A. & Folguera, A. (2011). Pre- Andean deformation of the Precordillera southern sector, southern Central Andes. *Geosphere*, 7, 219–239.
- Giambiagi, L., Mescua, J. et al. (2014a). Reactivation of Paleozoic structures during Cenozoic deformation in the Cordón del Plata and Southern Precordillera ranges (Mendoza, Argentina). *Journal of Iberian Geology*, 40, 309–320.
- Giambiagi, L., Tassara, A., Mescua, J., Tunik, M., Álvarez, P. P., Godoy, E., & Tapia, F. (2015). Evolution of shallow and deep structures along the Maipo–Tunuyán transect (33°40' S): from the Pacific coast to the Andean foreland. *Geological Society, London, Special Publications*, 399(1), 63-82.
- Gill, E. D., Segnit, E. R., and McNeill, N. H. (1981). Rate of formation of honeycomb weathering features (small scale tafoni) on the Otway coast, SE Australia. *Royal Soc. Victoria Proc.*, v. 92, p. 149-154.
- Glazner, A., Bartley, J., Carl, B. (1999). Oblique opening and noncoaxial emplacement of the Jurassic Independence dike swarm, California. *Journal of Structural Geology* 21 (10): 1275-1283.
- Godoy, E., & Loske, W. (1988). Tectonismo sinplutónico de dioritas jurásicas al sur de Valparaíso: datos U-Pb sobre la 'Fase Quintay'. *Revista Geológica de Chile*, 15(2), 119-128.
- Godoy, E., Yáñez, G. & Vera, E. (1999). Inversion of an Oligocene volcano-tectonic basin and uplift of its superimposed Miocene magmatic arc, Chilean Central Andes: first seismic and gravity evidence. *Tectonophysics*, 306, 217–326.
- Godoy, E. (2011). Structural setting and diachronism in the Central Andean Eocene to Miocene volcanotectonic basins. In: *Salfity, J. A. & Marquilla, R. (eds) Cenozoic Geology of the Central Andes of Argentina, SCR Publisher, Salta, Argentina, 155–167.*
- Goff, J., Dudley, W. C., Demaitenon, M. J., Cain, G. K., & Coney, J. P. (2006). The largest local tsunami in 20th century Hawaii. *Marine Geology*, 226(1-2), 65-79.

- Goff, J., Weiss, R., Courtney, C., & Dominey-Howes, D. (2010). Testing the hypothesis for tsunami boulder deposition from suspension. *Marine Geology*, 277(1-4), 73-77.
- González-Alfaro, J., Vargas, G., Ortlieb, L., González, G., Ruiz, S., Báez, J. C., & del Río, I. (2018). Abrupt increase in the coastal uplift and earthquake rate since ~ 40 ka at the northern Chile seismic gap in the Central Andes. *Earth and Planetary Science Letters*, 502, 32-45.
- Goudie, A., Viles, H. (1997) Salt Weathering Hazards. *Chichester: Wiley*.
- Goudie, A. (2003). Encyclopedia of Geomorphology. *Routledge, p.1200. London*.
- Graham, M. (1824). *Trans. Geol. Soc. London (Ser. 2). 1, 413*.
- Grisez, L. (1960). Alvéolisation littorale de schistes métamorphiques. *Rev. Géomorphologie Dynamique*, v. 11, p. 164-167.
- Guerrero, B. (201X, in prep.). Variabilidad en las tasas de alzamiento tectónico de terrazas marinas en Chile Central (33°-34° S) y su relación con rasgos estructurales de la Placa Sudamericana. *Undergraduate thesis in preparation, Departamento de Geología, Universidad de Chile, Chile*.
- Gutiérrez, N., Hinojosa, L., Le Roux, J. P. & Pedroza, V. (2013). Evidence for an Early-Middle Miocene age of the Navidad Formation (central Chile): paleontological, paleoclimatic and tectonic implications. *Andean Geology*, 40, 66–78.
- Hachinohe, S., Hiraki, N., & Suzuki, T. (2000). Rates of weathering and temporal changes in strength of bedrock of marine terraces in Boso Peninsula, Japan. In *Developments in geotechnical engineering (Vol. 84, pp. 171-185)*. Elsevier.
- Hagen, R. A., Vergara, H., & Naar, D. F. (1996). Morphology of San Antonio submarine canyon on the central Chile forearc. *Marine Geology*, 129(3-4), 197-205.
- Hearty, P. J., Hollin, J. T., Neumann, A. C., O'Leary, M. J., & McCulloch, M. (2007). Global sea-level fluctuations during the Last Interglaciation (MIS 5e). *Quaternary Science Reviews*, 26(17-18), 2090-2112.

- Heredia, N., Farías, P., García-Sansegundo, J. & Giambiagi, L. (2012). The basement of the Andean Frontal Cordillera in the Cordon del Plata (Mendoza, Argentina): geodynamic evolution. *Andean Geology*, 39, 242–257.
- Herm, D. (1969). Marines Pliozän und Pleistozän in Nord und Mittel-Chile unter besonderer Berücksichtigung der Entwicklung der Mollusken-Faunen. *Zitteliana 2*: 1-159.
- Hervé, F., Munizaga, F., Parada, M., Brook, M., Pankhurst, R., Snelling, N., & Drake, R. (1988). Granitoids of the Coast Range of Central Chile: Geochronology and geological setting. *Journal of South America Earth Sciences*, 1(2), 185 -194.
- Herve, F., & Ota, Y. (1993). Fast Holocene uplift rates at the Andes of Chiloé, southern Chile. *Andean Geology*, 20(1), 15-23.
- Hervé, F., Faundez, V., Calderón, M., Massonne, H. J., & Willner, A. P. (2007). Metamorphic and plutonic basement complexes. *In The Geology of Chile (pp. 5-19)*.
- Holtkamp, S. G., Pritchard, M. E. & Lohman, R. B. (2011). Earthquake swarms in South America. *Geophysical Journal International*, 187, 128–146.
- Huinink, HP., Pel, L., Kopinga, K. (2004). Simulating the growth of tafoni. *Earth Surface Processes and Landforms* 29(10): 1225–1233.
- Isacks, B. (1988). Uplift of the Central Andean plateau and bending of the Bolivian Orocline. *Journal of Geophysical Research*, 93, 3211–3231.
- Jara-Muñoz, J. & Melnick, D. (2015). Unraveling sea-level variations and tectonic uplift in wave-built marine terraces, Santa María Island, Chile. *Quaternary research*, 83(1), 216-228.
- Jara-Munoz, J., Melnick, D., Brill, D., & Strecker, M. R. (2015). Segmentation of the 2010 Maule Chile earthquake rupture from a joint analysis of uplifted marine terraces and seismic-cycle deformation patterns. *Quaternary Science Reviews*, 113, 171-192.

- Johansen, H.W. (1971). Effects of elevation changes in benthic algae in Prince William Sound. In *The Great Alaska Earthquake of 1964. National Academy of Sciences: 35-68. Washington D.C.*
- Kaizuka, S. (2015). Quaternary tectonic and recent seismic crustal movements in the Arauco Peninsula and its environs, central Chile. *Geographical Reports Tokyo Metropolitan University, v. 8, p. 1–49.*
- Kelleher, J.A. (1972). Rupture zones of large South American earthquakes and some predictions. *Journal of Geophysical Research, v. 77, p. 2089–2103.*
- Khazaradze, G., & Klotz, J. (2003). Short-and long-term effects of GPS measured crustal deformation rates along the south central Andes. *Journal of Geophysical Research: Solid Earth, 108(B6).*
- Klotz, J., Khazaradze, G., Angermann, D., Reigber, C., Perdomo, R., & Cifuentes, O. (2001). Earthquake cycle dominates contemporary crustal deformation in Central and Southern Andes. *Earth and Planetary Science Letters, 193(3-4), 437-446.*
- Koper, K. D., Hutko, A. R., Lay, T., Ammon, C. J., & Kanamori, H. (2011). Frequency-dependent rupture process of the 2011 M w 9.0 Tohoku Earthquake: Comparison of short-period P wave backprojection images and broadband seismic rupture models. *Earth, planets and space, 63(7), 16.*
- Lajoie, K. R. (1986). Coastal tectonics. In *Wallace, R. E., ed., Active tectonics: Washington, D.C., National Academy Press, p. 95-124.*
- Lamb, S., & Davis, P. (2003). Cenozoic climate change as a possible cause for the rise of the Andes. *Nature, 425(6960), 792.*
- Lambeck, K., Esat, T. M., & Potter, E. K. (2002). Links between climate and sea levels for the past three million years. *Nature, 419(6903), 199.*
- Laursen, J., & Normark, W. R. (2002). Late Quaternary evolution of the San Antonio Submarine Canyon in the central Chile forearc (~ 33°S). *Marine Geology, 188(3-4), 365-390.*

- Laursen, J., Scholl, D. W., & von Huene, R. (2002). Neotectonic deformation of the central Chile margin: Deepwater forearc basin formation in response to hot spot ridge and seamount subduction. *Tectonics*, 21(5), 2-1.
- Lavenu, A., & Cembrano, J. (1999). Compressional-and transpressional-stress pattern for Pliocene and Quaternary brittle deformation in fore arc and intra-arc zones (Andes of Central and Southern Chile). *Journal of Structural Geology*, 21(12), 1669-1691.
- Lavenu, A. & Encinas, A. (2005). Brittle deformation of the Neogene deposits of the Navidad Basin (Coastal Cordillera, 34° S, central Chile). *Revista Geológica de Chile*, 32, 229–248.
- Lay, T., Ammon, C. J., Kanamori, H., Xue, L., & Kim, M. J. (2011). Possible large near-trench slip during the 2011 M w 9.0 off the Pacific coast of Tohoku Earthquake. *Earth, planets and space*, 63(7), 32.
- Lebednik, P.A. (1973). Ecological effects of intertidal uplifting from nuclear testing. *Marine Biology* 20: 197-207.
- Leonard, E. & Wehmiller, J. (1991). Geochronology of marine terraces at Caleta Michilla, northern Chile; implications for Late Pleistocene and Holocene uplift. *Revista Geológica de Chile*, 18 (1): 81-86.
- Leonard, E.M.; Wehmiller, J.F. (1992). Low uplift rates and terrace reoccupation inferred from mollusk aminostratigraphy, Coquimbo bay, Chile. *Quaternary Research* 38: 246-259.
- Leyton, F., Ruiz, S., Sepúlveda, S. (2010). Reevaluación del peligro sísmico probabilístico en Chile central. *Andean Geology*, 37 (2), 455-472.
- Limber, P. W., & Murray, A. B. (2011). Beach and sea-cliff dynamics as a driver of long-term rocky coastline evolution and stability. *Geology*, 39(12), 1147-1150.
- Lin, Y. N. N., Sladen, A., Ortega-Culaciati, F., Simons, M., Avouac, J. P., Fielding, E. J., ... & Vigny, C. (2013). Coseismic and postseismic slip associated with the 2010 Maule Earthquake, Chile: Characterizing the Arauco Peninsula barrier effect. *Journal of Geophysical Research: Solid Earth*, 118(6), 3142-3159.

- Lomnitz, C. (1970). Major earthquakes and tsunamis in Chile during the period 1535 to 1955. *Geologische Rundschau*, v. 59, p. 938–960, doi: 10.1007/BF02042278.
- Lomnitz, C. (2004). Major earthquakes of Chile: A historical survey, 1535–1960. *Seismological Research Letters*, v. 75, p. 368–378.
- Marquardt, C., Lavenu, A., Ortlieb, L., Godoy, E., & Comte, D. (2004). Coastal neotectonics in Southern Central Andes: uplift and deformation of marine terraces in Northern Chile (27° S). *Tectonophysics*, 394(3-4), 193-219.
- Martini, I. (1978). Tafoni Weathering, with Examples from Tuscany, Italy. *Zeitschrift fuer Geomorphologie*, v. 22, p. 44-67.
- Martinod, J., Regard, V., Riquelme, R., Aguilar, G., Guillaume, B., Carretier, S., & Hérail, G. (2016). Pleistocene uplift, climate and morphological segmentation of the Northern Chile coasts (24°S–32°S): Insights from cosmogenic ¹⁰Be dating of paleoshorelines. *Geomorphology*, 274, 78-91.
- Matsukura Y, Matsuoka N. (1991). Rates of tafoni weathering on uplifted shore platforms in Nojima-Zaki, Boso Peninsula, Japan. *Earth Surface Processes and Landforms* 16(1): 51–56.
- McCaan, W., Nishenko, S., Skyes, L., Krause, J. (1979). Seismic gaps and plate tectonics: seismic potential for major boundaries. *Pure and Applied Geophysics*, 117, 1082-1147.
- McGreevy, J.P. (1985). A preliminary Scanning Electron Microscope study of honeycomb weathering of sandstone in a coastal environment. *Earth Surface Processes and Landforms* 10, 509–518.
- Mellor, A., Short, J., Kirkby, S.J. (1997). Tafoni in the El Chorro area, Andalucía, southern Spain. *Earth Surface Processes and Landforms* 22(9): 817–833.
- Melnick, D., Bookhagen, B., Echtler, H. P., & Strecker, M. R. (2006). Coastal deformation and great subduction earthquakes, Isla Santa María, Chile (37°S). *Geological Society of America Bulletin*, 118(11-12), 1463-1480.

- Melnick, D., Bookhagen, B., Strecker, M. R., & Echtler, H. P. (2009). Segmentation of megathrust rupture zones from fore-arc deformation patterns over hundreds to millions of years, Arauco peninsula, Chile. *Journal of Geophysical Research: Solid Earth*, 114(B1).
- Melnick, D., Cisternas, M., Moreno, M., Norambuena, R. (2012a). Estimating coseismic coastal uplift with an intertidal mussel: calibration for the 2010 Maule Chile earthquake (Mw 8.8). *Quat. Sci. Rev.* 42, 29e42.
- Melnick, D. (2016). Rise of the central Andean coast by earthquakes straddling the Moho. *Nature Geoscience*, 9(5), 401.
- Melnick, D., Moreno, M., Quinteros, J., Baez, J. C., Deng, Z., Li, S., & Oncken, O. (2017). The super-interseismic phase of the megathrust earthquake cycle in Chile. *Geophysical Research Letters*, 44(2), 784-791.
- Merrill, G.P. (1906). A treatise on rocks, rock-weathering, and soils. *Macmillan, New York*.
- Mesolella, K.J., Matthews, R.K., Broecker, W.S., Thurber, D.L. (1969). The astronomical theory of climatic change: Barbados data. *J. Geol.* 77, 250e274.
- Moernaut, J., Van Daele, M., Heirman, K., Fontijn, K., Strasser, M., Pino, M., ... & De Batist, M. (2014). Lacustrine turbidites as a tool for quantitative earthquake reconstruction: New evidence for a variable rupture mode in south central Chile. *Journal of Geophysical Research: Solid Earth*, 119(3), 1607-1633.
- Montgomery, D. R., Balco, G., & Willett, S. D. (2001). Climate, tectonics, and the morphology of the Andes. *Geology*, 29(7), 579-582.
- Moreno, M. S., Klotz, J., Melnick, D., Echtler, H., & Bataille, K. (2008). Active faulting and heterogeneous deformation across a megathrust segment boundary from GPS data, south central Chile (36–39°S). *Geochemistry, Geophysics, Geosystems*, 9(12).
- Moreno, M. S., Bolte, J., Klotz, J., & Melnick, D. (2009). Impact of megathrust geometry on inversion of coseismic slip from geodetic data: Application to the 1960 Chile earthquake. *Geophysical Research Letters*, 36(16).

- Moreno, M., Melnick, D., Rosenau, M., Baez, J., Klotz, J., Oncken, O., Tassara, A., Chen, J., Bataille, K., Bevis, M., Socquet, A., Bolte, J., Vigny, C., Brooks, B., Ryder, I., Grund, V., Smalley, B., Carrizo, D., Bartsch, M., Hase, H. (2012). Toward understanding tectonic control on the Mw 8.8 2010 Maule Chile earthquake. *Earth and Planetary Science Letters*, 321, 152–165. <https://doi.org/10.1016/j.epsl.2012.01.006>.
- Mottershead, D. N. (1989). Rates and patterns of bedrock denudation by coastal salt spray weathering: A seven-year record. *Earth Surface Processes and Landforms*, 14(5), 383–398.
- Mottershead, D.N. and Pye, K. (1994). Tafoni on coastal slopes, south Devon, U.K. *Earth Surface Processes and Landforms* 19, 543–563.
- Mpodozis, C., and Ramos, V. (1989). The Andes of Chile and Argentina. In *Ericksen, G.E., Cañas Pinochet, M.T., and Reinemund, J.A., eds., Geology of the Andes and its relation to hydrocarbon and mineral resources: Houston, Texas, Circum-Pacific Council for Energy and Mineral Resources*, p. 59–90.
- Muhs, D. R., Kelsey, H. M., Miller, G. H., Kennedy, G. L., Whelan, J. F., & McInelly, G. W. (1990). Age estimates and uplift rates for late Pleistocene marine terraces: Southern Oregon portion of the Cascadia forearc. *Journal of Geophysical Research: Solid Earth*, 95(B5), 6685-6698.
- Mustoe, G. E. (1982). The origin of honeycomb weathering. *Geol. Soc. America Bull.*, v. 93, p. 108-115.
- Mustoe GE. (1983). Cavernous weathering in the Capitol Reef Desert, Utah. *Earth Surface Processes and Landforms* 8(6): 517–526.
- Nanayama, F., Satake, K., Furukawa, R., Shimokawa, K., Atwater, B.F., Shigeno, K., Yamaki, S. (2003). Unusually large earthquakes inferred from tsunami deposits along the Kuril trench. *Nature* 424, 660-663.
- Nelson, A. R., & Manley, W. F. (1992). Holocene coseismic and aseismic uplift of Isla Mocha, south-central Chile. *Quaternary International*, 15-16, 61–76. doi:10.1016/1040-6182(92)90036-2

- Nishenko, S. (1985). Seismic potential for large and great interplate earthquakes along the Chilean and southern Peruvian margins of South America: a quantitative reappraisal. *Journal of Geophysical Research*, 90, 3589-3615.
- Norwick, S., Dexter, L. (2002). Rates of development of tafoni in the Moenkopi and Kaibab formations in Meteor Crater and on the Colorado Plateau, northeastern Arizona. *Earth Surface Processes and Landforms* 27(1): 11–26.
- Oguchi, C. T.; Hatta, T.; and Matsukura, Y. (1994). Changes in rock properties of porous rhyolite through 40,000 years in Kozushima, Japan. *Geog. Rev. Japan*, v. 67A, p. 775-793 (in Japanese with English abstract).
- Okal, E. A. (2005). A re-evaluation of the great Aleutian and Chilean earthquakes of 1906 August 17. *Geophysical Journal International*, 161(2), 268-282.
- Ortlieb, L.; Zazo, C.; Goy, J.; Hillaire-Marcel, C.; Ghaleb, B.; Cournoyers, L. (1996a). Coastal Deformation and Sea-Level Changes in the Northern Chile Subduction Area (23°S) during the last 330 Ky. *Quaternary Science Reviews* 15: 819-831.
- Ortlieb, L., Barrientos, S., & Guzman, N. (1996b). Coseismic coastal uplift and coralline algae record in northern Chile: the 1995 Antofagasta earthquake case. *Quaternary Science Reviews*, 15(8-9), 949-960.
- Ota, Y., & Paskoff, R. (1993). Holocene deposits on the coast of north-central Chile: radiocarbon ages and implications for coastal changes. *Andean Geology*, 20(1), 25-32.
- Ota, Y., Miyauchi, T., Paskoff, R., Koba, M. (1995). Plio-Quaternary marine terraces and their deformation along the Altos de Talinay, north-central Chile. *Revista Geológica de Chile* 22 (1): 89-102
- Otten, M. (1984). The origin of brown hornblende in the Artfjället gabbro and dolerites. *Contributions to Mineralogy and Petrology* 86 (2): 189-199.
- Ozawa, S., Nishimura, T., Munekane, H., Suito, H., Kobayashi, T., Tobita, M., & Imakiire, T. (2012). Preceding, coseismic, and postseismic slips of the 2011 Tohoku earthquake, Japan. *Journal of Geophysical Research: Solid Earth*, 117(B7).

- Parada, M. A., Nyström, J. O., & Levi, B. (1999). Multiple sources for the Coastal Batholith of central Chile (31–34° S): geochemical and Sr–Nd isotopic evidence and tectonic implications. *Lithos*, 46(3), 505-521.
- Paskoff, R. (1970). Recherches géomorphologiques dans le Chili semi-aride. *Biscaye Frères 420 p. Bordeaux.*
- Paskoff, R. (1977). Quaternary of Chile: the state of research. *Quaternary Research* 8: 2-31.
- Paskoff, R. (2005). Faulted Coasts. (M. Schwartz, Ed.) *Encyclopedia of Coastal Science, Encyclopedia of Earth Science Series*, 463-466.
- Pedoja, K., Husson, L., Regard, V., Cobbold, P. R., Ostanciaux, E., Johnson, M. E., ... & Weill, P. (2011). Relative sea-level fall since the last interglacial stage: are coasts uplifting worldwide?. *Earth-Science Reviews*, 108(1-2), 1-15.
- Perfettini, H., Avouac, J.-P., Tavera, H., Kositsky, A., Nocquet, J.-M., Bondoux, F., Chlieh, M., Sladen, A., Audin, L., Farber, D.L. (2010). Seismic and aseismic slip on the central Peru megathrust. *Nature* 465, 78-81.
- Perrey, A. (1854). Documents relatifs aux tremblements de terre au Chili. *Ann. Soc. Imper. d'Agric. Barret, Lyon.*
- Pilger, R. H. (1981). Plate reconstructions, aseismic ridges, and low-angle subduction beneath the Andes. *Geological Society of America Bulletin*, 92(7), 448-456.
- Pilger, R. H. (1984). Cenozoic plate kinematics, subduction and magmatism: South American Andes. *Journal of the Geological Society*, 141(5), 793-802.
- Piracés, R., & MaksaeV, V. (1977). Geología de la Hoja Quillota, IV y V Región. *Instituto de Investigaciones Geológicas (Informe Registrado No. 1406)*, 135, 1 mapa 1:250.000.
- Plafker, G. (1964). Tectonic deformation associated with the 1964 Alaskan earthquake. *Science* 148: 1675 p.

- Plafker, G., & Savage, J. C. (1970). Mechanism of the Chilean earthquakes of May 21 and 22, 1960. *Geological Society of America Bulletin*, 81(4), 1001-1030.
- Polanski, J. (1964). Descripción geológica de la Hoja 25 a-b - Volcán de San José, provincia de Mendoza. *Dirección Nacional de Geología y Minería, Boletín 98*, 1-92, Buenos Aires, Argentina.
- Potter, E.-K., Esat, T.M., Schellmann, G., Radtke, U., Lambeck, K., McCulloch, M.T. (2004). Suborbital-period sea-level oscillations during marine isotope substages 5a and 5c. *Earth Planet. Sci. Lett.* 225, 191-204.
- Rabassa, J., and Clapperton, C.M. (1990). Quaternary glaciations of the southern Andes. *Quaternary Science Reviews*, v. 9, p. 153-174, doi: 10.1016/0277-3791(90)90016-4.
- Ramos, V. (1988). The tectonics of the Central Andes: 30°-33° S latitude. In: Clark, S. & Burchfiel, D. (eds) *Processes in Continental Lithospheric Deformation. Geological Society of America, Boulder, Special Paper, 218*, 31-54, <http://dx.doi.org/10.1130/SPE218-p31>.
- Ramos, V. A., Cristallini, E. O., & Pérez, D. J. (2002). The Pampean flat-slab of the Central Andes. *Journal of South American earth sciences*, 15(1), 59-78.
- Rauld, R., Vargas, G., Armijo, R., Ormeño, A., Valderas, C. & Campos, J. (2006). Cuantificación de escarpes de falla y deformación reciente en el frente cordillerano de Santiago. In: *Proceedings of the XI Congreso Geológico Chileno, Antofagasta, Chile*, 447-450.
- Regard, V., Saillard, M., Martinod, J., Audin, L., Carretier, S., Pedoja, K., Riquelme, R., Paredes, P., Hérail, G. (2010). Renewed uplift of the Central Andes Forearc revealed by coastal evolution during the Quaternary. *Earth and Planetary Science Letters* 297, 199-210.
- Rivano, S., Sepúlveda, P., Boric, R., & Espiñeira, D. (1993). Hojas Quillota y Portillo, escala 1:250.000. *Carta Geológica de Chile SERNAGEOMIN*.
- Rivera, O., & Cembrano, J. (2000). Modelo de formación de cuencas volcano-tectónicas en zonas de transferencia oblicuas a la cadena andina: el caso de las cuencas

oligo-miocénicas de Chile central y su relación con estructuras NWW-NW (33°00'-34°30'S). *In Congreso Geológico Chileno (No. 9, pp. 631-636).*

Rodríguez Montecinos, M. P. (2008). Evolución de la Erosión y del Relieve del Antearco de Chile Central (33-34°S) Durante el Neógeno Mediante el Análisis de Minerales Pesados Detríticos y la Geomorfología. *Disponible en <http://repositorio.uchile.cl/handle/2250/101921>*

Rodríguez, M. P., Pinto Lincoñir, L. & Encinas, A. (2012). Cenozoic erosion in the Andean forearc in Central Chile (33°–34°S): sediment provenance inferred by heavy mineral studies. *In: Rasbury, E. T., Hemming, S. R. & Riggs, N. R. (eds) Mineralogical and Geochemical Approaches to Provenance. Geological Society of America, Boulder, Special Paper, 487, 141–162.*

Rodríguez, M. P., Carretier, S., Charrier, R., Saillard, M., Regard, V., Hérail, G. & Audin, L. (2013). Geochronology of pediments and marine terraces in north-central Chile and their implications for Quaternary uplift in the Western Andes. *Geomorphology, 180, 33-46.*

Rodríguez, M. P. (2014). Neogene landscape evolution in the Andes of north-central Chile between 28 and 32°S: interplay between tectonic and erosional processes. *Geodynamic Processes in the Andes of Central Chile and Argentina. Geological Society, London, Special Publications, 399, <http://dx.doi.org/10.1144/SP399.15>*

Rohling, E., Grant, K., Bolshaw, M., Roberts, A., Siddall, M., Hemleben, C., Kucera, M. (2009). Antarctic temperature and global sea level closely coupled over the past five glacial cycles. *Nat. Geosci. 2, 500e504.*

Roqué, C., Zarroca, M., & Linares, R. (2013). Subsurface initiation of tafoni in granite terrains—geophysical evidence from NE Spain: geomorphological implications. *Geomorphology, 196, 94-105.*

Rosenbloom, N. A., & Anderson, R. S. (1994). Hillslope and channel evolution in a marine terraced landscape, Santa Cruz, California. *Journal of Geophysical Research: Solid Earth, 99(B7), 14013-14029.*

- Ruegg, J.C; Rudloff, A.; Vigny, C; Madariaga, R.; de Chabaliera, J.B.; Campos, J.; Kausel, E.; Barrientos, S.; Dimitrov, D. (2009). Interseismic strain accumulation measured by GPS in the seismic gap between Constitución and Concepción in Chile. *Physics of the Earth and Planetary Interiors*, 175(1-2), 78-85.
- Ruiz, S.; Saragoni, G.R. (2005a). Fórmulas de atenuación para la subducción de Chile considerando los dos mecanismos principales de sismogénesis y los efectos del suelo. *In Jornadas Chilenas de Sismología e Ingeniería Antisísmica, No. 9. Concepción, Chile.*
- Saillard, M. (2008). Dynamique du soulèvement côtier Pléistocène des Andes centrales: Étude de l'évolution géomorphologique et datations (^{10}Be) de séquences de terrasses marines (Sud Pérou-Nord Chili). *Ph.D Thesis, Université de Toulouse, Toulouse, 308 p.*
- Saillard, M., Hall, S. R., Audin, L., Farber, D. L., Hérail, G., Martinod, J., ... & Bondoux, F. (2009). Non-steady long-term uplift rates and Pleistocene marine terrace development along the Andean margin of Chile (31°S) inferred from ^{10}Be dating. *Earth and Planetary Science Letters*, 277(1-2), 50-63.
- Saillard, M., Riotte, J., Regard, V., Violette, A., Hérail, G., Audin, L., & Riquelme, R. (2012). Beach ridges U–Th dating in Tongoy bay and tectonic implications for a peninsula–bay system, Chile. *Journal of South American Earth Sciences*, 40, 77-84.
- Saillard, M., Audin, L., Rousset, B., Avouac, J. P., Chlieh, M., Hall, S. R., ... & Farber, D. L. (2017). From the seismic cycle to long-term deformation: linking seismic coupling and Quaternary coastal geomorphology along the Andean megathrust. *Tectonics*, 36(2), 241-256.
- Saragoni, G.R.; Astroza, M.; Ruiz, S. (2004). Comparative study of subduction earthquake ground motion of north, central and south America. *In Proceedings of the thirteenth World Conference on Earthquake Engineering, Paper 104. Vancouver, Canada.*

- Satake, K., Fujii, Y., Harada, T., & Namegaya, Y. (2013). Time and space distribution of coseismic slip of the 2011 Tohoku earthquake as inferred from tsunami waveform data. *Bulletin of the seismological society of America*, 103(2B), 1473-1492.
- Scott, A. T., & Pinter, N. (2003). Extraction of coastal terraces and shoreline-angle elevations from digital terrain models, Santa Cruz and Anacapa Islands, California. *Physical Geography*, 24(4), 271-294.
- Seivers, A. (1963), The seismic sea wave of 22 May 1960 along the Chilean Coast. *Bull. Seismol. Soc. Am.*, 53, 1125– 1190.
- Sellés, D. & Gana, P. (2001). Geología del área Talagante-San Francisco de Mostazal: Regiones Metropolitana y del Libertador General Bernardo O'Higgins. 1:100000. *SERNAGEOMIN, Carga Geológica de Chile, Serie Geológica Básica*.
- Sepúlveda, S. A., Giambiagi, L. B., Moreiras, S. M., Pinto, L., Tunik, M., Hoke, G. D. & Farías, M. (eds). (2015). Geodynamic Processes in the Andes of Central Chile and Argentina. *Geological Society, London, Special Publications*, 399, 1–12.
- Shackleton, N. J., Sánchez-Goñi, M. F., Paillet, D., & Lancelot, Y. (2003). Marine isotope substage 5e and the Eemian interglacial. *Global and Planetary change*, 36(3), 151-155.
- Sheffels, B. (1990). Lower bound on the amount of crustal shortening in the Central Bolivian Andes. *Geology*, 18, 812–815.
- Shennan, I., Bruhn, R., Plafker, G. (2009). Multi-segment earthquakes and tsunami potential of the Aleutian megathrust. *Quat. Sci. Rev.* 28, 7-13.
- Shennan, I., Garrett, E., & Barlow, N. (2016). Detection limits of tidal-wetland sequences to identify variable rupture modes of megathrust earthquakes. *Quaternary Science Reviews*, 150, 1-30.
- Siña, A. (1987). Geología y petrogénesis de rocas plutónicas del Batolito de la Costa entre Algarrobo y Rocas de Santo Domingo (Chile Central, 33° 30' S), Región de Valparaíso. *Tesis, Dpto. de Geología y Geofísica, U. de Chile*, 139p. *Santiago, Chile*.

- Smith, B.J. and McAlister, J.J. (1986). Observations on the occurrence and origins of salt weathering phenomena near Lake Magadi, Southern Kenya. *Zeitschrift für Geomorphologie NF* 30, 445–460.
- Soloviev, S.L. & Go, Ch.N. (1975). Catalogue of Tsunamis on the Eastern shore of the Pacific Ocean (1513-1968). *Nauka, Moscow. (Can. Transl. Fish. Aquat. Sci. 5078)*.
- Somoza, R. (1998). Updated Nazca (Farallon)–South American relative motions during the last 40 My: Implications for mountain building in the Andes. *Journal of South American Earth Sciences*, v. 11, p. 211–215, doi: 10.1016/S0895-9811(98)00012-1.
- Steffen, H. (1907). Contribuciones para un estudio científico del terremoto del 16 de agosto de 1906. *Imprenta Cervantes*.
- Stephenson, W. J., & Kirk, R. M. (2000). Development of shore platforms on Kaikoura Peninsula, South Island, New Zealand: Part one: the role of waves. *Geomorphology*, 32(1-2), 21-41.
- Strecker, M. R., Alonso, R. N., Bookhagen, B., Carrapa, B., Hilley, G. E., Sobel, E. R., & Trauth, M. H. (2007). Tectonics and climate of the southern central Andes. *Annu. Rev. Earth Planet. Sci.*, 35, 747-787.
- Subarya, C., Chlieh, M., Prawirodirdjo, L., Avouac, J.-P., Bock, Y., Sieh, K., Meltzner, A.J., Natawidjaja, D.H., McCaffrey, R. (2006). Plate-boundary deformation associated with the great Sumatra-Andaman earthquake. *Nature* 440, 46-51.
- Sunamura T. (1996). A physical model for the rate of coastal tafoni development. *Journal of Geology* 104(6): 741–748.
- Takahashi, K. (1975). Differential erosion originating washboard-like relief on wave-cut bench at Aoshima Island, Kyushu, Japan. *Geog. Rev. Japan*, v. 48, p. 43-62.
- Tapia, F., Farías, M. & Astaburuaga, D. (2012). Deformación cretácica-paleocena y sus evidencias en la cordillera de los Andes de Chile Central (33.7–36°S). *XI Congreso Geológico Chileno, Antofagasta, Chile*, 232–234.

- Tavera, J. (1979). Estratigrafía y paleontología de la Formación Navidad, Provincia de Colchagua, Chile (Lat. 30°50' – 34°S). *Museo Nacional de Historia Natural, Boletín N°36*. 176 p. Chile.
- Taylor, F.W., Briggs, R.W., Frohlich, C., Brown, A., Hornbach, M., Papabatu, A.K., Meltzner, A.J., Billy, D. (2008). Rupture across arc segment and plate boundaries in the 1 April 2007 Solomons earthquake. *Nat. Geosci.* 1, 253-257.
- Tebbens, S.F. & Cande, S.C. (1997). Southeast Pacific tectonic evolution from early Oligocene to present. *Journal of Geophysical Research*, v. 102, p. 12,061–12,084, doi: 10.1029/96JB02582.
- Thiele, R., & Morel, R. (1981). Tectónica triásico-jurásica en la cordillera de la costa, al norte y sur del río Mataquito (34°45'-35°15' lat. S), Chile. *Revista geológica de Chile: An international journal on andean geology*, (13), 49-61.
- Thomas, H. (1958). Geología de la Cordillera de la Costa entre el valle de La Ligua y la Cuesta de Barriga. *Instituto de Investigaciones Geológicas, Boletín, No. 2*, 86.
- Trenhaile, A. S. (2002). Modeling the development of marine terraces on tectonically mobile rock coasts. *Marine Geology*, 185(3-4), 341-361.
- Tuckett, F. (1884). Notes on Corsica. *Alpine Journal* 11: 449–459.
- Twidale, CBJ. (1976). The shaping and interpretation of large residual granite boulders. *Journal of Geological Society of Australia* 23 (4): 371–381.
- Udías, A., Madariaga, R., Buforn, E., Muñoz, D., Ros, M. (2012). The large Chilean historical earthquakes of 1647, 1657, 1730, and 1751 from contemporary documents. *Bull. Seismol. Soc. Am.* 102, 1639-1653.
- Vargas, G., Farías, M., Carretier, S., Tassara, A., Baize, S., & Melnick, D. (2011b). Coastal uplift and tsunami effects associated to the 2010 Mw8.8 Maule earthquake in Central Chile. *Andean Geology*, 38(1), 219-238.
- Vicuña Mackenna, B. (1877). Ensayo histórico sobre el clima de Chile: (desde los tiempos prehistóricos hasta el gran temporal de julio de 1877). *Imprenta del Mercurio*, p. 254.

- Vigny, C., Rudloff, A., Ruegg, J. C., Madariaga, R., Campos, J., & Alvarez, M. (2009). Upper plate deformation measured by GPS in the Coquimbo Gap, Chile. *Physics of the Earth and Planetary Interiors*, 175(1-2), 86-95.
- Vigny, C., Socquet, A., Peyrat, S., Ruegg, J.-C., Metois, M., Madariaga, R., Morvan, S., Lancieri, M., Lacassin, R., Campos, J., Carrizo, D., Bejar-Pizarro, M., Barrientos, S., Armijo, R., Aranda, C., Valderas-Bermejo, M.-C., Ortega, I., Boundoux, F., Baize, S., Lyon-Caen, H., Pavez, A., Vilotte, P., Bevis, M., Brooks, B., Smalley, R., Parra, H., Baez, J.-C., Blanco, M., Cimbaro, S., Kendrick, E. (2011). The 2010 M_w 8.8 Maule megathrust earthquake of central Chile, monitored by GPS. *Science* 332 (6036), 1417–1421. <http://doi.org/10.1126/science.1204132>.
- Viles, H., and Goudie, A. (1992). Weathering of limestone columns from the Weymouth seafront, England. *Proc. 7th Int. Cong. Deterioration and Conservation of Stone, Laboratorio Nacional de Engenharia Civil, Lisbon, v. 1, p. 297-304.*
- Wall, R., Gana, P., Gutiérrez, A. (1996). Mapa geológico del área de San Antonio-Melipilla, Regiones de Valparaíso, Metropolitana y del Libertador General Bernardo O'Higgins. *Servicio Nacional de Geología y Minería (Chile), Mapas geológicos, N°2, Escala 1:100.000, 1 mapa, 1 anexo.*
- Wang, K. (2007). Elastic and viscoelastic models of crustal deformation in subduction earthquake cycles. *Seismogenic Zone Subduction Thrust Faults* 540-575.
- Webber, J. R., Klepeis, K. A., Webb, L. E., Cembrano, J., Morata, D., Mora-Klepeis, G., & Arancibia, G. (2015). Deformation and magma transport in a crystallizing plutonic complex, Coastal Batholith, central Chile. *Geosphere*, 11(5), 1401-1426.
- Wellman, H., Wilson, A. (1965). Salt weathering a neglected geological erosive agent in coastal and arid environments. *Nature* 205 (4976): 1097–1098.
- Wesson, R., Melnick, M., Cisternas, M., Moreno, M., Ely, L. (2015). Vertical deformation through a complete seismic cycle at Isla Santa María, Chile. *Nat. Geosci.* 8, 547–551. <https://doi.org/10.1038/ngeo2468>.

- Xue-Ze, W. (2001). Earthquake behavior of variable rupture-scale on active faults and application of the cascade-rupturing model [J]. *Acta Seismologica Sinica*, 14(4), 404-416.
- Yáñez, G.; Gana, P.; Fernández, R. (1998). Origen y significado geológico de la Anomalía Melipilla, Chile central. *Revista Geológica de Chile* 25 (2): 175-198.
- Yáñez, G. A., Ranero, C. R., von Huene, R., & Díaz, J. (2001). Magnetic anomaly interpretation across the southern central Andes (32–34°S): The role of the Juan Fernández Ridge in the late Tertiary evolution of the margin. *Journal of Geophysical Research: Solid Earth*, 106(B4), 6325-6345.
- Yáñez, G., Cembrano, J., Pardo, M., Ranero, C. & Selles, D. (2002). The Challenger-Juan Fernández- Maipo major tectonic transition of the Nazca – Andean subduction system at 33–34°S: geodynamic evidence and implications. *Journal of South American Earth Sciences*, 15, 23–38.
- Yildirim, C., Melnick, D., Ballato, P., Schildgen, T. F., Echtler, H., Erginal, A. E., ... & Strecker, M. R. (2013). Differential uplift along the northern margin of the Central Anatolian Plateau: inferences from marine terraces. *Quaternary Science Reviews*, 81, 12-28.
- Zegers, L. L. (1906, January). El terremoto del 16 de agosto. *In Anales de la Universidad de Chile* (pp. ág-1).

6 ANNEXES

ANNEX 1

Summary table for Table 4 showing different measured coseismic uplift values depending on the seismic events magnitudes. References for each measurement are shown in that same table. This data was used for the graph shown in Figure 61.

	Earthquake	Event Magnitude	Coseismic uplift (m)
2007	Tocopilla	7,7	0,34
1985	Valparaíso	8	0,4
1985	Valparaíso	8	0,5
1985	Valparaíso	8	0,33
1985	Valparaíso	8	0,23
1985	Valparaíso	8	0,28
1995	Antofagasta	8,1	0,8
1995	Antofagasta	8,1	0,15
1906	Valparaíso	8,2	0,6
1822	Valparaíso	8,5	1
1835	Arauco	8,5	1,5
1877	Antofagasta	8,8	1,2
2010	Maule	8,8	1,1
2010	Maule	8,8	1,3
2010	Maule	8,8	1,5
2010	Maule	8,8	2
2010	Maule	8,8	2,6
2010	Maule	8,8	2,4
2010	Maule	8,8	2,5
2010	Maule	8,8	3,2
1960	Valdivia	9,5	1,6
1960	Valdivia	9,5	2
1960	Valdivia	9,5	1,5
1960	Valdivia	9,5	1,1
1960	Valdivia	9,5	1,5

ANNEX 2

Map of part of the study area, showing location, orientation and type of some of the photographs taken for this work.

